Localized Vibrational Modes in High-Entropy Oxides

Connor M. Wilson, B.Sc.

Experimental Condensed Matter Physics and Materials Science

Submitted in partial fulfillment of the requirements for the degree of

Master of Science

Faculty of Mathematics and Science, Brock University
St. Catharines, Ontario

Abstract

The existence of localized vibrational modes in the high-entropy oxide $Mg_{0.2}Co_{0.2}Ni_{0.2}Cu_{0.2}Zn_{0.2}O$ is investigated using classical lattice dynamics. New empirical interatomic potentials for the cation-oxygen interactions in $Mg_{0.2}Co_{0.2}Ni_{0.2}Cu_{0.2}Zn_{0.2}O$ are developed and are shown to yield superior agreement with the experimental crystal structures, dielectric constants, and phonon frequencies of the parent binary oxides. Various probes for localization are calculated and suggest $Mg_{0.2}Co_{0.2}Ni_{0.2}Cu_{0.2}Zn_{0.2}O$ supports localized modes beyond a high-frequency mobility edge in the vibrational density-of-states.

Acknowledgements

I would like to express my deepest gratitude to my supervisor, Dr. D. Crandles, for introducing me to the field of high-entropy oxides, to Dr. G. Ramachandran, for many insightful conversations about Anderson localization, and to Dr. E. Sternin, for his longtime mentorship and invaluable help with data fitting and analysis. He is credited with the interpretation of the multiexponential fit in Sect. 4.3.3. Thank you to my mother and brother, K. and C. Wilson, my wonderful girlfriend S. Hesse, and to my late grandmother R. Pattison, for their endless love and support. I am also grateful to the National Sciences and Engineering Research Council of Canada (NSERC), the Ontario Provincial Government (QEII-GSST), and the many generous benefactors at Brock University for helping to finance this work.

Thank you to Dr. Eric de Giuli from Toronto Metropolitan University, for serving as external examiner and for the suggestion to plot the 2D eigenvector fields in Sect. 4.2.3. Thank you also to Dr. Jiri Hlinka from the Czech Academy of Sciences for the suggestion to investigate the possibility of short-range cation ordering in Sect. 4.3.4.

Contents

List of Tables

List of Figures

Chapter 1

Introduction

1.1 High-Entropy Oxides

1.1.1 Overview

The field of high-entropy oxides (HEOs)[1] began with the synthesis of $Mg_{0.2}Co_{0.2}Ni_{0.2}Cu_{0.2}Zn_{0.2}O$ in 2015 by C. M. Rost et al. [1]. HEO was prepared by ball-milling an equiatomic mixture of the binary oxides MgO, CoO, NiO, CuO, and ZnO into a powder, using a hydraulic press to form the powder into pellets, and sintering the pellets in a tube furnace. If the pellets were sintered at a temperature $T > T_c$ (where the critical temperature T_c is between 850–900 °C) and air-quenched to room temperature, XRD and SEM results revealed HEO crystallized in a single-phase rocksalt structure with an ordered oxygen sublattice and a cation sublattice which was occupied with equal probability by Mg, Co, Ni, Cu, and Zn. This was despite a) nonuniform crystal structures[2], electronegativities, and cation coordination numbers, and; b) limited mutual solid solubility. A possible[3] crystal structure of HEO is shown schematically in Fig. 1.1. Rost et al. further demonstrated that HEO undergoes a

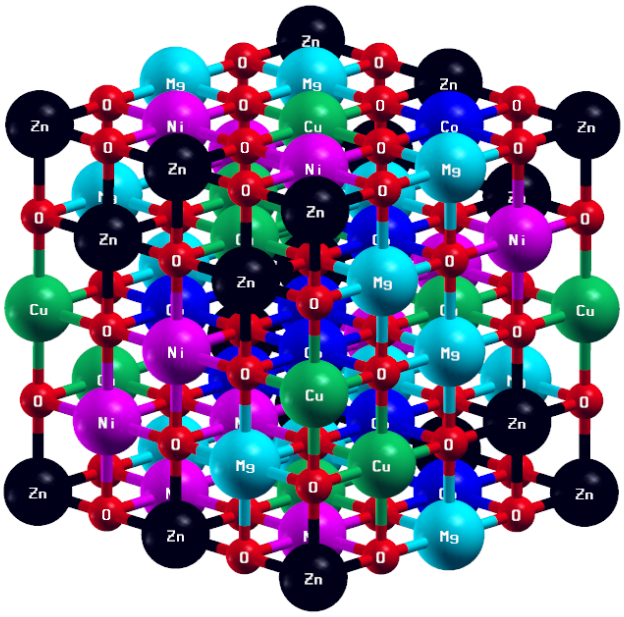

Figure 1.1: Possible instance of a 64-atom $Mg_{0.2}Co_{0.2}Ni_{0.2}Cu_{0.2}Zn_{0.2}O$ supercell.

[1]Unless otherwise indicated, throughout this thesis 'HEO' shall refer to $Mg_{0.2}Co_{0.2}Ni_{0.2}Cu_{0.2}Zn_{0.2}O$.

[2]MgO, CoO, and NiO crystallize in the rocksalt structure at STP, whereas ZnO and CuO crystallize in the wurtzite and tenorite structures, respectively.

[3]'Possible', since the configuration space of the cation sublattice is immense.

reversible single-phase to multi-phase structural transformation as the sintering temperature is adjusted. When HEO prepared at $T > T_c$ is re-sintered between 800–850 °C, a needle-shaped Cu-rich tenorite phase emerges. At still lowering sintering temperatures between 700–750 °C, an elongated, particle-shaped Co-rich spinel phase also precipitates out of HEO [2]. However, if HEO is again re-sintered back to $T > T_c$, the tenorite and spinel phases dissolve and the single-phase rocksalt structure is recovered. This is referred to as 'phase cycling' below, although this is not standard nomenclature. Since their inception in 2015, high-entropy oxides crystallizing in the spinel [3], perovskite [4], and α-PbO_2 [5] structures have been synthesized, among many others. B. Musico et al. have previously reviewed some of the various high-entropy oxides and corresponding experimental results which have been studied as of 2020 [6]. For reference, Table 1.1 reviews the masses of the

Ion	Mass ($\mathrm{g\,mol^{-1}}$)
O	16.00
Mg	24.31
Co	58.93
Ni	58.69
Cu	63.55
Zn	65.38

Table 1.1: Masses of the constituent ions in HEO.

constituent ions in HEO. Oxygen is the lightest ion at 16 $\mathrm{g\,mol^{-1}}$, followed by Mg at 24 $\mathrm{g\,mol^{-1}}$. Cobalt, nickel, copper, and zinc are nearest-neighbours on the periodic table and have an average mass of roughly 60 $\mathrm{g\,mol^{-1}}$.

A precise, all-encompassing definition of a high-entropy material has not yet been established. However, it is widely accepted that high-entropy materials are crystalline, single-phase, and mass-disordered down to the atomic scale [7].

Differentiating high-entropy materials from conventional solid solutions is not easy. Some experimental tests which have been proposed are: a) a configurational entropy in excess of $1.6R$, where R is the ideal gas constant; b) an endothermic reaction enthalpy, and; c) a crystal structure which is different from the parent oxides. None of these tests are perfect in isolation. For example, (Ti,Zr)O_2 satisfies criteria b) and c), but its configurational entropy is much less than $1.6R$ [7]. Phase cycling was initially thought to be the definitive characteristic of a configurational entropy-stabilized material; however, a recent paper by Fracchia et al. on $Mg_{0.2}Co_{0.2}Ni_{0.2}Cu_{0.2}Zn_{0.2}O$ showed that phase-cycling occurs even in the ternary oxide $Ni_{0.8}Cu_{0.2}O$, where the configurational entropy is considerably lower [8]. Hence, while configurational entropy is significant, a prominent role is still played by conventional solid solubility limits. Aamlid et al. have proposed a new 'gold standard' for entropic stabilization might be attempting to identify a systematic variation of the single-phase dissolution with configurational entropy as the stoichiometry of the cations is adjusted [7].

1.1.2 Previous Work

Kotsonis et al. have recently reviewed the functional properties of $Mg_{0.2}Co_{0.2}Ni_{0.2}Cu_{0.2}Zn_{0.2}O$ which have been studied as of 2023 [9]. Some of the salient results from their paper are listed below. Investigations into the infrared and Raman spectra of HEO are also summarized.

Thermal Conductivity

Lim et al. have measured a low thermal conductivity[4] of 3 $\mathrm{W\,mK^{-1}}$ in HEO [10]. This is above the analytic limit for an amorphous system despite the strong phonon scattering resulting from mass and force constant disorder. Lim et al. have also shown that the thermal conductivity of HEO further decreases by a factor of roughly one-half if any of Sc, Sn, Cr, or Ge are added to the cation sublattice. Braun et al. have shown that the low thermal conductivity of HEO is not concomitant with an increased elastic modulus [11]. This is in contrast to conventional materials. HEO therefore allows for an interesting and unusual combination of material properties.

Energy Storage

Bérardan et al. reported a high room-temperature Li-ion conductivity[5] of 10^3 S/cm in HEO [13]. Sarkar et al. later showed that the specific capacity of HEO cells remains stable after 50 charge and discharge cycles. The removal of one cation species drastically alters the electrochemical behaviour [14]. HEO shows potential for applications to solid-state batteries by tuning the stoichiometry of the cations to alter the Li storage properties.

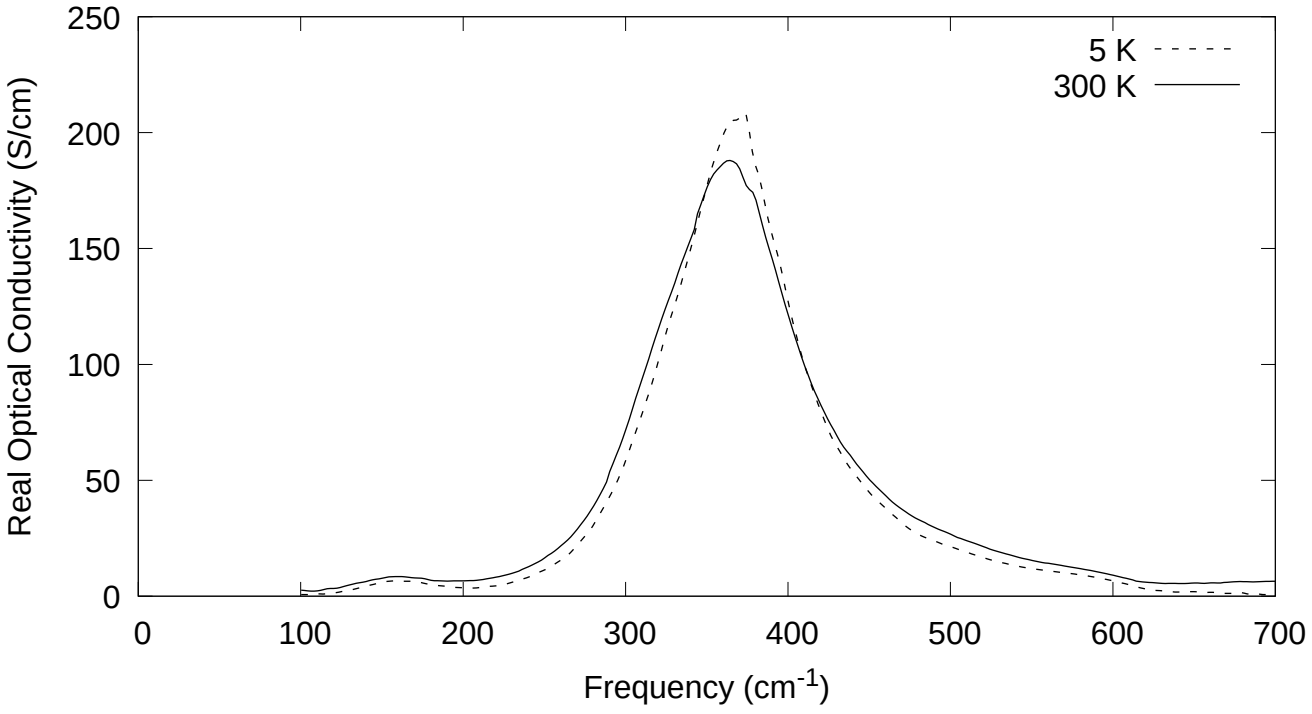

Figure 1.2: Real part of the optical conductivity of HEO. Adapted from [15].

Infrared Spectroscopy

Afsharvosoughi and Crandles have measured the infrared reflectance of HEO and extracted the real part of the optical conductivity from Kramers-Kronig analysis [15]. See Fig. 1.2. Their data

[4]For reference, the thermal conductivity of pure MgO is between 45–60 $\mathrm{W\,mK^{-1}}$ [10].
[5]The 300 K Li-ion conductivity of common electrolytes and ranges from 10^{-8}–10^{-3} S/cm [12].

consists of a strong mode near 360 cm^{-1} and a weak mode near 150 cm^{-1}. The weak mode is of unclear origin, although the insignificant temperature dependence in Fig. 1.2 likely rules out anharmonic effects. The strong mode was associated with the reststrahlen band characteristic of rocksalt crystals. NiO and CoO present subsidiary structures in their reststrahlen bands below their Néel temperatures T_N due to spin-phonon coupling. However, no such features emerge in HEO even as it is cooled below $T_N = 112$ K. This was attributed to the high scattering rate of the strong mode.

Raman Spectroscopy

T. Afsharvosoughi has also measured the temperature-dependent Raman spectrum of HEO [16]. Their data consists of five peaks, the first four of which have been assigned to, in order of increasing frequency, a TO, LO, LO + TO, and 2LO mode, respectively[6]. The nature of the fifth peak is not clear. On one hand, its central frequency is close to $3\omega_{LO}$, where ω_{LO} is the LO central frequency, and may therefore be a 3LO mode. On the other hand, the strength of the mode increases significantly as HEO is cooled below T_N. In analogy with the Raman spectrum of pure NiO. the fifth peak may be a two-magnon mode. Further theoretical investigation into magnetic ordering in HEO may be needed to resolve the nature of this mode.

1.2 Plan for this Thesis

The scaling theory of localization (see Sect. 2.2 for further details) suggests that the eigenstates of a three-dimensional system are either localized or extended, depending upon the amount of disorder present in the system. Given that the cation sublattice of HEO is strongly disordered, it is natural to ask whether or not the vibrational modes of HEO are localized. It should be noted that HEO is a cleaner platform to study vibrational mode localization than the sister field of high-entropy alloys, which are electrically conducting and hence require a treatment of electron-phonon coupling. In addition, localized vibrational modes have been shown to reduce the thermal conductivity of GaAs/AlAs superlattices by up to 50% [17], and are therefore of practical importance for the application of HEO to thermal coatings.

In this thesis, large, toy model HEO supercells are constructed from a 'superposition' of the parent binary oxides. For example, the Mg–O interaction in HEO is assumed to be the same as it is in pure MgO, and so forth. See Sect. 3.1 for more details regarding the interaatomic potentials. Classical lattice dynamics is used to extract the eigenfrequencies and eigenvectors of HEO, from which various probes for localization are calculated. Previous studies; *i.e.* the works of Anand et al. [18] and Chen et al. [19], have also constructed toy models of HEO in this way to study its thermodynamics and the mechanical effects of Li-dopant, respectively. To the best of the author's knowledge, however, this thesis represents the first demonstration that localized vibrational modes do indeed exist in HEO.

Chapter 2 discusses the relevant theoretical background in classical lattice dynamics and Anderson localization. Chapter 3 develops empirical interatomic potentials for HEO by fitting to the crystal structures, dielectric constants, and phonon frequencies of the parent binary oxides. Chapter 4 confirms the potentials reproduce the experimental crystal structure and optical conductivity of HEO and presents several diagnostics for mode localization.

[6]Here first letter indicates whether the mode involves a longitudinal (L) or transverse (T) phonon; uppercase "O" indicates an optical phonon. Sect. 2.2.2 explains these classifications in greater detail. The LO + TO and 2LO modes are combination modes involving an LO and a TO phonon and two LO phonons, respectively.

Chapter 2

Theory

2.1 Classical Theory of Lattice Dynamics

In this section the theory of lattice dynamics within the framework of classical mechanics is reviewed. The notation used is adopted from Srivastava [20], with the one exception that ε is used instead of e to denote a phonon eigenvector. Vector notations such as overarrows/boldface are omitted for brevity; it is clear from the context which quantities are scalars and which are vectors.

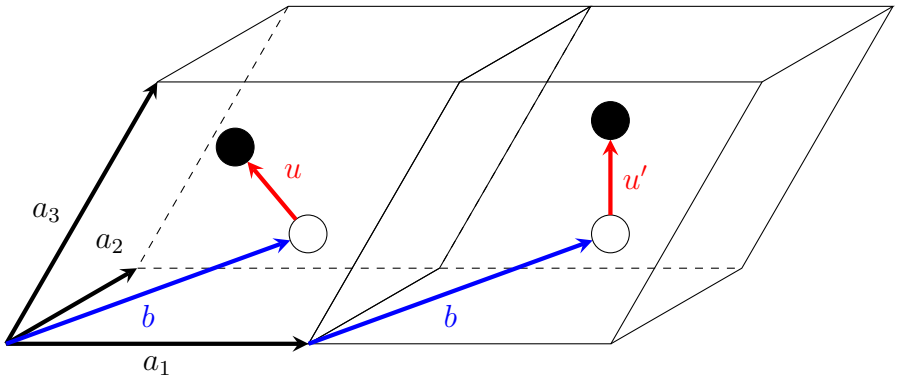

Figure 2.1: Two unit cells in a crystal.

2.1.1 Equations of Motion

Consider a d-dimensional crystal composed of $N \equiv \prod_\alpha N_\alpha$ unit cells located at

$$\text{Unit cell positions} = \{\ell \equiv (\ell_1, \ldots, \ell_d) : \ell_\alpha \in [0, N_\alpha - 1] \ \forall \alpha \in [1, d]\}$$

where N_α is the number of unit cells in the αth primitive direction. Each unit cell further contains p basis atoms situated at

$$\text{Basis atom positions} = \{b \equiv (b_1, \ldots, b_d) : b_\alpha \in [0, N_\alpha - 1] \ \forall \alpha \in [1, d]\}$$

At zero temperature, the Np atoms are 'frozen' at $\{\ell + b\}$, ignoring zero-point motion. At finite temperature, the atoms fluctuate about $\{\ell + b\}$ by the time-dependent displacement vectors $\{u\}$:

$$x_\alpha(\ell b; t) = \ell_\alpha + b_\alpha + u_\alpha(\ell b; t) \tag{2.1}$$

where the time dependence of x, u will henceforth be suppressed. The Lagrangian for the crystal is:

$$\mathcal{L} = \frac{1}{2} \sum_{\ell b} m_b \, \dot{u}_\alpha(\ell b)^2 - U\left(\{x\}\right) \tag{2.2}$$

where m_b is the mass of the bth basis atom and U is the potential energy of the crystal, whose dependence on $\{x\}$ is not known *a priori*. Summation over repeated vector projections is implicit throughout this section. Substituting Eq. 2.2 into the Euler-Lagrange equations leads to dpN coupled, nonlinear equations of motion. This is a completely intractable problem. The following assumption about the $\{u\}$ must be made to make progress:

> *Assumption of small atomic displacements: The thermal excursions $\{u\}$ are much smaller than the zero-temperature interatomic spacings $\{\ell + b\}$.*

If this assumption holds, U can be expanded in a Taylor series of the $\{u\}$:

$$U(\{x\}) = U(\{\ell + b\}) + \sum_{\ell b} \Phi_\alpha(\ell b)\, u_\alpha(\ell b) + \frac{1}{2} \sum_{\ell b} \sum_{\ell' b'} \Phi_{\alpha\beta}(\ell b; \ell' b')\, u_\alpha(\ell b)\, u_\beta(\ell' b') + \dots \tag{2.3}$$

where the 'force constants' are defined by

$$\Phi_\alpha(\ell b) = \left. \frac{\partial U}{\partial u_\alpha(\ell b)} \right|_0 \qquad \Phi_{\alpha\beta}(\ell b; \ell' b') = \left. \frac{\partial^2 U}{\partial u_\alpha(\ell b)\, \partial u_\beta(\ell' b')} \right|_0 \tag{2.4}$$

with obvious generalizations to higher-order terms. The notation $\big|_0$ is shorthand for 'evaluated at the zero-temperature configuration'. By choosing the constant $U(\{\ell + b\})$ as the zero of potential energy in Eq. 2.3, it can be discarded without loss of generality.

> *Assumption of mechanical equilibrium: The zero-temperature configuration $\{\ell + b\}$ is also an equilibrium configuration.*

The force exerted on atom (ℓb) by the rest of the crystal is

$$F_\alpha(\ell b) = -\frac{\partial U}{\partial u_\alpha(\ell b)} = -\Phi_\alpha(\ell b) - \sum_{\ell' b'} \Phi_{\alpha\beta}(\ell b; \ell' b')\, u_\beta(\ell' b') + \dots$$

Thus if the foregoing assumption holds, the $\{F\}$ must vanish in the limit $\{u \to 0\}$. This can only be true if $\{\Phi_\alpha(\ell b) = 0\}$. Consequently, Eq. 2.3 reduces to

$$U(\{x\}) = \frac{1}{2} \sum_{\ell b} \sum_{\ell' b'} \Phi_{\alpha\beta}(\ell b; \ell' b')\, u_\alpha(\ell b)\, u_\beta(\ell' b') + \dots \tag{2.5}$$

The $\mathcal{O}(u^2)$ term in Eq. 2.5 is called the 'harmonic' term, while the terms of $\mathcal{O}(u^3)$ and above are collectively referred to as 'anharmonic' terms. From the infinity of anharmonic terms in Eq. 2.5 it follows that the Euler-Lagrange equations still cannot be solved in closed form. One more assumption must be made:

> *Harmonic approximation: For sufficiently small[1] temperatures the anharmonic contributions to Eq. 2.5 are negligible compared to the harmonic term.*

[1] The notion of 'sufficiently small' temperatures depends strongly on both the material and the physical quantity under study. For instance, anharmonic effects manifest in the reflectance spectrum of MgO already at 5 K [21], but excellent agreement with inelastic neutron scattering data taken at 300 K can be obtained within the harmonic approximation [22].

Thus if the harmonic approximation holds, Eq. 2.5 assumes the much simplified form

$$U(\{x\}) = \frac{1}{2}\sum_{\ell b}\sum_{\ell' b'} \Phi_{\alpha\beta}(\ell b;\ell' b')\, u_\alpha(\ell b)\, u_\beta(\ell' b') \tag{2.6}$$

Substituting Eq. 2.6 into the Euler-Lagrange equations produces

$$m_b\, \ddot{u}_\alpha(\ell b) = -\sum_{\ell' b'} \Phi_{\alpha\beta}(\ell b;\ell' b')\, u_\beta(\ell' b') \tag{2.7}$$

which is Newton's second law for a crystal. There are dpN coupled differential equations of the form Eq. 2.7, but the harmonic approximation has guaranteed they are all linear, and therefore amenable to solution by Fourier transform. This will be discussed in Sect. 2.1.3. All the material dependence is contained within the force constants $\{\Phi_{\alpha\beta}(\ell b;\ell' b')\}$ and the masses $\{m_b\}$.

2.1.2 Symmetries of the Force Constant Matrix

1. *Clairaut's symmetry: It follows from the definition of the force constants as mixed partial derivatives that*[2]
$$\Phi_{\alpha\beta}(\ell b;\ell' b') = \Phi_{\beta\alpha}(\ell' b';\ell b) \tag{2.8}$$

2. *Translational invariance: The potential is invariant under translations of the lattice into itself:*
$$\Phi_{\alpha\beta}(\ell b;\ell' b') = \Phi_{\alpha\beta}(\ell+\ell'', b;\ell'+\ell'', b') \tag{2.9}$$
By choosing $\ell'' = -\ell$ or $\ell'' = -\ell'$, it follows that the force constants depend on the coordinates of the unit cells only through their difference:
$$\Phi_{\alpha\beta}(\ell b;\ell' b') = \Phi_{\alpha\beta}(0b;\ell'-\ell, b') = \Phi_{\alpha\beta}(\ell-\ell', b;0b')$$

3. *Rigid-body invariance: The force exerted on each atom is invariant under rigid-body translations of the crystal through a constant vector c:*
$$F_\alpha(\ell b) = -\frac{\partial U}{\partial u_\alpha(\ell b)} = -c_\beta \sum_{\ell' b'} \Phi_{\alpha\beta}(\ell b;\ell' b') \overset{!}{=} 0$$
Since the components of c are linearly independent, this implies the 'acoustic sum rule'
$$\sum_{\ell' b'} \Phi_{\alpha\beta}(\ell b;\ell' b') = 0 \tag{2.10}$$

Additional constraints follow from the invariance of the potential and forces under rotations and point group symmetries [23], but they will not be needed here.

[2] There is no standardized name for this symmetry. It is called Clairaut's symmetry here after Clairaut's theorem in mathematics, which guarantees the equality of mixed partial derivatives under weak assumptions of continuity.

2.1.3 Dynamical Matrix

The solution of Eq. 2.7 in the steady state is a plane-wave of the form

$$u_\alpha(\ell b) = \frac{1}{\sqrt{m_b}} \sum_q \varepsilon_\alpha(b;q)\, \exp[i\,(q\cdot\ell - \omega_q t)] \tag{2.11}$$

where q is a wavevector, ω_q is the frequency of the qth vibrational mode, and the dpN coefficients $\{\varepsilon_\alpha(b;q)\}$ are to be determined. By imposing periodic boundary conditions

$$u_\alpha(\ell + N_\alpha a_\alpha, b) \stackrel{!}{=} u_\alpha(\ell b) \implies q\cdot a_\alpha = \frac{2\pi n_\alpha}{N_\alpha},\ n_\alpha \in [0, N_\alpha - 1]\ \forall\alpha$$

it follows that there are $N = \prod_\alpha N_\alpha$ allowed wavevectors – one for each unit cell in the crystal. Substituting Eq. 2.11 into Eq. 2.7:

$$\sum_q \exp(-i\omega_q t)\left[\omega_q^2\varepsilon_\alpha(b;q)\,\exp(iq\cdot\ell) - \frac{1}{\sqrt{m_b}}\sum_{\ell' b'}\Phi_{\alpha\beta}(\ell b;\ell' b')\frac{1}{\sqrt{m_{b'}}}\varepsilon_\beta(b';q)\,\exp(iq\cdot\ell')\right] = 0$$

$$\sum_q \exp[i\,(q\cdot\ell - \omega_q t)]\left[\omega_q^2\varepsilon_\alpha(b;q) - \frac{1}{\sqrt{m_b}}\sum_{\ell' b'}\Phi_{\alpha\beta}(\ell b;\ell' b')\frac{1}{\sqrt{m_{b'}}}\varepsilon_\beta(b';q)\,\exp[iq\cdot(\ell'-\ell)]\right] = 0$$

$$\sum_q \exp[i\,(q\cdot\ell - \omega_q t)]\left[\omega_q^2\varepsilon_\alpha(b;q) - \frac{1}{\sqrt{m_b}}\sum_{\ell' b'}\Phi_{\alpha\beta}(0b;\ell'-\ell,b')\frac{1}{\sqrt{m_{b'}}}\varepsilon_\beta(b';q)\,\exp[iq\cdot(\ell'-\ell)]\right] = 0$$

$$\sum_q \exp[i\,(q\cdot\ell - \omega_q t)]\left[\omega_q^2\varepsilon_\alpha(b;q) - \frac{1}{\sqrt{m_b}}\sum_{\ell' b'}\Phi_{\alpha\beta}(0b;\ell' b')\frac{1}{\sqrt{m_{b'}}}\varepsilon_\beta(b';q)\,\exp(iq\cdot\ell')\right] = 0$$

$$\sum_q \exp[i\,(q\cdot\ell - \omega_q t)]\left[\omega_q^2\varepsilon_\alpha(b;q) - \sum_{b'}\varepsilon_\beta(b';q)\,\underbrace{\frac{1}{\sqrt{m_b m_{b'}}}\sum_{\ell'}\Phi_{\alpha\beta}(0b;\ell' b')\,\exp(iq\cdot\ell')}_{D_{\alpha\beta}(bb';q)}\right] = 0$$

$$\sum_q \exp[i\,(q\cdot\ell - \omega_q t)]\,\underbrace{\left[\omega_q^2\varepsilon_\alpha(b;q) - \sum_{b'} D_{\alpha\beta}(bb';q)\,\varepsilon_\beta(b';q)\right]}_{E_\alpha(b;q)} = 0$$

$$\sum_q \exp[i\,(q\cdot\ell - \omega_q t)]\,E_\alpha(b;q) = 0$$

In the third line the symmetry Eq. 2.9 has been used. The fourth line follows from changing the summation index from $\ell' - \ell \to \ell'$.

The sum over q in the final line vanishes if and only if $E_\alpha(b;q) = 0\ \forall q$. Clearly $E_\alpha(b;q) = 0$ is a necessary condition. To prove that it is also sufficient, multiply through by $\exp(-iq'\cdot\ell)$ and sum over ℓ:

$$\sum_q \exp(-i\omega_q t)\,E_\alpha(b;q)\underbrace{\sum_\ell \exp[i(q-q')\cdot\ell]}_{N\delta_{q-q',0}} = 0 \implies \exp(-i\omega_q t)E_\alpha(b;q) = 0\ \forall q$$

The factor $\exp(-i\omega_q t)$ is always nonzero and can be safely divided out. The plane wave ansatz Eq. 2.11, which is consistent with the translational symmetry Eq. 2.9, has therefore reduced the dpN coupled equations of motion Eq. 2.7 to N independent matrix equations $E_\alpha(b;q) = 0$, or

$$\omega_q^2 \varepsilon_\alpha(b;q) = \sum_{b'} D_{\alpha\beta}(bb';q)\, \varepsilon_\beta(b';q) \tag{2.12}$$

where $\{D_{\alpha\beta}(bb';q)\}$ are elements of the $dp \times dp$ dynamical matrix defined by

$$D_{\alpha\beta}(bb';q) = \frac{1}{\sqrt{m_b m_{b'}}} \sum_{\ell'} \Phi_{\alpha\beta}(0b;\ell' b')\, \exp(iq\cdot\ell') \tag{2.13}$$

whose eigenvalues are the $\{\omega_q^2\}$ and whose eigenvectors, which were initially introduced as Fourier expansion coefficients in Eq. 2.11, are the $\{\varepsilon_\alpha(b;q)\}$.

The following argument shows the dynamical matrix is also Hermitian:

$$\begin{aligned}
D_{\beta\alpha}(b'b;q)^* &= \frac{1}{\sqrt{m_{b'} m_b}} \sum_{\ell'} \Phi_{\beta\alpha}(0b';\ell' b)\, \exp(-iq\cdot\ell') \\
&= \frac{1}{\sqrt{m_b m_{b'}}} \sum_{\ell'} \Phi_{\beta\alpha}(0b';-\ell' b)\, \exp(iq\cdot\ell') \\
&= \frac{1}{\sqrt{m_b m_{b'}}} \sum_{\ell'} \Phi_{\alpha\beta}(-\ell' b;0b')\, \exp(iq\cdot\ell') \\
&= \frac{1}{\sqrt{m_b m_{b'}}} \sum_{\ell'} \Phi_{\alpha\beta}(0b;\ell' b')\, \exp(iq\cdot\ell') \\
&= D_{\alpha\beta}(bb';q)
\end{aligned}$$

The second line follows from changing the summation index to $\ell' \to -\ell'$, the third line follows from Clairaut's symmetry Eq. 2.8, and the fourth line follows from Eq. 2.9. By a standard theorem of linear algebra, the Hermiticity of the dynamical matrix guarantees it has exactly dp eigenfrequencies and dp eigenvectors [24]. To keep track of which eigenvector corresponds to which eigenfrequency, a label s will be appended to the $\{\omega_q\}$ and the $\{\varepsilon_\alpha(b;q)\}$ as follows

$$\omega_q \to \omega_{qs}; \quad \varepsilon_\alpha(b;q) \to \varepsilon_\alpha(b;qs)$$

Hermiticity further implies that the eigenvalues of the dynamical matrix $\{\omega_{qs}^2\}$ are all real and that the eigenvectors are orthonormal

$$\sum_b \varepsilon_\alpha^*(b;qs)\, \varepsilon_\alpha(b;qs') = \delta_{ss'} \tag{2.14}$$

and complete [24]:

$$\sum_s \varepsilon_\alpha^*(b;qs)\, \varepsilon_\beta(b';qs) = \delta_{\alpha\beta}\, \delta_{bb'} \tag{2.15}$$

The completeness relation in particular implies the general solution to Eq. 2.7 can be expanded in

a series of the eigenvectors:

$$u_\alpha(\ell b;t) = \frac{1}{\sqrt{N m_b}} \sum_{qs} A_{qs}\, \varepsilon_\alpha(b;qs)\, \exp\{i\,(q\cdot\ell - \omega_{qs}t)\} \tag{2.16}$$

where the expansion coefficients $\{A_{qs}\}$ are to be determined from the initial conditions. Eq. 2.16 is the starting point for the theory of vibrational wavepacket dynamics developed in Sect. 2.3.2. Alternatively, it is possible to show that the Hamiltonian is diagonal when written in terms of certain real linear combinations of the $\{A_{qs}\}$. These combinations are called 'normal coordinates', and are formulated explicitly in Eq. 2.30. When the Hamiltonian is then quantized, one finds

$$\hat{\mathcal{H}} = \sum_{qs} \hbar\omega_{qs} \left(\hat{a}^\dagger_{qs}\, \hat{a}_{qs} + \frac{1}{2} \right)$$

which is formally identical to the Hamiltonian of the 1D quantum harmonic oscillator. The operator $\hat{a}^\dagger_{qs}$ creates one quasiparticle – a phonon – with crystal momentum $\hbar q$ in the eigenmode s.

There are additional constraints on the eigenvectors and eigenfrequencies which will be needed in Sect. 2.3. From above, the squared eigenfrequencies $\{\omega^2_{qs}\}$ are purely real. It follows that the eigenfrequencies $\{\omega_{qs}\}$ themselves are either purely real or purely imaginary. The latter possibility can be excluded on physical grounds, since Eq. 2.11 implies imaginary eigenfrequencies cause the atomic displacements to erupt exponentially in time, in contradiction with the assumption that the potential was expanded about an equilibrium configuration. Hence $\{\omega_{qs} \geq 0\}$. In addition, it is possible to prove by demanding that Eq. 2.11 obeys time reversal symmetry that [20]

$$\omega_{qs} = \omega_{-qs} \tag{2.17}$$

from which it also follows

$$\varepsilon^*_\alpha(b;qs) = \varepsilon_\alpha(b;-qs) \tag{2.18}$$

It is also important to note[3] that the eigenvectors are purely real at the Brillouin zone centre. This follows from setting $q = 0$ in the Hermiticity argument. It is easy to see in this case that the dynamical matrix is real and symmetric, and can therefore be diagonalized by a real orthogonal matrix of its eigenvectors [24].

2.1.4 Coulomb Interaction

In an ionic crystal the Coulomb interaction between electrically-charged ions can account for up to 90% of the potential energy [25]. It can be shown that the Coulomb interaction introduces a modification to the dynamical matrix of the form [26]

$$D \to D + ZCZ \tag{2.19}$$

where Z is a diagonal matrix of the ionic charges and ZCZ is defined by

$$z_b\, z_{b'}\, C_{\alpha\beta}(bb';q) = \sum_{\ell'} \Phi^{(C)}_{\alpha\beta}(\ell b, \ell' b') \exp(-iq\cdot\ell') \tag{2.20}$$

[3] All phonon calculations in Chapter 4 were performed at $q = 0$.

where z_b is the charge on the bth atom. The $\{\Phi^{(C)}\}$ are the Coulomb force constants; *i.e.* derivatives of the Coulomb interaction with respect to interatomic distances. Since the Fourier transform of the r^{-1} potential does not exist, the series Eq. 2.20 is conditionally convergent; *i.e.* its value depends on the direction $q \to 0$ in reciprocal space[4]. In this thesis, Eq. 2.20 was summed by applying Ewald's method[5], as a result of which it was decomposed into two terms: one which converges rapidly in real space, and another which converges rapidly in reciprocal space [25].

2.1.5 The Shell Model

The results of Sect. 2.1.4 are only valid so long as the ions are treated as point changes. This is known as the 'rigid-ion model'. Because the polarisabilty of the ions is ignored, the rigid ion model incorrectly predicts $\epsilon_\infty = 1$ [26]. A glance at the data in Appendix A shows that the binary oxides in HEO have a high-frequency dielectric constant $\epsilon_\infty \sim 4$.

One solution to this problem is the 'shell model' introduced by Dick and Overhauser [27], in which atoms are decomposed into massive point charges bonded by isotropic, harmonic springs to massless, charged shells; *i.e.* a core-shell pair interact via

$$\Phi(r) = \frac{1}{2}\, kr^2 \tag{2.21}$$

where k is the stiffness constant and r is the core-shell distance. The atomic polarisability is

$$\alpha = \frac{(Ye)^2}{k} \tag{2.22}$$

where e is the electron change and Y (in units of e) is the shell charge. The shell model qualitatively captures the quantum-mechanical reality of a charged nucleus surrounded by an electron cloud. If the shell model is applied to an ionic crystal, the dynamical matrix becomes [26]

$$D \to D + ZCZ - (D_{cs} + ZCY)\,(D_{ss} + YCY)^{-1}\,(D_{cs} + ZCY)^T \tag{2.23}$$

where Y is a diagonal matrix of the shell charges, and D_{cs}, D_{ss}, describe the core-shell and shell-shell interactions, respectively. If the shells are omitted; *i.e.* $D_{cs} = D_{ss} = Y = 0$, then Eq. 2.23 correctly reduces to the dynamical matrix Eq. 2.19 of an ionic crystal in the rigid-ion description.

2.2 Anderson Localization

2.2.1 Overview

In 1958, P. Anderson proposed that scattering from a static, random potential could cause electronic eigenstates to localize and induce a phase transition from a conducting to an insulating material [28]. An example of how this might occur in 1D is shown in Fig. 2.2. Although the eigenstates $|1\rangle, |2\rangle$ are energetically degenerate, they are too far removed spatially for electrons to hop between them. This phenomenon has come to be known as 'Anderson localization' and applies to waves in general (*i.e.* and not just to electronic Bloch states). Subsequent experimental studies have even observed the Anderson localization of light and sound waves [29]. The scaling theory of localization devel-

[4]This property is responsible for the phenomenon of LO-TO splitting in ionic crystals.

[5]This is the default setting in `GULP`, the program that was used to perform the lattice dynamical calculations. See Sect. 3.2 for more details about `GULP`.

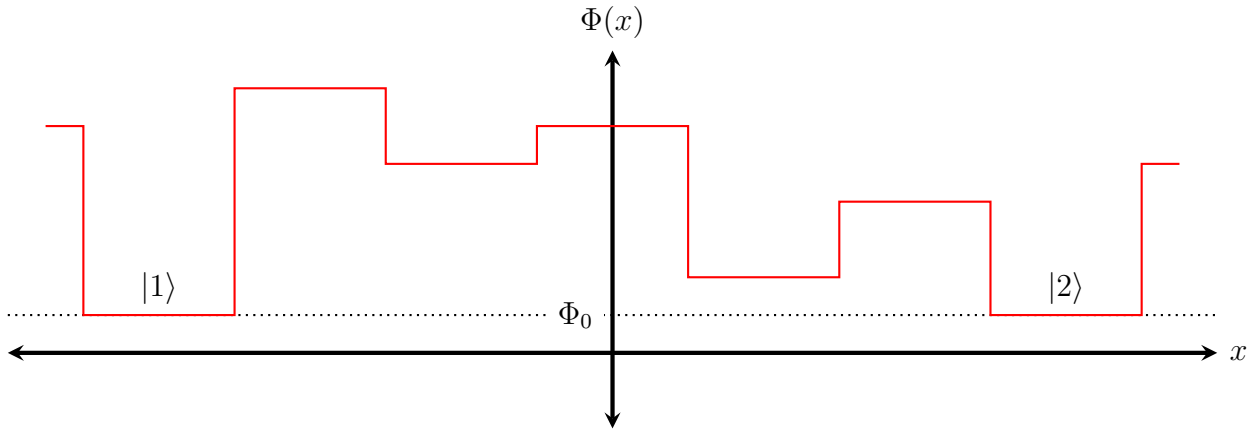

Figure 2.2: Random potential landscape in one dimension. The eigenstates with energy Φ_0 are too far apart for electrons to hop between them. Adapted from [30].

oped in 1979 by the 'gang of four' (Abrahams, Anderson, Licciardello, and Ramakrishnan) showed that any amount of disorder whatsoever is sufficient to localize all eigenstates in one- and two-dimensions. In three-dimensions eigenstates may be localized or extended, depending upon the amount of disorder in the system [31].

2.2.2 Vibrational Modes in Disordered Media

It has been shown in Sect. 2.1.3 that for each the N allowed values of the wavevector q, the vibrations in crystalline solids are characterised by dp frequencies $\{\omega_{qs}^2\}$ and eigenvectors $\{\varepsilon_\alpha(b;qs)\}$ obtained by diagonalizing the dynamical matrix. The 'dispersion relation' is the dp-fold multivalued function obtained by plotting ω_{qs} against q. The vibrational density-of-states (VDOS)

$$\mathcal{D}(\omega) = \sum_{qs} \delta(\omega - \omega_{qs}) \tag{2.24}$$

counts the number of modes with frequencies between ω and $\omega + \mathrm{d}\omega$. In practise the delta function in Eq. 2.24 is sometimes approximated by a Lorentzian function [25] with a broadening factor b comparable to the resolution of INS experiments; *i.e.*

$$\delta(\omega - \omega_{qs}) \approx \frac{b/\pi}{1 + \left[b\left(\omega - \omega_{qs}\right)^2\right]} \tag{2.25}$$

It is very important to emphasize that all the theory discussed so far is valid only for crystalline media. In an amorphous solid the translational symmetry Eq. 2.9 is broken and the wavevector q is ill-defined. Stated another way, the equations of motion Eq. 2.7 can no longer be decoupled by a plane wave expansion of the form Eq. 2.11. It follows immediately from the non-existence of q that the dispersion relation likewise does not exist in an amorphous solid. The VDOS, on the other hand, can be generalized and assumes the form

$$\mathcal{D}(\omega) = \sum_{i} \delta(\omega - \omega_i) \tag{2.26}$$

where the $\{\omega_i\}$ are the frequencies obtained from a brute-force diagonalization of the 10^{23} equations of motion Eq. 2.7. It is worth noting that Eq. 2.26 can be thought of as the limit of Eq. 2.24 in the absence of translational symmetry.

While Eq. 2.26 is conceptually true, it is not useful in practise. It is simply not possible to set up and solve 10^{23} coupled differential equations for the frequencies $\{\omega_i\}$. As a workaround, the method of 'supercell lattice dynamics' can be applied to obtain an approximation to the VDOS of an amorphous solid using the machinery of Sect. 2.1. This will be discussed in Sect. 2.2.3.

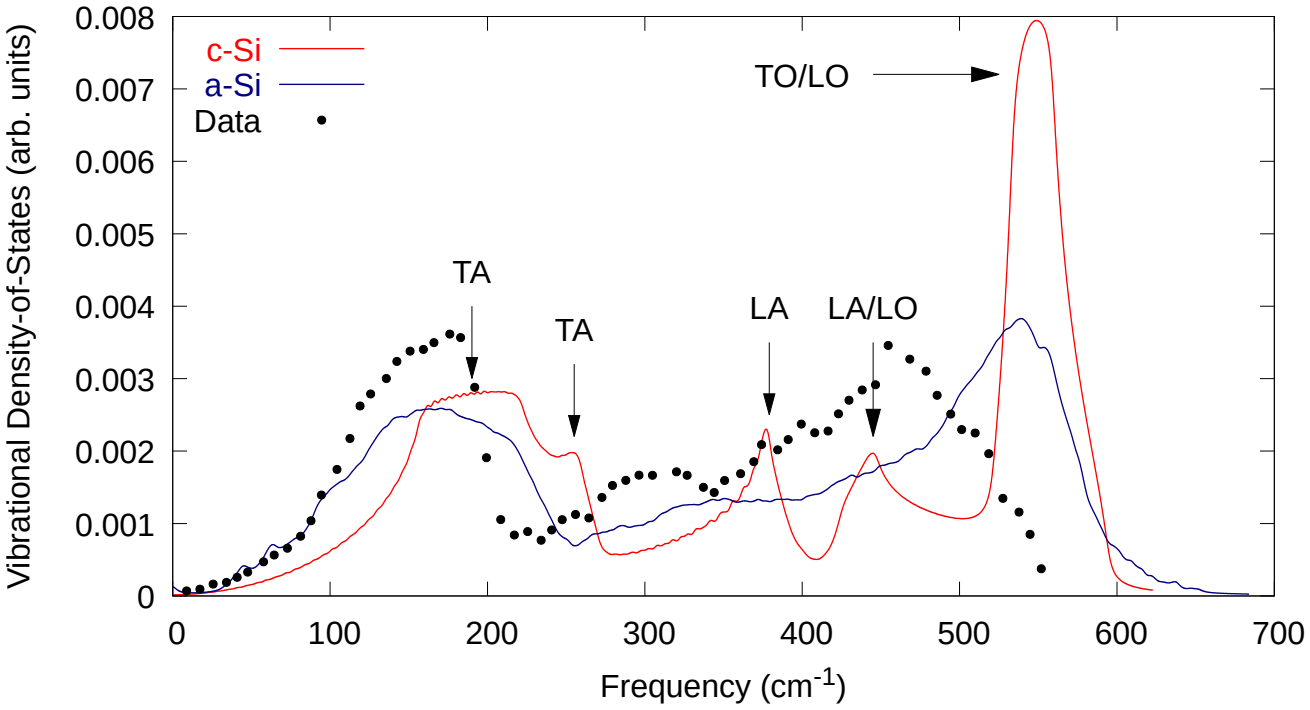

Figure 2.3: VDOS of crystalline (c-Si) and amorphous (α-Si) silicon normalized to unit intensity. Mode assignments adapted from [32]. INS data on α-Si adapted from [33]. Refer to Sect. 2.3.3 for details regarding the Si model.

There are three types of disorder which are of interest in this thesis: mass disorder, force constant (or bonding) disorder, and structural disorder. HEO is mass disordered since its cation sublattice is randomly populated by Mg, Co, Ni, Cu, and Zn. HEO is also force constant disordered, since *e.g.* the different cations interact with oxygen through different potentials (see Sect. 3.1 for details regarding the potential models employed here). As a counterexample, one could imagine a toy model HEO in which there is a single potential for all cation-oxygen interactions, and a single potential for all cation-cation interactions. Such a system would still be mass disordered, but not force constant disordered. Structural disorder, on the other hand, refers to systems without long-range crystalline order. Amorphous silicon is an example, but HEO is not, since it crystallizes in the rocksalt structure.

From the nonexistence of q it also follows that the classification of modes as either longitudinal/transverse (L/T) is also lost; *i.e.* there is no direction of propagation with respect to which a mode can vibrate transversely or longitudinally. Beltukov et al. have generalized L/T modes by considering Voronoi cells surrounding all atoms in a sample of amorphous silicon (α-Si). T-modes conserve the volume of the cells, while L-modes do not [34]. Similarly, with no well-defined disper-

sion relation, modes cannot be classified as acoustic ($\partial\omega_{qs}/\partial q \sim q$) or optical ($\partial\omega_{qs}/\partial q \sim$ const), where both derivatives are to be evaluated at $q = 0$. The appropriate generalization in this case is the 'phase quotient' introduced by Bell and Hibbins-Butler [35], which is applied to HEO in Sect. 4.2.2.

Allen and Feldman [36] and Allen et. al [37] proposed that the 'phonon gas' model of thermal conductivity in crystalline solids should be replaced by the taxonomy of propagons, diffusons, and locons in glasses. Propagons are extended, plane wave-like modes which generally occupy the lowest-frequency part of the VDOS, where q is still somewhat well-defined. The eigenvectors of a propagon are spatially coherent; *i.e.* the displacements of nearest-neighbours are strongly correlated. Conversely, the eigenvectors of a locon are randomly-oriented and the vibrations are confined to a region of finite spatial extent. In α-Si locons occupy the highest-frequency part of the VDOS, beyond the 'mobility edge' [37], although this is not a universal feature: a recent lattice dynamical study on amorphous polymers, for example, has shown that locons can exist at low frequencies and can actually dominate (at 90%) the total fraction of vibrational modes [38]. Diffusons, like propagons, are extended modes, but like locons, their eigenvectors are randomly-oriented. A wavepacket of diffusons transports energy diffusively, hence the nomenclature. A summary of the three types of vibrational excitations is sketched in Table 2.1.

Mode	Extended?	Frequency	Eigenvectors	Transport
Propagon	Yes	Low	Periodic	Ballistic
Diffuson	Yes	Medium	Random	Diffusive
Locon	No	High	Random	None

Table 2.1: Characteristics of propagons, diffusons, and locons.

2.2.3 Supercell Lattice Dynamics

One of the most common ways to study the lattice dynamics of a disordered solid is to build a 'supercell'; *i.e.* an extrusion of the primitive/conventional unit cell. An example of an HEO supercell was shown in Fig. 1.1. The larger the supercell is made, the more representative of a truly disordered material it becomes. It cannot be made arbitrarily large, however, for the computational resources required to diagonalize the dynamical matrix scales as N^3 [39]. Hence a balance must be struck between the desired accuracy of the calculation and the resources available to the user. The minimum size of the requisite supercell can be determined by ensuring all physical properties of interest are converged with respect to N.

An application of the supercell method to the VDOS of α-Si is shown in Fig. 2.3. For comparison, INS data on α-Si and the VDOS of crystalline silicon (c-Si) are also shown. The sharp peaks in the VDOS of c-Si are broadened in α-Si, but its general features are nonetheless preserved. This is also true of crystalline Ge, crystalline SiO_2, and their amorphous counterparts [40]. Allen et al. [37] note in particular that the diffuson modes in α-Si transition from having TA-like to LA-like character near 250 cm^{-1}, just as would be expected in c-Si.

2.3 Classical Wavepacket Dynamics

2.3.1 Motivation

The final column of Table 2.1 suggests that propagons, diffusons, and locons can be distinguished by studying the time-dependence of their energy transport. To make this idea precise, consider a wavepacket located at the centre of a large supercell. The wavepacket has been initialized by displacing some of the atoms while holding the rest at their equilibrium positions. See Fig. 2.4 in Sect. 2.3.4 for an illustration. All of the atoms initially have zero momentum, so the only energy stored in the supercell is potential. At time $t = 0$, the atoms are suddenly released and the wavepacket is allowed to propagate.

If the wavepacket consisted of propagons, the wavefront should spread linearly in time at something like the sound velocity; *i.e.* $\langle r \rangle \sim t$ and consequently $\langle r^2 \rangle \sim t^2$, where the average $\langle \cdot \rangle$ is taken over all atoms in the supercell. Similarly, if the wavepacket consisted of diffusons, the wavefront should spread diffusively; $\langle r^2 \rangle \sim t$. Lastly, if the wavepacket consisted of locons, then the wavefront should not spread at all; $\langle r^2 \rangle \sim$ const. Define now at each time t a diffusion coefficient [41]

$$D(t) = \frac{\langle r^2(t) \rangle - \langle r^2(0) \rangle}{t} \tag{2.27}$$

It follows from the preceding discussion that by studying the dependence of $D(t)$ on t it should be possible to discriminate between the three types of modes. The results are summarized in Table 2.2. However, it is not clear at this stage how to calculate $\langle r^2 \rangle$. This is taken up in Sects. 2.3.2 and 2.3.3.

$D(t)$	Mode
t	Propagon
const.	Diffuson
t^{-1}	Locon

Table 2.2: Expected time dependence of the diffusion coefficient.

2.3.2 General Theory

The general solution to the equations of motion Eq. 2.7 was given in Eq. 2.16 and is

$$u_\alpha(\ell b; t) = \frac{1}{\sqrt{N m_b}} \sum_{qs} A_{qs}\, \varepsilon_\alpha(b; qs)\, \exp[i\,(q \cdot \ell - \omega_{qs} t)]$$

where the explicit time dependence of the $\{u\}$ has been restored. Physically, $u_\alpha(\ell b; t)$ is the displacement of the atom (ℓb) away from equilibrium and must be real-valued at all times. This constraint

can be enforced by adding to Eq. 2.16 its complex conjugate and halving the result:

$$\begin{aligned} u_\alpha(\ell b;t) &\stackrel{!}{=} \frac{1}{2\sqrt{Nm_b}} \sum_{qs} \left[A_{qs}\, \varepsilon_\alpha(b;qs)\, \exp\{i\,(q\cdot\ell - \omega_{qs}t)\} + A^*_{qs}\, \varepsilon^*_\alpha(b;qs)\, \exp\{-i\,(q\cdot\ell - \omega_{qs}t)\} \right] \\ &= \frac{1}{2\sqrt{Nm_b}} \sum_{qs} \left[A_{qs}\, \varepsilon_\alpha(b;qs)\, \exp\{i\,(q\cdot\ell - \omega_{qs}t)\} + A^*_{qs}\, \varepsilon_\alpha(b;-qs)\, \exp\{-i\,(q\cdot\ell - \omega_{qs}t)\} \right] \\ &= \frac{1}{2\sqrt{Nm_b}} \sum_{qs} \varepsilon_\alpha(b;qs) \left[A_{qs}\, \exp(-i\omega_{qs}t) + A^*_{-qs}\, \exp(i\omega_{qs}t) \right] \exp(iq\cdot\ell) \\ &= \frac{1}{\sqrt{Nm_b}} \sum_{qs} \varepsilon_\alpha(b;qs)\, Q(qs;t)\, \exp(iq\cdot\ell) \end{aligned}$$

The second line follows from the relation Eq. 2.18 between an eigenvector and its complex conjugate; the third line follows by replacing $q \to -q$ in the summation and using the time-reversal symmetry relation Eq. 2.17. In the final line the 'normal coordinates' defined by

$$Q(qs;t) = \frac{1}{2} \left[A_{qs}\, \exp(-i\omega_{qs}t) + A^*_{-qs}\, \exp(i\omega_{qs}t) \right] \tag{2.28}$$

have been introduced. It may be seen that the general solution involves $2dpN$ unknowns, which can be taken either as the the real and imaginary parts of the $\{A_{qs}\}$, or more conveniently, as the values of $\{Q(qs;t), \dot{Q}(qs;t)\}$ at time $t = 0$. This is precisely the information provided by the $2dpN$ initial positions and velocities $\{u_\alpha(\ell b;0), \dot{u}_\alpha(\ell b;0)\}$. The transformation between the two sets of unknowns is effected by solving the matrix equation:

$$\begin{pmatrix} Q(qs;0) \\ \dot{Q}(qs;0) \end{pmatrix} = \frac{1}{2} \begin{pmatrix} 1 & 1 \\ -i\omega_{qs} & i\omega_{qs} \end{pmatrix} \begin{pmatrix} A_{qs} \\ A^*_{-qs} \end{pmatrix} \iff \begin{pmatrix} A_{qs} \\ A^*_{-qs} \end{pmatrix} = \frac{1}{i\omega_{qs}} \begin{pmatrix} i\omega_{qs} & -1 \\ i\omega_{qs} & 1 \end{pmatrix} \begin{pmatrix} Q(qs;0) \\ \dot{Q}(qs;0) \end{pmatrix} \tag{2.29}$$

Substituting Eq. 2.29 into Eq. 2.28, the normal coordinates are equivalently expressed as

$$Q(qs;t) = Q(qs;0)\, \cos\omega_{qs}t + \frac{\dot{Q}(qs;0)}{\omega_{qs}}\, \sin\omega_{qs}t \tag{2.30}$$

and the displacements are given by

$$u_\alpha(\ell b;t) = \frac{1}{\sqrt{Nm_b}} \sum_{qs} \varepsilon_\alpha(b;qs) \left[Q(qs;0)\, \cos\omega_{qs}t + \frac{\dot{Q}(qs;0)}{\omega_{qs}}\, \sin\omega_{qs}t \right] \exp(iq\cdot\ell) \tag{2.31}$$

The $\{Q(qs;0), \dot{Q}(qs;0)\}$ can also be written in terms of the initial values of the displacements and velocities themselves as follows:

$$u_\alpha(\ell b;0) = \frac{1}{\sqrt{Nm_b}} \sum_{qs} \varepsilon_\alpha(b;qs)\, Q(qs;0)\, \exp(iq\cdot\ell)$$

$$\sum_\ell u_\alpha(\ell b;0)\, \exp(-iq'\cdot\ell) = \frac{1}{\sqrt{Nm_b}} \sum_{qs} \varepsilon_\alpha(b;qs)\, Q(qs;0) \underbrace{\sum_\ell \exp[i\,(q-q')\cdot\ell]}_{N\delta_{q-q',0}}$$

$$= \sqrt{\frac{N}{m_b}} \sum_s \varepsilon_\alpha(b;q's)\, Q(q's;0)$$

The second line follows from multiplying through by $\exp(-iq'\cdot\ell)$ and summing over ℓ. Moving the prefactor $\sqrt{N/m_b}$ to the left-hand side, multiplying by $\varepsilon^*_\alpha(b;q's')$, and performing a second summation over $b\alpha$ produces

$$\frac{1}{\sqrt{N}} \sum_{b\alpha} \sqrt{m_b}\, \varepsilon^*_\alpha(b;q's') \sum_\ell u_\alpha(\ell b;0)\, \exp(-iq'\cdot\ell) = \underbrace{\sum_{b\alpha} \varepsilon^*_\alpha(b;q's')\, \varepsilon_\alpha(b;q's)}_{\delta_{ss'}}\, Q(q's;0) = Q(q's';0)$$

where $\delta_{ss'}$ arises from the completeness relation Eq. 2.15. An analogous expansion of the $\{\dot{Q}(qs;0)\}$ in terms of the $\{\dot{u}_\alpha(\ell b;0)\}$ can be derived by differentiating both sides of Eq. 2.31 with respect to time and evaluating the result at $t=0$. In summary, the expansions are

$$Q(qs;0) = \frac{1}{\sqrt{N}} \sum_{b\alpha} \sqrt{m_b}\, \varepsilon^*_\alpha(b;qs) \sum_\ell u_\alpha(\ell b;0)\, \exp(-iq\cdot\ell) \tag{2.32}$$

$$\dot{Q}(qs;0) = \frac{1}{\sqrt{N}} \sum_{b\alpha} \sqrt{m_b}\, \varepsilon^*_\alpha(b;qs) \sum_\ell \dot{u}_\alpha(\ell b;0)\, \exp(-iq\cdot\ell) \tag{2.33}$$

2.3.3 Dynamics in a Large Supercell

Consider a crystal described by a supercell. If the supercell is made large enough, then to first approximation $N=1$, the only lattice site is $\ell=0$, and the Brillouin zone consists of the single point $q=0$. Suppose further that all atoms are initially at rest. Then the left-hand side of Eq. 2.33 vanishes and Eqns. 2.31 and 2.32 can be combined into the single equation

$$u_\alpha(b;t) = \frac{1}{\sqrt{m_b}} \sum_s \varepsilon_\alpha(b;s)\, \cos\omega_s t \sum_{b'\alpha'} \sqrt{m_{b'}}\, \varepsilon^*_{\alpha'}(b';s)\, u_{\alpha'}(b';0) \tag{2.34}$$

where the labels $\ell = q = 0$ have been discarded. Future algebraic manipulations will be made considerably easier if Eq. 2.34 is recast as a matrix equation. Here the Dirac notation used by Allen

and Kelner [42] in the context of vibrational wavepackets is introduced by the correspondence rules:

$$\begin{aligned} u_\alpha(b;t) &\longleftrightarrow \langle b\alpha|u(t)\rangle \\ \varepsilon_\alpha(b;s) &\longleftrightarrow \langle b\alpha|s\rangle \\ \varepsilon^*_\alpha(b;s) &\longleftrightarrow \langle s|b\alpha\rangle \\ \cos\omega_s t\,\delta_{ss'} &\longleftrightarrow \langle s|\hat{C}(t)|s'\rangle \\ m_{b\alpha}\,\delta_{\alpha\alpha'}\delta_{bb'} &\longleftrightarrow \langle b\alpha|\hat{M}|b'\alpha'\rangle \end{aligned}$$

The $\{|b\alpha\rangle\}$ are vectors in direct space, while the $\{|s\rangle\}$ are vectors in the eigenbasis of the dynamical matrix. In the fourth line an operator $\hat{C}(t)$ has been introduced which is diagonal in the eigenbasis and whose eigenvalues are the $\{\cos\omega_s t\}$. The fifth line is more subtle: each component of a given atomic displacement is obviously weighted by the same mass, so there is no harm in writing $m_b \to m_{b\alpha}$. The $\{m_{b\alpha}\}$ are the eigenvalues of the 'mass operator' $\hat{M}$ which is diagonal in direct space. In the Dirac notation, the orthonormality and completeness relations Eqns. 2.14 and 2.15 relations read, respectively

$$\sum_{b\alpha} \langle s|b\alpha\rangle\,\langle b\alpha|s'\rangle = \langle s|s'\rangle = \delta_{ss'} \tag{2.35}$$

$$\sum_{s} \langle s|b\alpha\rangle\,\langle b'\alpha'|s\rangle = \langle b'\alpha'|b\alpha\rangle = \delta_{\alpha\alpha'}\,\delta_{bb'} \tag{2.36}$$

Similarly, Eq. 2.34 now reads:

$$\begin{aligned} \langle b\alpha|u(t)\rangle &= \frac{1}{\sqrt{m_b}} \sum_s \langle b\alpha|s\rangle\,\cos\omega_s t \sum_{b'\alpha'} \sqrt{m_{b'}}\,\langle s|b'\alpha'\rangle\,\langle b'\alpha'|u(0)\rangle \\ &= \frac{1}{\sqrt{m_b}} \sum_s \langle b\alpha|s\rangle \left(\sum_{s'} \delta_{ss'}\,\cos\omega_{s'} t\right) \sum_{b'\alpha'} \sqrt{m_{b'}}\,\langle s|b'\alpha'\rangle\,\langle b'\alpha'|u(0)\rangle \\ &= \frac{1}{\sqrt{m_b}} \sum_{ss'} \langle b\alpha|s\rangle\;\langle s|\hat{C}(t)|s'\rangle \sum_{b'\alpha'} \sqrt{m_{b'}}\,\langle s'|b'\alpha'\rangle\,\langle b'\alpha'|u(0)\rangle \\ &= \left(\sum_{b''\alpha''} \langle b\alpha|\hat{M}^{-\frac{1}{2}}|b''\alpha''\rangle\right) \sum_{ss'} \langle b\alpha|s\rangle\;\langle s|\hat{C}(t)|s'\rangle \sum_{b'\alpha'} \left(\sum_{b'''\alpha'''} \langle b'\alpha'|\hat{M}^{\frac{1}{2}}|b'''\alpha''\rangle\right) \langle s'|b'\alpha'\rangle\,\langle b'\alpha'|u(0)\rangle \\ &= \left(\sum_{b''\alpha''} \langle b\alpha|\hat{M}^{-\frac{1}{2}}|b''\alpha''\rangle\right) \sum_{ss'} \langle b''\alpha''|s\rangle\;\langle s|\hat{C}(t)|s'\rangle \sum_{b'\alpha'} \left(\sum_{b'''\alpha'''} \langle b'\alpha'|\hat{M}^{\frac{1}{2}}|b'''\alpha''\rangle\right) \langle s'|b'\alpha'\rangle\,\langle b'''\alpha'''|u(0)\rangle \\ &= \left(\sum_{b'\alpha'} \langle b\alpha|\hat{M}^{-\frac{1}{2}}|b'\alpha'\rangle\right) \sum_{ss'} \langle b'\alpha'|s\rangle\;\langle s|\hat{C}(t)|s'\rangle \sum_{b''\alpha''} \left(\sum_{b'''\alpha'''} \langle b''\alpha''|\hat{M}^{\frac{1}{2}}|b'''\alpha'''\rangle\right) \langle s'|b''\alpha''\rangle\,\langle b'''\alpha'''|u(0)\rangle \\ &= \sum_{ss'} \sum_{b'\alpha'} \sum_{b''\alpha''} \sum_{b'''\alpha'''} \langle b\alpha|\hat{M}^{-\frac{1}{2}}|b'\alpha'\rangle\,\langle b'\alpha'|s\rangle\;\langle s|\hat{C}(t)|s'\rangle\,\langle s'|b''\alpha''\rangle\;\langle b''\alpha''|\hat{M}^{\frac{1}{2}}|b'''\alpha'''\rangle\,\langle b'''\alpha'''|u(0)\rangle \end{aligned}$$

The replacement $\langle s|b\alpha\rangle \to \langle s'|b\alpha\rangle$ is made in the third line with impunity since the delta function enforces $s = s'$. For the same reason, $\langle b\alpha|s\rangle \to \langle b''\alpha''|s\rangle$ and $\langle b'\alpha'|u(0)\rangle \to \langle b'''\alpha'''|u(0)\rangle$ in the fifth line. The penultimate line follows from exchanging the primed and doubly-primed $(b\alpha)$ indices.

Summation over dyads $|b\alpha\rangle\langle b\alpha|$ and $|s\rangle\langle s|$ generates resolutions of unity by Eqns. 2.35 and 2.36.

Furthermore, since the above holds for any bra $\langle b\alpha|$, it can be very succinctly written as

$$|u(t)\rangle = \hat{M}^{-\frac{1}{2}}\hat{C}(t)\hat{M}^{\frac{1}{2}}\,|u(0)\rangle \tag{2.37}$$

which generalizes Allen and Kelner's results for a 1D chain with constant mass to arbitrary mass- and force-constant disorder in d dimensions. The direct translation of the foregoing (*i.e.* without summation over dyads) reads

$$\mathbf{u}(t) = \mathbf{M}^{-\frac{1}{2}}\boldsymbol{\varepsilon}\mathbf{C}(t)\boldsymbol{\varepsilon}^{\dagger}\mathbf{M}^{\frac{1}{2}}\mathbf{u}(0) \tag{2.38}$$

where $\boldsymbol{\varepsilon}$ is a unitary matrix whose columns are the vibrational eigenvectors. Eq. 2.37 has the advantage of holding in any basis whatsoever; Eq. 2.38 is more useful in practical computations, where only certain matrix elements are known. One would probably not know, for instance, the initial displacements in the eigenbasis; *i.e.* the column vector $\langle s|u(0)\rangle$. Differentiating Eq. 2.38 with respect to time, the velocities of the atoms are

$$|v(t)\rangle = -\hat{M}^{-\frac{1}{2}}\hat{\Omega}\hat{S}(t)\hat{M}^{\frac{1}{2}}\,|u(0)\rangle \tag{2.39}$$

where $\hat{S}$ and $\hat{\Omega}$ are diagonal in the eigenbasis with eigenvalues $\{\sin\omega_s t\}$ and $\{\omega_s\}$, respectively. The same formula is given in the 'conventional' matrix-vector notation as

$$\mathbf{v}(t) = -\mathbf{M}^{-\frac{1}{2}}\boldsymbol{\varepsilon}\boldsymbol{\Omega}\mathbf{S}(t)\boldsymbol{\varepsilon}^{\dagger}\mathbf{M}^{\frac{1}{2}}\mathbf{u}(0) \tag{2.40}$$

Following Allen and Kelner, consider now the vector

$$|W(t)\rangle = \hat{M}^{\frac{1}{2}}\,|v(t)\rangle - i\hat{\Omega}\hat{M}^{\frac{1}{2}}\,|u(t)\rangle \tag{2.41}$$

whose physical significance will soon become apparent. The amplitude of $|W(t)\rangle$ is

$$\langle W(t)|W(t)\rangle = \langle v(t)|\hat{M}|v(t)\rangle + \langle u(t)|\hat{M}^{\frac{1}{2}}\hat{\Omega}^2\hat{M}^{\frac{1}{2}}|u(t)\rangle \tag{2.42}$$

where use has been made of the fact that $\hat{\Omega}, \hat{M}$ are Hermitian operators to eliminate the cross terms. The first term on the right-hand side of Eq. 2.42 is equal to twice the kinetic energy of the crystal:

$$\begin{aligned}
2T &= \sum_{b\alpha} m_b\,\dot{u}_\alpha(b;t)^2 \\
&= \sum_{b\alpha}\dot{u}_\alpha(b;t)\left(\sum_{b'\alpha'} m_{b\alpha}\,\delta_{\alpha\alpha'}\,\delta_{bb'}\right)\dot{u}_\alpha(b;t) \\
&= \sum_{b\alpha}\sum_{b'\alpha'}\langle v(t)|b\alpha\rangle\;\langle b\alpha|\hat{M}|b'\alpha'\rangle\,\langle b'\alpha'|v(t)\rangle \\
&= \langle v(t)|\hat{M}|v(t)\rangle
\end{aligned}$$

Note in the third line that $\langle b\alpha|v(t)\rangle = \langle b\alpha|v(t)\rangle^*$, which follows from the reality of the atomic velocities. It will now be shown that the second term on the right-hand side of Eq. 2.42 is equal to twice the potential energy. To prove this, it is first noted that, by construction, the dynamical matrix is diagonal in the eigenbasis:

$$\hat{D} = \hat{D}\sum_s |s\rangle\langle s| = \sum_s \omega_s^2\,|s\rangle\langle s| = \hat{\Omega}^2 \tag{2.43}$$

Also, when specialized to the large supercell, Eq. 2.13 reduces to

$$D_{\alpha\alpha'}(bb') = \frac{\Phi_{\alpha\alpha'}(bb')}{\sqrt{m_b m_{b'}}} \tag{2.44}$$

The potential energy is then

$$\begin{aligned}
2\Phi &= \sum_{b\alpha}\sum_{b'\alpha'} u_\alpha(b;t)\,\Phi_{\alpha\alpha'}(bb')\,u_{\alpha'}(b';t) \\
&= \sum_{b\alpha}\sum_{b'\alpha'} u_\alpha(b;t)\,\sqrt{m_b m_{b'}}\,D_{\alpha\alpha'}(bb')\,u_{\alpha'}(b';t) \\
&= \sum_{b\alpha}\sum_{b'\alpha'} u_\alpha(b;t)\left(\sum_{b''\alpha''}\langle b\alpha|\hat{M}^{\frac{1}{2}}|b''\alpha''\rangle\right) D_{\alpha\alpha'}(bb')\left(\sum_{b'''\alpha'''}\langle b'\alpha'|\hat{M}^{\frac{1}{2}}|b'''\alpha'''\rangle\right) u_{\alpha'}(b';t) \\
&= \sum_{b\alpha}\sum_{b'\alpha'}\sum_{b''\alpha''}\sum_{b'''\alpha'''} \langle u(t)|b\alpha\rangle\ \langle b\alpha|\hat{M}^{\frac{1}{2}}|b''\alpha''\rangle\ \langle b\alpha|\hat{D}|b'\alpha'\rangle\ \ \langle b'\alpha'|\hat{M}^{\frac{1}{2}}|b'''\alpha'''\rangle\,\langle b'\alpha'|u(t)\rangle \\
&= \sum_{b\alpha}\sum_{b'\alpha'}\sum_{b''\alpha''}\sum_{b'''\alpha'''} \langle u(t)|b\alpha\rangle\ \langle b\alpha|\hat{M}^{\frac{1}{2}}|b''\alpha''\rangle\ \langle b''\alpha''|\hat{D}|b'\alpha'\rangle\ \ \langle b'\alpha'|\hat{M}^{\frac{1}{2}}|b'''\alpha'''\rangle\,\langle b'''\alpha'''|u(t)\rangle \\
&= \sum_{b\alpha}\sum_{b'\alpha'}\sum_{b''\alpha''}\sum_{b'''\alpha'''} \langle u(t)|b\alpha\rangle\ \langle b\alpha|\hat{M}^{\frac{1}{2}}|b'\alpha'\rangle\ \langle b'\alpha'|\hat{D}|b''\alpha''\rangle\ \ \langle b''\alpha''|\hat{M}^{\frac{1}{2}}|b'''\alpha'''\rangle\,\langle b'''\alpha'''|u(t)\rangle \\
&= \langle u(t)|\hat{M}^{\frac{1}{2}}\hat{D}\hat{M}^{\frac{1}{2}}|u(t)\rangle
\end{aligned}$$

which is indeed equal to the second term on the right-hand side of Eq. 2.42 once the replacement $\hat{D} = \hat{\Omega}^2$ is made using Eq. 2.43. Thus

$$\langle W(t)|W(t)\rangle = 2T + 2\Phi = 2E \tag{2.45}$$

i.e. the overlap $\langle W(t)|W(t)\rangle$ it is an integral of the motion, equal to twice the total energy E of the crystal. Inserting a resolution of unity:

$$\langle W(t)|W(t)\rangle = \sum_{b\alpha}\langle W(t)|b\alpha\rangle\,\langle b\alpha|W(t)\rangle = \sum_{b\alpha}|\langle b\alpha|W(t)\rangle|^2$$

which suggests that a reasonable, additive definition of the on-site energy is

$$\epsilon_\alpha(b;t) = \frac{1}{2}\,|\langle b\alpha|W(t)\rangle|^2 \tag{2.46}$$

The wavepacket width introduced in Sect. 2.3.1 can finally be written as

$$\left\langle r^2(t)\right\rangle = \frac{1}{E}\sum_{b\alpha}\left[b_\alpha - R_\alpha(t)\right]^2\epsilon_\alpha(b;t) \tag{2.47}$$

where $R(t)$ is the center-of-energy of the wavepacket defined by

$$R_\alpha(t) = \frac{1}{E}\sum_{b} b_\alpha\,\epsilon_\alpha(b;t) \tag{2.48}$$

Both Eqns. 2.47 and 2.48 are again generalizations of Allen and Kelner's results. To find $\langle r^2(t)\rangle$ it

is necessary to know $|W(t)\rangle$, which can be calculated from the initial displacements as follows:

$$\begin{aligned}
|W(t)\rangle &= \hat{M}^{\frac{1}{2}} |v(t)\rangle - i\hat{\Omega}\hat{M}^{\frac{1}{2}} |u(t)\rangle \\
&= -\hat{\Omega}\left[\hat{S}(t) + i\hat{C}(t)\right] \hat{M}^{\frac{1}{2}} |u(0)\rangle \\
&= -i\hat{\Omega}\left[\hat{C}(t) - i\hat{S}(t)\right] \hat{M}^{\frac{1}{2}} |u(0)\rangle \\
&= \left[\hat{C}(t) - i\hat{S}(t)\right] \left(-i\hat{\Omega}\hat{M}^{\frac{1}{2}} |u(0)\rangle\right) \\
&= e^{-i\hat{\Omega}t} |W(0)\rangle \\
&= \hat{\mathcal{U}}(t) |W(0)\rangle
\end{aligned}$$

The second line follows from the definitions of the atomic displacements and velocities Eqns. 2.38 and 2.39. In the fourth line the fact that $\hat{\Omega}, \hat{C}, \hat{S}$ are all diagonal in the eigenbasis has been used to commute the multiplications $\hat{\Omega}\hat{C}$ and $\hat{\Omega}\hat{S}$.

2.3.4 Wavepacket Dynamics and Localization

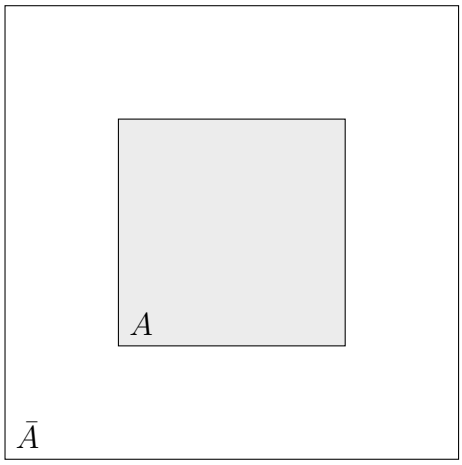

Figure 2.4: Supercell of HEO A wrapped in an environment of HEO $\bar{A}$. All the atoms in A are initially displaced, while all the atoms in $\bar{A}$ are fixed to the equilibrium positions. The result is a wavepacket (A) which has been initialized with potential energy only.

Consider a cubic supercell A of HEO embedded in the centre of an HEO environment. The union of A and its environment $\bar{A}$ is a larger supercell of HEO which is denoted by B. If A is not too small, $\bar{A}$ should not look too dissimilar from periodic repetitions of A itself. In other words, a mode which was a locon in A should still approximately be localized in B, and similarily for propagons and diffusons. The setup is illustrated in Fig. 2.4. At time $t = 0$ all the atoms in $\bar{A}$ are fixed to zero initial displacement, while all the atoms in A are displaced in proportion to one of eigenmodes of A. The initial displacements of B are given symbolically by

$$|u(0)\rangle = \hat{M}^{-\frac{1}{2}} |0 \cup s_A\rangle \implies |W(0)\rangle = \hat{\Omega} |0 \cup s_A\rangle \tag{2.49}$$

when $|0 \cup s_A\rangle$ is a vector whose components in the eigenbasis are equal to zero if an atom $b \in \bar{A}$ and is equal to an eigenvector component of mode s_A if $b \in A$. The relation between $|u(t)\rangle$ and

$|0 \cup s_A\rangle$ follows from Eq. 2.11. Evolving $|W(0)\rangle$ forward in time with $\hat{\mathcal{U}}(t)$ produces

$$\begin{aligned}\langle b\alpha|W(t)\rangle &= \langle b\alpha|\hat{\mathcal{U}}(t)\hat{\Omega}|0 \cup s_A\rangle \\ &= \langle b\alpha|\left(\sum_s |s\rangle\langle s|\right)\hat{\mathcal{U}}(t)\hat{\Omega}\left(\sum_{s'} |s'\rangle\langle s'|\right)\left(\sum_{b'\alpha'} |b'\alpha'\rangle\langle b'\alpha'|\right)|0 \cup s_A\rangle \\ &= \sum_{ss'}\sum_{b'\alpha'} \langle b\alpha|s\rangle\ \langle s|\hat{\mathcal{U}}(t)\hat{\Omega}|s'\rangle\ \langle s'|b'\alpha'\rangle\ \langle b'\alpha'|0 \cup s_A\rangle\end{aligned}$$

In the 'classical' matrix-vector notation, this reads

$$\mathbf{W}(t) = \boldsymbol{\varepsilon}\,\boldsymbol{\mathcal{U}}(t)\,\boldsymbol{\Omega}\,\boldsymbol{\varepsilon}^\dagger\,\mathbf{s}_A \tag{2.50}$$

The on-site energies and wavepacket width Eqns. 2.46 and 2.47 can be calculated at once from the components $\{\langle b\alpha|W(t)\rangle\}$. The diffusion coefficient Eq. 2.27, which is a function of $\langle r^2\rangle$ only, discriminates between propagons, diffusons, and locons according to the predictions of Table 2.2.

2.3.5 Correlation Amplitude

The correlation amplitude in quantum mechanics measures the similarity of state $|\Psi(t)\rangle$ at time t to the initial state $|\Psi(0)\rangle$ at time $t = 0$. Since $|W(t)\rangle$ obeys the Schrödinger equation for state kets

$$|W(t)\rangle = \hat{\mathcal{U}}(t)\,|W(0)\rangle \tag{2.51}$$

it is the Newtonian analogue of the state of a quantum system. Note in this analogy that the operator $\hat{\mathcal{U}}(t)$ plays the role of the quantum propagator for a time-independent potential (the potential must be time-independent, since the total energy of the crystal is conserved). A correlation amplitude for the wavepacket can therefore be defined as

$$\begin{aligned}\langle W(t)|W(0)\rangle &= \langle W(0)|\hat{\mathcal{U}}(t)|W(0)\rangle \\ &= \langle 0 \cup s_A|\hat{\Omega}\hat{\mathcal{U}}(t)\,\hat{\Omega}|0 \cup s_A\rangle \\ &= \sum_{b\alpha}\sum_{b'\alpha'}\sum_{ss's''s'''} \langle 0 \cup s_A|b\alpha\rangle\,\langle b\alpha|s\rangle\ \langle s|\hat{\Omega}|s'\rangle\ \langle s'|\hat{\mathcal{U}}(t)|s''\rangle\ \langle s''|\hat{\Omega}|s'''\rangle\,\langle s'''|b'\alpha'\rangle\,\langle b'\alpha'|0 \cup s_A\rangle\end{aligned}$$

or, in the classical notation, as the quadratic form

$$\mathbf{W}^*(t)\cdot\mathbf{W}(0) = \left(\boldsymbol{\Omega}^T\,\varepsilon^\dagger\,\mathbf{s}_A\right)^T\boldsymbol{\mathcal{U}}(t)\left(\boldsymbol{\Omega}^T\,\varepsilon^\dagger\,\mathbf{s}_A\right) \tag{2.52}$$

Physically, a locon should not spread far in space and should closely resemble its initial state after a long time t. The opposite is true of propagons and diffusons. Hence a correlation amplitude which is close to unity (in modulus) for all time gives further evidence for the existence of localized modes. Eq. 2.52 is also much faster (numerically) to evaluate than Eq. 2.50, since the large matrices $\boldsymbol{\varepsilon}$ appear only in matrix-vector multiplications with the initial state $\mathbf{s}_A$, which contains mostly zeros.

Chapter 3

Methods

3.1 Interatomic Potentials

Due to the complicated nature of chemical bonding, the interaction energy Φ introduced in Sect. 2.1 is not known *a priori* in any real material. To diagonalize the dynamical matrix Eq. 2.13 it is therefore necessary to choose, on the basis of ionic vs. covalent bonding, and agreement with experimental data, a reasonable functional form of Φ. In this work, it is assumed that the short-range interaction between atoms located at b, b' is given by the pairwise Buckingham potential

$$\Phi(x_{bb'}) = A_{bb'} \exp\left(-\frac{x_{bb'}}{\rho_{bb'}}\right) - \frac{C_{bb'}}{x_{bb'}^6} \qquad x_{bb'} = |b - b'| \tag{3.1}$$

where the two terms on the right-hand side represent, respectively, the repulsion between overlapping electron clouds and the van-der-Waals attraction between fluctuating dipoles. The constants $\{A, \rho, C\}$ depend on the species of atoms b, b' under consideration and vary between materials. Use of the Buckingham potential is ubiquitous in lattice dynamical studies on metal oxides. The effects of atomic polarisability are accounted for with the shell model discussed in Sect. 2.1.5. For simplicity, the sum of the core and shell charges is fixed to the formal charge on each ion, either $+2$ or -2 for the cations and oxygen, respectively. It is important to emphasize that shell-shell interactions are parametrized by Eq. 3.1, while a core and its shell interact via Eq. 2.21. The Coulomb potential acts between all pairs of cores and shells.

For HEO with 5 species of cations and its oxygen sublattice, the number of Buckingham potentials required to parametrize all shell-shell interactions is $\frac{1}{2}6(6+1) = 21$, each contributing 3 unknowns $\{A, \rho, C\}$. The core/shell pairs further contribute another 6×2 unknowns $\{Y, k\}$. Thus the total number of unknown numerical constants, which must be determined from a fit to experimental data, is 75. This exceeds the number of recorded HEO observables (cf. [6] for a review). Further assumptions therefore need to be made to proceed with the lattice dynamical approach. The remainder of this section is devoted to an exposition of these assumptions and their justifications.

> *Assumption 1: The Buckingham potentials describing the shell-shell interactions in the parent binary oxides are directly transferable to HEO. Thus the Mg–O interaction in HEO is assumed to be the same as the Mg–O interaction in MgO, and so forth. Likewise, the Mg core and shell parameters in MgO are directly transferable to HEO.*

Since HEO is itself synthesized from a powderized mixture of its parent binary oxides, this assumption is physically sensible. The impetus of this assumption, however, is mostly practical: the binary oxide observables are more bountiful than the HEO observables.

> *Assumption 2: Cations interact only with oxygen (and not amongst themselves).*

Lewis & Catlow [43] found satisfactory agreement between the simulated and experimental elastic constants of spinel oxides by neglecting cation-cation interactions and using Assumption 1 to fit their cation-oxygen potentials. HEO should better conform to Assumption 2 than spinel since, for

the binary oxides MgO, CoO, and NiO, there is no difference in coordination [19]. Assumption 2 has the added advantage of reducing the number of unknowns from 75 to 30.

Assumption 3: The Buckingham O–O parameters are taken from Lewis & Catlow.

The Buckingham O–O interaction and the oxygen core/shell parameters must be the same in the binary oxides and HEO; *i.e.* an oxygen in MgO, CoO, *etc.*, is the same as an oxygen in HEO. It is reasonable to fix the O–O parameters at the values determined by Lewis & Catlow since they are highly transferable [44] and in widespread use. The oxygen core/shell parameters were allowed to vary in the fit to improve the agreement with experimental data (see Sect. 3.4 and Table 3.3), but did not deviate far from the Lewis & Catlow values. Assumption 3 further reduces the number of unknowns from 30 to 27.

Assumption 4: The van der Waals term is nonzero only for the O–O interaction.

No improvement in the fit quality was observed by attempting to graft nonzero $C_{bb'}$ terms onto existing cation-oxygen potentials. Physically, oxygen is larger and more polarisable than the metal cations in HEO, and should therefore have the strongest dipole-dipole interaction [45]. There are 22 unknowns left after making Assumption 4: ten cation-oxygen Buckingham parameters $\{A, \rho\}$, and two shell model parameters $\{Y, k\}$ for each of the six ions in HEO.

3.2 The `General Utility Lattice Program (GULP)`

`GULP` is a classical lattice dynamics program designed to run a variety of simulations on zero-dimensional (*i.e.* isolated molecules) up to three-dimensional (bulk) materials [39]. In this thesis, `GULP` was used use to fit the Buckingham/shell model potentials introduced in Sects. 2.1.5 and 3.1 to experimental data on the parent binary oxides MgO, CoO, NiO, CuO, and ZnO. The precise way in which this was done is explained in Sect. 3.4. `GULP` was also used to diagonalize the dynamical matrix of HEO supercells and extract its eigenfrequencies/vectors, from which the various probes for vibrational mode localization in Sect. 4.3 were calculated.

To run a `GULP` simulation, the user must input the crystal structure (*i.e.* lattice parameters and internal coordinates) as well as all relevant interatomic potentials for the material under consideration. The user must also specify in the `keyword` section what properties they are interested in calculating. If phonon properties are requested, as here, `GULP` includes an option to write any of the eigenfrequencies/vectors, VDOS, dispersion, dynamical matrix, and/or force constants to file.

3.3 The Need for New Potentials

Anand et al. [18] and Chen et al. [19] have previously applied `GULP` to HEO to study its thermodynamics and the mechanical effects of Li dopant, respectively. Both have taken the Zn–O, Co–O, and Ni–O potentials from Table 1 of Lewis & Catlow [43]; Chen et al. have derived Mg–O and Cu–O potentials by fitting to the binary oxides' elastic and dielectric constants, while Anand et al. have adopted the Cu–O potential from a lattice-dynamical study of Hg-based superconductors [46]. Anand et al. are not clear about which Mg–O potential they use.

None of these sets of potentials are entirely appropriate for a lattice-dynamical study of the vibrations in HEO. The Lewis & Catlow (Table 1) cation-oxygen potentials were derived by assuming a constant value of ρ and determining A from a fit to the binary oxides' lattice constants. They do not take into account additional experimental data (*i.e.* dielectric constants and phonon frequencies)

which are available for ZnO, CoO, and NiO. The Cu–O potential from Anand et al. was derived by fitting to the structural data available for select Hg-based superconductors and may not be transferable to other materials. Lastly, it can be rigorously shown [47] that central potentials lead invariably to the Cauchy relation $C_{12} = C_{44}$ between elastic constants which is violated by the binary oxides; see Table 3.1 for experimental data. The Mg–O and Cu–O potentials from Chen et al. are therefore too simplistic to quantitatively reproduce the binary oxides' elastic constants. It is conceivable during the course of fitting to experimental data that too much weight was poured into the elastic constants at the expense of other MgO and CuO obsrvables.

Oxide	Ref.	C_{11}	C_{12}	C_{44}	C_{12}/C_{44}
MgO	[48]	296.03 ± 0.13	95.35 ± 0.13	155.89 ± 0.05	0.6116
CoO	[49]	255.6 ± 1.1	143.6 ± 1.5	80.5 ± 0.5	1.78
NiO	[49]	270 ± 13	125 ± 28	105 ± 21	1.24
	[50]	$344.6 \pm 1\%$	$40 \pm 10\%$	$141 \pm 5\%$	0.28

Table 3.1: Elastic constants of rocksalt binary oxides in HEO. All values are reported in units of GPa. The last column gives a sense of how far C_{12}, C_{44} deviate from the Cauchy relation.

3.4 Potential Fitting

Let $\mathcal{O}_{calc}$ denote an observable calculated by `GULP` in the course of a least-squares fit and $\mathcal{O}$ denote its value as determined by experiment. Then the 22 outstanding parameters $\{A, \rho, Y, K\}$ described in Sect. 3.1 are determined by minimizing the expression

$$\chi^2 = \sum_{\{\mathcal{O}\}} W(\mathcal{O}) \left[\mathcal{O} - \mathcal{O}_{calc}\right]^2 \tag{3.2}$$

where the sum is taken over all observables used in the fit and $W(\mathcal{O})$ is the weight accorded to observable $\mathcal{O}$. The fact that $W(\mathcal{O})$ is not unique implies an infinity of equally valid solutions (*i.e.* values of the undetermined parameters) to the least-squares problem. To select out one possible solution, the `GULP` manual proffers the following advice regarding a sensible choice of W:

1. It should be inversely proportional to $\mathcal{O}^2$. This ensures χ^2 is dimensionless and does not depend on the units in which $\mathcal{O}$ is measured.

2. It should be inversely proportional to the uncertainty in $\mathcal{O}$. Observables which are known more precisely are therefore assigned a larger weight.

These considerations motivated the following form of W:

$$W(\mathcal{O}) = \eta \times \frac{w(\mathcal{O})/N(\mathcal{O})}{w(\mathcal{O}_r)/N(\mathcal{O}_r)} \qquad w(\mathcal{O}) = \frac{1}{|\sigma_{\mathcal{O}}/\mathcal{O}|} \times \frac{1}{\mathcal{O}^2} \tag{3.3}$$

where η is a constant to be defined below, $\sigma_{\mathcal{O}}$ is the uncertainty in $\mathcal{O}$, $\mathcal{O}_r$ is a 'reference' observable (taken to be the lattice constant of MgO), and $N(\mathcal{O})$ counts the number of observables in the same class as $\mathcal{O}$. Thus if $\mathcal{O}$ is one of the 16 phonon frequencies used to fit the MgO parameters (see Appendix A), then $N(\mathcal{O}) = 16$. Four classes of observables were used in the fitting process:

structural data (*i.e.* cell lengths/angles and internal coordinates), static/high-frequency dielectric constants, and phonon frequencies.

The auxiliary function w accounts for the advice given in the `GULP` manual. Note that the relative uncertainty (and not *e.g.* the absolute uncertainty) appears in w to keep Eq. 3.2 dimensionless. In the function W, division by $w(\mathcal{O}_r)$ ensures all observables are weighted on the same scale when the binary oxides are merged to fit the oxygen shell model (see below). Division by the number of like observables $N(\mathcal{O})$ ensures all oxides are weighted similarly regardless of the relative abundances of experimental data. For instance, only 11 phonon frequencies were available to fit the CoO parameters, whereas 24 were used to fit the ZnO parameters (see Appendix A). The constant η simply controls the numerical size of χ^2 and was set to $\eta = 10^4$. This choice led to $\chi^2 \sim 10^2$.

Once the weight function has been specified, `GULP` minimizes χ^2 by adjusting the values of the outstanding fit parameters. The `relax` keyword was specified in the input files to force `GULP` to perform a structural relaxation after every fit iteration. This ensures the phonon frequencies are fitted at a minimum in the internal energy. Otherwise, they are ill-defined [51]. See Sect. 3.5 for more details on structural relaxation.

The manual cautions against allowing many parameters to vary simultaneously in a fit. To avoid this, the fit was performed in the following sequence of steps:

1. Optimize the cation-oxygen $\{A, \rho\}$ and the cation $\{Y, k\}$ for each oxide separately, leaving the O–O and the oxygen shell model parameters fixed at the Lewis & Catlow values.

2. Merge all oxides into a single file and optimize the oxygen shell model parameters, leaving all cation-oxygen and cation shell model parameters fixed at the values determined in step 1.

3. Fix the oxygen shell model parameters at the values determined in step 2 and re-optimise the cation-oxygen and cation shell model parameters.

4. Iterate steps 2 and 3 until no significant changes are observed in χ^2. Two iterations were deemed sufficient in the actual fit, each iteration after which χ^2 decreased by less than one part in 650.

The final values of the parameters are shown in Tables 3.2 and 3.3. Since all cations are equipped with a shell model, in contradistinction to Chen et al. [19], we refer below to the new potentials as the 'all-shell model', or ASM. Popov et al. have previously found reasonable agreement with the experimental phonon frequencies of CuO by using two Buckinhgam potentials to describe the inter/intraplanar Cu–O shell-shell interactions [52]. Their approach is adopted here.

As a test of the ASM, the calculated crystal structures, dielectric constants, and phonon frequencies of the binary oxides are compared to values from experiment and from Chen et al. in Appendix B. All MgO and CuO observables calculated from the ASM are in much better agreement with experiment as compared to those calculated using the Chen et al. potentials. Agreement between the experimental and ASM dielectric constants of Co–O, Ni–O, and Zn–O is also superior to the Lewis & Catlow potentials used by Chen et al. With the one exception of ZnO, the ASM generally provides better agreement with the experimental phonon frequencies.

3.5 Structural Relaxation

Let x be a vector in the space of the cell lengths, cell angles, and internal coordinates of a given material. In addition to the Buckingham and shell model parameters, the potential energy Eq. 2.6 is

	A (eV)	ρ (Å)	C (eV Å^6)	r_{min} (Å)	r_{max} (Å)
O – O	22,764	0.149	27.88	0	12
Mg – O	1266.7	0.301	0	0	8
Co – O	1244.3	0.305	0	0	8
Ni – O	1794.8	0.283	0	0	8
Cu – O	2054.7	0.269	0	0	2.3
	558.23	0.360	0	2.3	8
Zn – O	571.82	0.353	0	0	8

Table 3.2: Buckingham shell-shell cation-oxygen interactions in HEO.

	Y (e)	k (eV Å^{-2})
O	-2.88	70.52
Mg	2.77	137.3
Co	3.20	66.51
Ni	3.68	95.45
Cu	3.82	85.37
Zn	2.19	19.12

Table 3.3: Shell model parameters of the ions in HEO.

also an implicit function of x, since the force constants Eq. 2.4 are to be evaluated at the equilibrium configuration x_0.

For a simple, ordered solid such as MgO, x_0 can be straightforwardly inferred from *e.g.* x-ray diffraction measurements. For HEO, however, although there is long range crystalline order, atoms may be locally displaced from the ideal rocksalt positions due to differences in ionic radii. Hence it is not clear *a priori* exactly what x_0 is for a supercell of HEO. The problem is even worse in α-Si, where there is structural disorder.

Suppose the material in question is in a configuration x which is not too far from x_0; that is, x can be decomposed into $x = x_0 + \delta x$, where δx is small compared to x_0. Then the potential energy can be expanded in a Taylor series of δx as

$$\Phi(x) = \Phi(x_0) + \sum_i \left.\frac{\partial \Phi}{\partial x_i}\right|_0 (\delta x)_i + \frac{1}{2}\sum_{ij} \left.\frac{\partial^2 \Phi}{\partial x_i \partial x_j}\right|_0 (\delta x)_i (\delta x)_j + \dots$$

which can be expressed in vector form as

$$\Phi(x) = \Phi(x_0) + \boldsymbol{\nabla}\Phi \cdot \delta x + \frac{1}{2}(\delta x)^T H \delta x + \dots \tag{3.4}$$

where H is the Hessian matrix. In this work terms up to quadratic order in δx were retained in Eq. 3.4. This is known as the 'Newton-Raphson' procedure. By differentiating both sides of Eq. 3.4, the displacement δx from the current configuration x to the minimum x_0 is

$$\delta x = -H^{-1}\boldsymbol{\nabla}\Phi \tag{3.5}$$

Eq. 3.5 is exact for a harmonic energy surface; *i.e.* it is possible to go from x to x_0 in a single step. For a realistic energy surface, it must be applied iteratively.

A structural relaxation therefore consists of systematically varying δx to find a local minimum in $\Phi(x)$. Physically, the cell lengths, cell angles, and internal coordinates are adjusted until the lattice energy (forces) change by no more than 10^{-5} (10^{-3}) of the initial value after each iteration.

Inverting the Hessian in Eq. 3.4 is the most computationally expensive step in the structural relaxation. It is actually inefficient to recalculate H^{-1} after each iteration, since it often varies slowly. The Broyden-Fletcher-Goldfarb-Shanno (BFGS) algorithm was used to update the existing Hessian using the forces calculated in the previous iteration[1]. The updating formulae are shown explicitly on pg. 46 of the `GULP` manual [25].

3.6 Dielectric Function

The dielectric function is calculated within `GULP` as [25]

$$\varepsilon_{\alpha\beta}(\omega) = \varepsilon^{\infty}_{\alpha\beta} + \frac{4\pi}{V}\sum_s \frac{\Omega_{\alpha\beta}(s)}{\omega^2 - \omega_s^2 + i\omega\gamma} \tag{3.6}$$

where V is the volume of the unit cell, ω is the frequency of the applied field, ω_s is the frequency of the sth eigenmode, $\gamma = 4$ cm^{-1} is a mode-independent broadening factor chosen to match the

[1]The Newton-Raphson procedure, the tolerances in the discussion below Eq. 3.5, and the BFGS updating scheme are the default settings in `GULP`.

resolution of FTIR experiments [15], and $\Omega_{\alpha\beta}$ is the mode oscillator strength defined by

$$\Omega_{\alpha\beta}(s) = \left(\sum_b \frac{Q_{\alpha\gamma}(b)\, \varepsilon_\gamma(b;s)}{\sqrt{m_b}} \right) \left(\sum_b \frac{Q_{\beta\gamma}(b)\, \varepsilon_\gamma(b;s)}{\sqrt{m_b}} \right) \tag{3.7}$$

Note that Eq. 3.6 is just the Lorentz model for the dielectric function, with the $\{\Omega_{\alpha\beta}(s)\}$ playing the roles of plasma frequencies. The $\{Q_{\alpha\beta}(b)\}$ are elements of the Born effective-charge tensor

$$Q = Z - D_{cs} D_{ss}^{-1} Y \tag{3.8}$$

where the matrices on the right-hand side have been defined in Sects. 2.1.4 and 2.1.5. Physically, Q *defines* the effective charges of the ions in the system by considering the change in the total dipole moment μ with respect to atomic perturbations [25]. Since μ is a quantum-mechanical observable, the Born effective charges can be calculated *ab initio* from density functional theory.

3.7 Supercell Generation

Atom probe tomography experiments on HEO reveal no short-range cation ordering down to an atomic resolution of 1–3 Å [53]. To this end, supercells of HEO were generated by randomly distributing equiatomic ratios of Mg, Co, Ni, Cu, and Zn throughout the cation sublattice.

Results are also shown (in Sects. 4.2.1 and 4.3.1) for a single, 4096-atom supercell of 'high-entropy sulfide-oxide' (HESO), which was generated by randomly doping half of the oxygen sublattice in HEO with sulfur ions. The cation-sulfur potentials are identical to the cation-oxygen Buckingham potentials, and the sulfur-sulfur and sulfur-oxygen potentials are identical to the oxygen-oxygen potential. The sulfur and oxygen shell models are also identical. Thus HESO adds only mass disorder, and not force constant disorder, to HEO. The purpose of simulating HESO is to investigate the importance of additional mass disorder on the creation of localized vibrational modes. It must be noted that HESO has not been observed experimentally, although high-entropy oxyflorides crystallizing in the rocksalt structure were recently synthesized in 2020 [54].

For the sake of comparison, results are also presented for a single, 1000-atom supercell of α-Si. The cell lengths, cell angles, internal coordinates, and interatomic potentials were adapted from Barkema et al. [55].

Chapter 4

Results

4.1 Model Validation

In this section, the simulated lattice parameters, bond lengths, and optical conductivity of HEO are compared to experiment. All `GULP` results have been averaged over 50 disorder realizations. Each realization was structurally relaxed (see Sect. 3.5) before any properties were calculated.

Frequent comparison is made to the paper by Anand et al. [18], who have previously applied classical lattice dynamics to HEO in order to study its thermodynamics. Details regarding the interatomic potentials employed by Anand et al. were discussed in Sect. 3.3.

4.1.1 Lattice Parameters

The lattice parameters of HEO are shown in Table 4.1. The cell angles are all correctly equal to 90° within error. The cell lengths are in pairwise agreement but slightly underestimate the value from x-ray diffraction (XRD) measurements by 0.03 Å $\sim 1\%$. By averaging over $\mathcal{O}(10^4)$ disorder realizations of 2000-atom supercells, Anand et al. [18] report an average cation-oxygen distance of 2.08 Å, corresponding to an even shorter cell length of 4.16 Å.

	XRD [15]	Anand et al. [18]	This work
α (°)	90	–	90.000(3)
β (°)	90	–	90.000(2)
γ (°)	90	–	90.000(2)
a (Å)	4.236(1)	4.16	4.2058(8)
b (Å)	4.236(1)	4.16	4.2058(8)
c (Å)	4.236(1)	4.16	4.2058(8)

Table 4.1: Optimised lattice parameters of HEO. Anand et al. do not report error estimates.

4.1.2 Bond Lengths

The distributions of first nearest-neighbour cation-oxygen distances ('bond lengths') in HEO are shown in Fig. 4.1. All distributions are composed of a main peak and a shoulder in the right tail. Anand et al. [18] have reported a bimodal distribution of Cu–O bonds and concluded that the experimentally-observed local lattice distortion in the vicinity of Cu cations may be due to a combination of the Jahn-Teller effect [13] and differences in ionic radii. They do not mention whether or not the other cation-oxygen bonds are similarly distributed. The median bond lengths are listed explicitly in Table 4.2 and are compared to results from extended x-ray absorption fine-structure spectroscopy (EXAFS). Our results agree with the experiment of Sushil et al. [56].

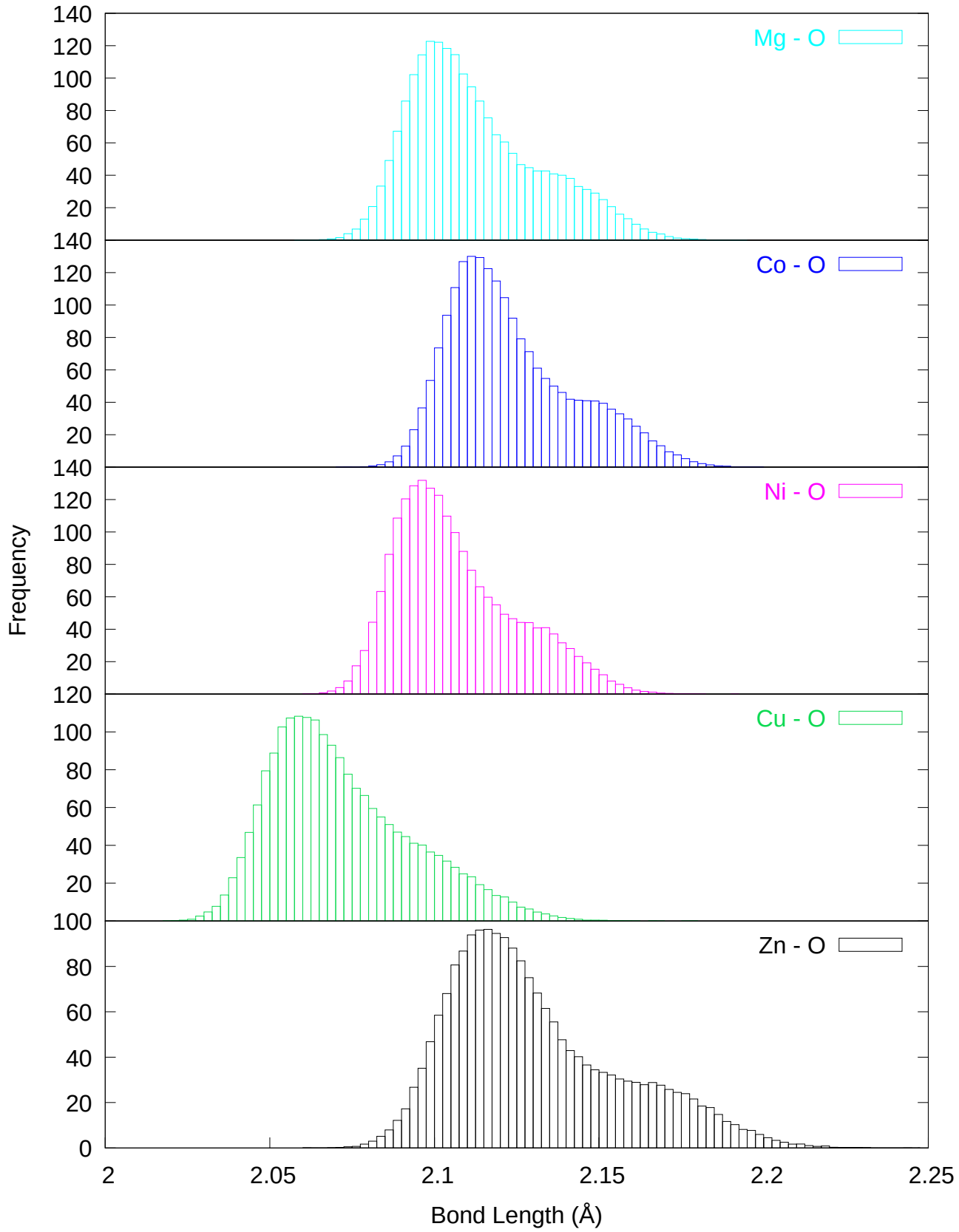

Figure 4.1: Distribution of first nearest-neighbour cation-oxygen distances (bond lengths) in HEO.

	Rost et al. [57]	Sushil et al. [56]	Anand et al. [18]	This work
Mg–O	–	–	2.088(3)	2.10(2)
Co–O	2.089(9)	2.0906	2.093(3)	2.11(2)
Ni–O	2.084(5)	2.0918	2.080(3)	2.10(2)
Cu–O	2.07(5)	2.0733	2.033(3)	2.06(2)
Zn–O	2.078(9)	2.0984	2.094(3)	2.12(3)

Table 4.2: Bond lengths in HEO. Rost et al. and Sushil et al. are EXAFS studies. Mg–O bonds were not analysed to due to insufficient energy resolution. Sushil et al. do not report error estimates. Errors in the results from Anand et al. are taken to be equal to the width of the data points in their Fig. 4b).

4.1.3 Internal Coordinates

It should be verified that the internal atomic coordinates do not drift too far from the ideal rocksalt positions in the course of a structural relaxation. Otherwise, `GULP` may be incorrectly signalling that HEO is not stable in the rocksalt structure.

Let b, b' denote the equilibrium position vectors (in fractional coordinates) of the bth atom in the supercell before and after structural relaxation, respectively. The 'drift' vector $\Delta_\alpha(b, b')$ which respects periodic boundary conditions is then given by

$$\Delta_\alpha(b, b') = (b_\alpha - b'_\alpha) - \text{floor}\,(b_\alpha - b'_\alpha) \tag{4.1}$$

The distribution of 'atomic drifts', *i.e.* the norms of the $\{\Delta_\alpha(b, b')\}$, is presented in Fig. 4.2. Each ion drifts ~ 0.05 Å relative to the ideal rocksalt structure, which is indeed much smaller than the cation-oxygen spacings of ~ 2.1 Å in Table 4.2. It is not clear if the secondary features near 0.01 Å have a physical origin or are artifacts of the structural relaxation.

4.1.4 Optical Conductivity

As discussed in Sect. 1.1.2, the real part of the optical conductivity $\sigma'(\omega)$ of HEO has previously been extracted from FTIR reflectance data via Kramers-Kronig analysis [15] and is shown in Fig. 4.3. Due to the small triclinic distortions in Table 4.1, `GULP` predicts that the dielectric tensor $\sigma'_{\alpha\beta}(\omega)$ has nonzero off-diagonal components. However, the smallness of the distortions implies a corresponding smallness in the off-diagonal components at most frequencies. To make a comparison to experiment, the average of the diagonal components; *i.e.* the average of the trace

$$\sigma'(\omega) \approx \frac{\sigma'_{11}(\omega) + \sigma'_{22}(\omega) + \sigma'_{33}(\omega)}{3}$$

is plotted in Fig. 4.3. It may be seen that the `GULP` model reproduces the weak mode in the experimental optical conductivity. The agreement between the main peaks near 360 cm^{-1} is also satisfactory. The asymmetry in the `GULP` peak may a result of the Zn–O Buckingham and shell model parameters underestimating the phonon frequencies in ZnO by $\pm 20\%$. See also Appendix B.

That the ZnO phonon frequencies are underestimated suggests the ZnO potential is too 'soft'. To test this, a second ZnO potential was developed in which Zn and oxygen still interact through

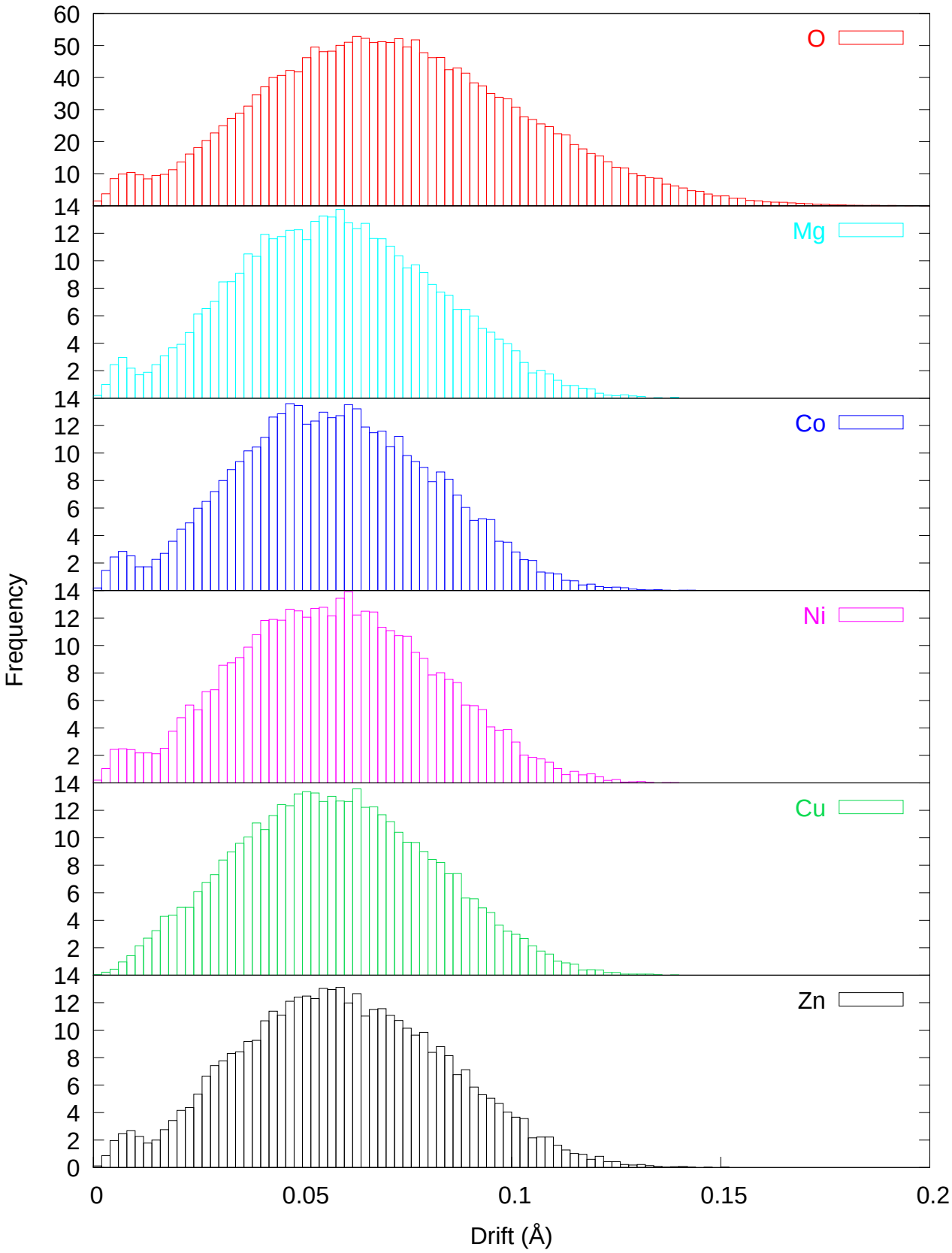

Figure 4.2: Distribution of atomic deviations from ideal rocksalt positions (drifts) in HEO.

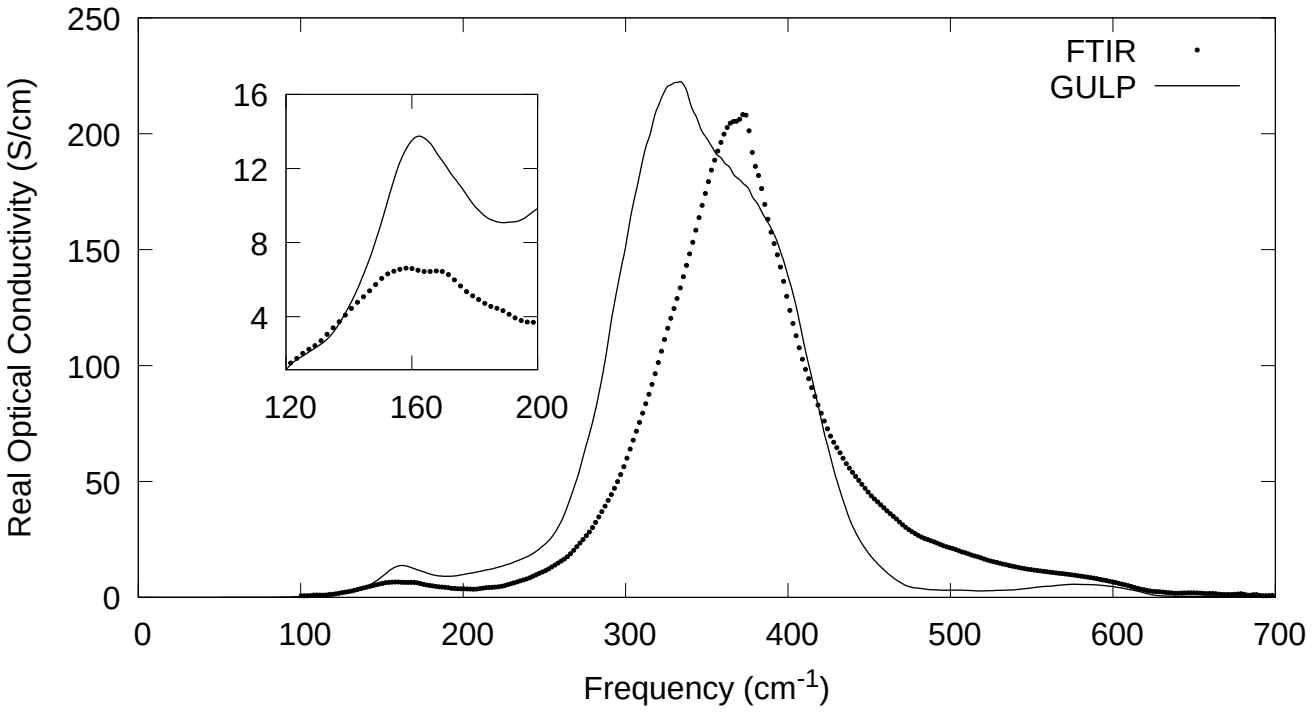

Figure 4.3: Simulated optical conductivity of HEO. FTIR results at 5 K adapted from [15].

the Buckingham potential, but a harmonic spring was added between nearest-neighbour Zn and oxygen ions to stiffen the potential. In doing so the asymmetry was eliminated and the strong mode frequencies agreed within error. However, the weak mode frequency was overestimated by 50 cm^{-1}. It was decided not to proceed with the modified set of potentials on the grounds that: a) the existence of localized vibrational modes was independent of the potentials used, and; b) qualitative agreement between the simulated and experimental optical conductivity was achieved without the addition of the harmonic spring.

4.1.5 Elastic Constants

The `GULP` manual recommends testing new potentials against observables not used in the fitting process. Calculated observables which are unphysical likely indicate an error in the potentials [25].

The elastic constants of HEO have previously been calculated by Pitike et al. from density functional theory (DFT) [58] and are compared to the `GULP` calculations in Table 4.3. As discussed in Sect. 3.3, central potentials cannot correctly describe solids (such as HEO and its parent binary oxides) which violate the Cauchy relation $C_{12} = C_{44}$ between elastic constants. Nonetheless, the `GULP` model does predict $C_{11} \sim 2C_{12}$, which agrees roughly with the DFT result, and satisfies the following conditions for mechanical stability in a cubic crystal [58]

$$C_{44} > 0; \qquad C_{11} > |C_{12}|; \qquad C_{11} + 2C_{12} > 0$$

	C_{11}	C_{12}	C_{44}
GULP	354.3(3)	168.37(9)	167.31(3)
DFT	303	124	88

Table 4.3: Elastic constants of HEO from GULP compared to DFT. All values are in units of GPa. No error estimates are reported in [58].

4.2 Characterization of Vibrational Modes

In this section the nature of the vibrational modes in HEO is examined. All phonon calculations in Sects. 4.2 and 4.3 have been performed at $q = 0$ only.

4.2.1 Engagement

Let B denote one of the six ionic species in HEO. Then the 'engagement' of species B in the eigenmode s is defined by

$$E(B;s) = \sum_{b\in B}\sum_{\alpha} |\varepsilon_\alpha(b;s)|^2 \tag{4.2}$$

where $\sum_{b\in B}$ is taken over all atoms in the supercell belonging to the species B, and $\sum_\alpha$ is taken over all Cartesian directions. The quantity defined by Eq. 4.2 does not appear to have a standardized name in the context of vibrational mode localization; it is referred to by Carvalho et al. [59] as the 'relative amplitude' and by Thienprasert et al. [60] as the 'localization' itself. The name 'engagement' is preferred here, as $E(B;\omega_s) \sim 1$ if species B is strongly 'engaged' in the motion at eigenfrequency ω_s and $E(B;\omega_s) \ll 1$ otherwise. It follows from the orthonormality Eq. 2.14 of the phonon eigenvectors that

$$\sum_B E(B;s) = \sum_b\sum_\alpha |\varepsilon_\alpha(b;s)|^2 = 1$$

and thus the engagement is only useful for crystal structures with multiple atomic species per unit cell; otherwise, it is trivially equal to one for all frequencies. The engagements of the ions in a 4096-atom configuration of HEO are shown in Fig. 4.4. Each dot represents a single eigenmode. At low frequency the engagements of the cations are high, while as frequency increases the cation engagements fall and the oxygen engagement rises to a value near unity. This agrees with the intuition that $\omega^2 \sim k/m$; at low frequency the heavier cations vibrate most intensely, and conversely for oxygen at high frequency. See Table 1.1 for a list of the atomic masses. A transition from cation- to oxygen-dominated motion occurs near 300 cm^{-1}, where the engagement curves cross.

At 150 cm^{-1} the Zn and oxygen engagements simultaneously obtain a global maximum and minimum, respectively. This suggests that the corresponding peak in the optical conductivity (see Fig. 4.3) is driven by the motion of Zn ions against a stationary oxygen sublattice. This is further supported by Lorentz oscillator fits to FTIR reflectance data, which show that the plasma frequency of the 150 cm^{-1} mode is smallest when Zn (and not Mg, Co, or Cu) is removed from HEO [15].

While the engagement might explain the origin of the 150 cm^{-1} mode, it does not explain the role played by disorder. In pure ZnO there is also a crossover in the engagement between cation- and oxygen-dominated motion, yet no weak mode appears in its optical conductivity. From the fact that the GULP model senses the weak mode at all, it follows that the mode does not originate from anharmonic effects (since GULP operates under the harmonic approximation) or cation-cation interactions (which were excluded from the model; see the assumptions in Sect. 3.1).

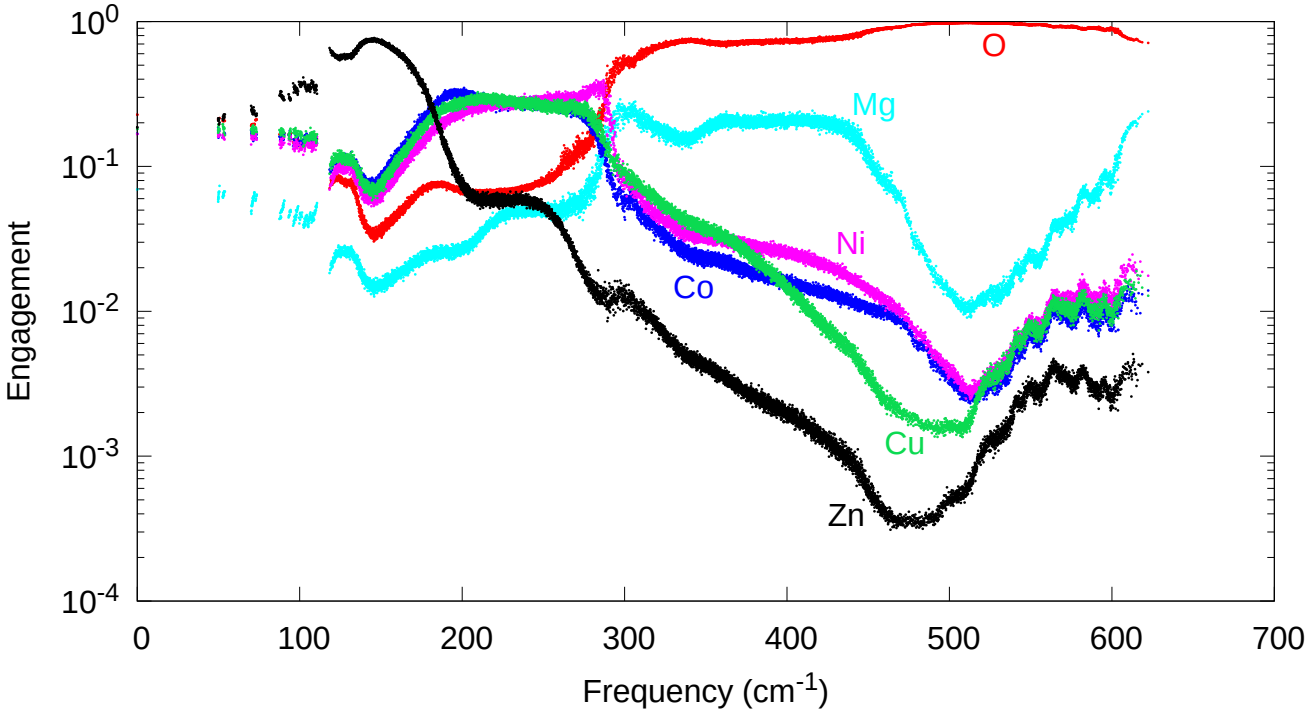

Figure 4.4: Engagements of ions in a 4096-atom configuration of HEO.

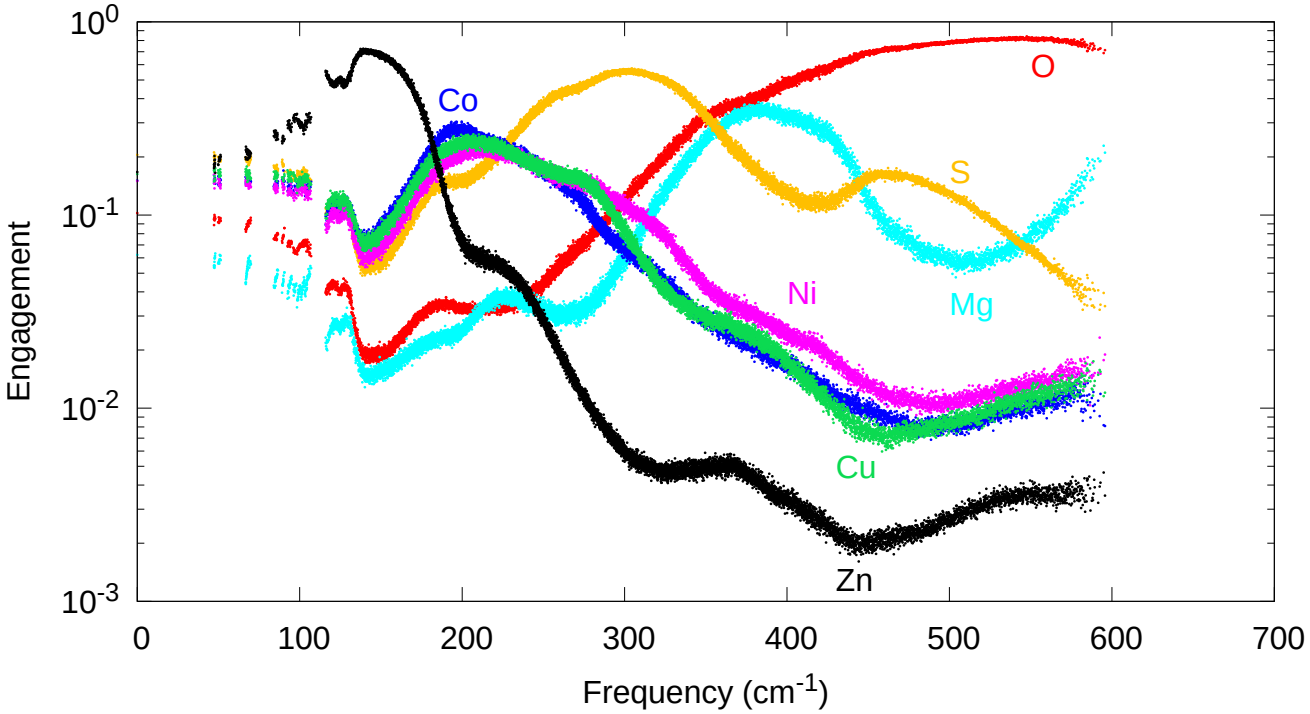

Figure 4.5: Engagements of ions in a 4096-atom configuration of HESO.

One may wonder if the mode is driven by short-range correlations. Denote by $(\mathrm{Zn})_{max}$ the Zn ion with the largest eigenvector component at a given frequency. The distribution of second and fourth nearest-neighbour cations (abbreviated '2NN' and '4NN', respectively) surrounding $(\mathrm{Zn})_{max}$ is shown in Fig. 4.6. The histogram has been averaged over fifty 4096-atom disorder realizations. For each realization, an additional average has been performed over 100 eigenmodes with frequencies closest to the 150 cm^{-1} peak in the Zn engagement. There is no strong preference for any one species of cation as a second or fourth nearest-neighbour. Fig. 4.7 compares the distributions of nearest-neighbour Zn–O bond lengths surrounding $(\mathrm{Zn})_{max}$ to the bulk distribution of Zn–O bond lengths from Fig. 4.1. The same averaging procedure just described was also used to generate the '1NN' curve in Fig. 4.7. There is a slight shift in weight towards shorter Zn–O bond lengths about $(\mathrm{Zn})_{max}$, but the peaks of the two distributions agree within error [2.12(3) Å for bulk ZnO from Table 4.2; the same results for $(\mathrm{Zn})_{max}$]. It is therefore unlikely that the weak mode in the optical conductivity is caused by short-range order.

It is worthwhile noting that the weak mode also appears in the ternary series $\mathrm{Co}_{1-x}\mathrm{Zn}_x\mathrm{O}$, as shown in Fig. 4.8. Observe that as x decreases, the strong Zn peak appears to split into two low-intensity peaks near 150 cm^{-1} and 250 cm^{-1}. It is conceivable that a similar splitting of the Zn peak in HEO leads to the weak mode in the optical conductivity. The nature of the mechanism which causes the splitting, however, remains unclear. No experimental reports on rocksalt $\mathrm{Co}_{1-x}\mathrm{Zn}_x\mathrm{O}$ were found in the literature.

Finally, the engagements of HESO are shown in Figs. 4.5. These will be discussed in Sect. 4.3.1, in connection with the participation ratio. See Sect. 3.7 for the definition of HESO.

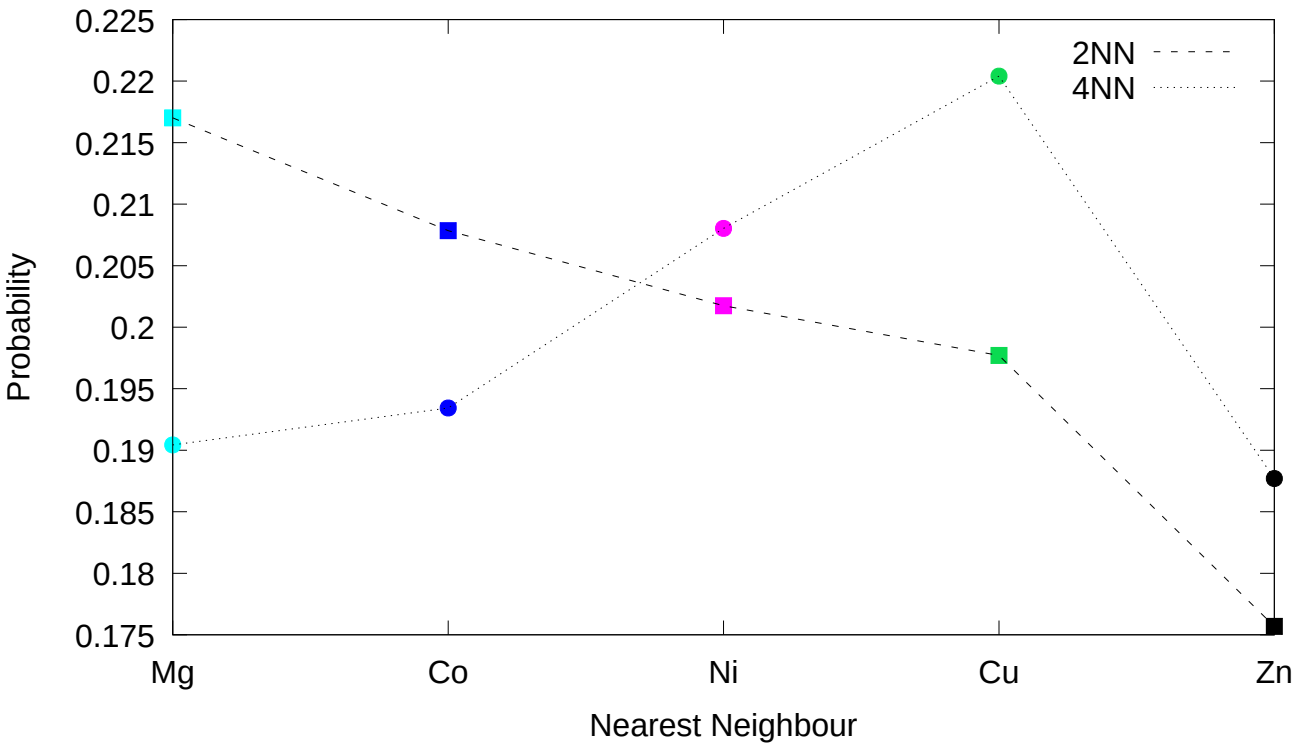

Figure 4.6: Distribution of second and fourth nearest-neighbour cations ('2NN' and '4NN', respectively) surrounding the Zn ion with the largest eigenvector component near 150 cm^{-1}.

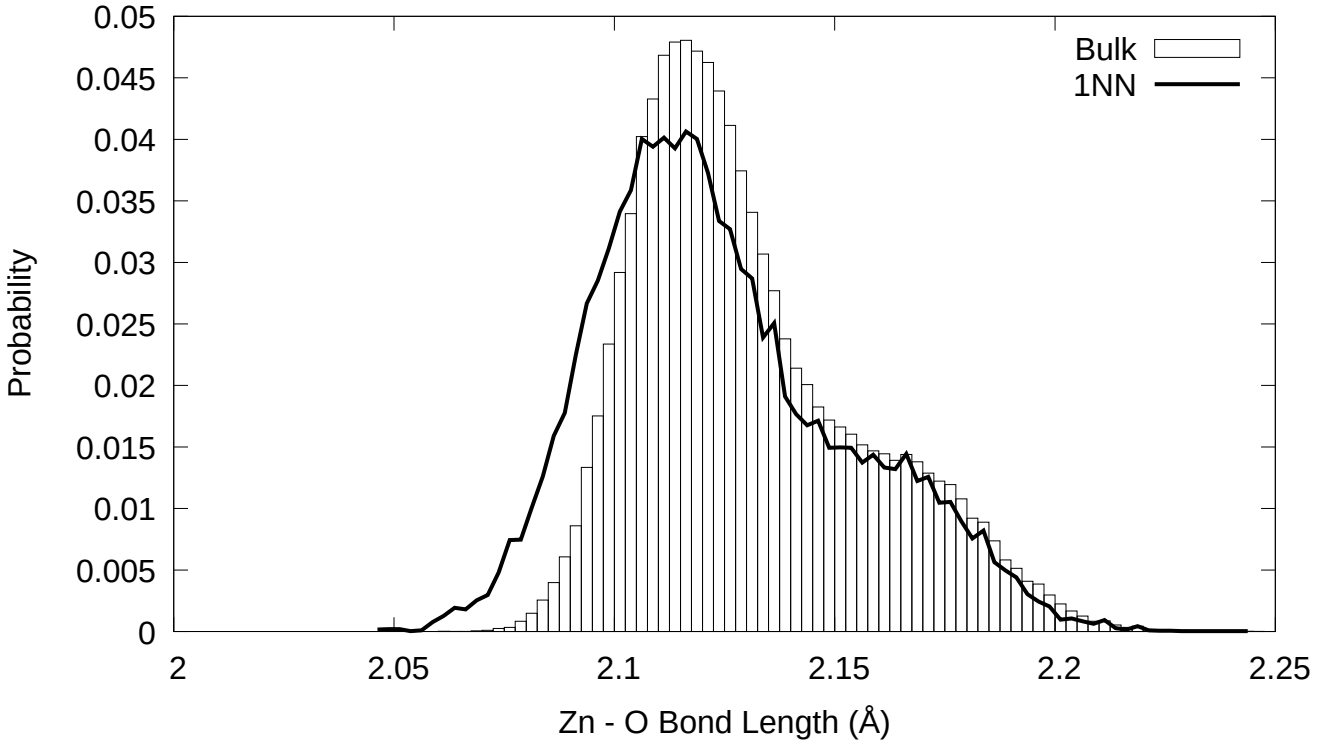

Figure 4.7: Distribution of nearest-neighbour Zn–O bond lengths originating from the Zn ion with the largest eigenvector component near 150 cm^{-1}.

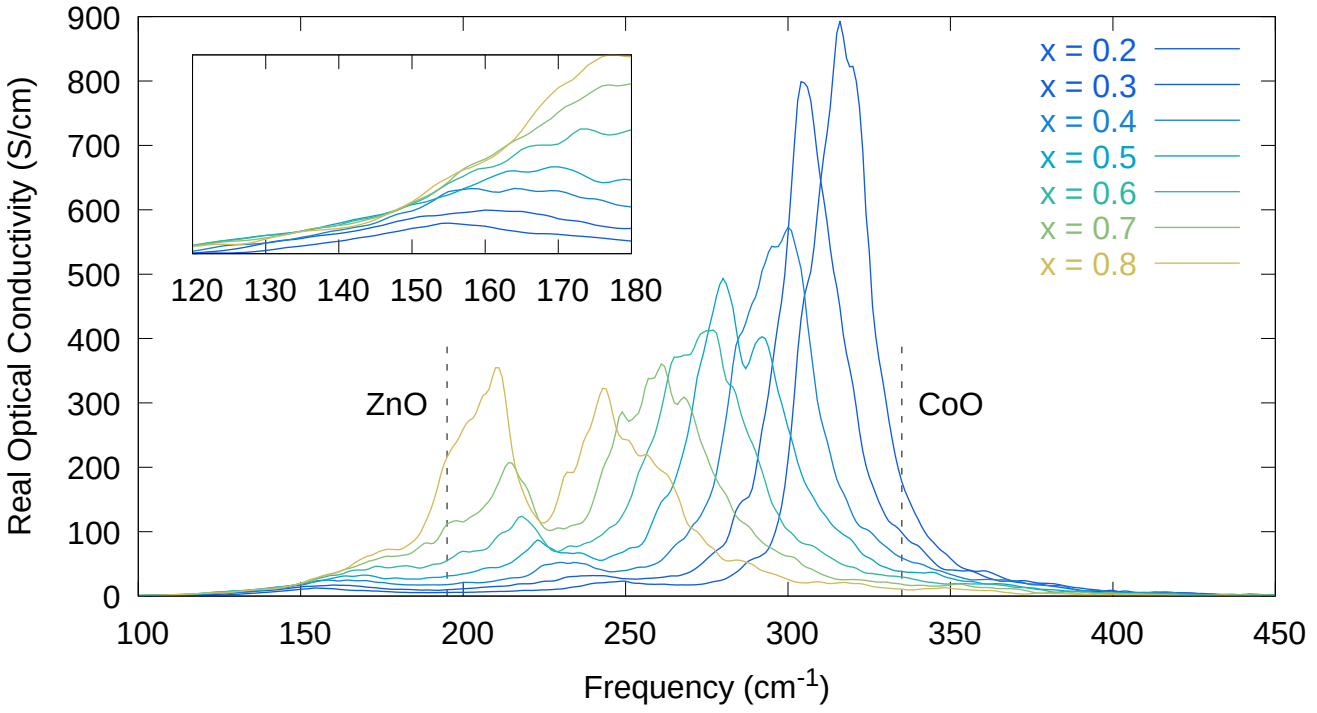

Figure 4.8: Simulated optical conductivity of the ternary series $Co_{1-x}Zn_xO$. The dotted lines indicate the positions of the TO peaks in pure CoO and ZnO.

4.2.2 Phase Quotient

The phase quotient introduced by Bell and Hibbins-Butler [35] is defined by

$$\phi_s = \frac{\sum_{\langle bb' \rangle} \sum_\alpha \varepsilon_\alpha(b;s)\,\varepsilon_\alpha(b';s)}{\sum_{\langle bb' \rangle} \left|\sum_\alpha \varepsilon_\alpha(b;s)\,\varepsilon_\alpha(b';s)\right|} \tag{4.3}$$

where $\sum_{\langle bb' \rangle}$ denotes a double summation over all atoms b and over all nearest-neighbours $\{b'\}$ of b. Eq. 4.3 generalizes acoustic and optical phonons to disordered media: when nearest-neighbours vibrate in-phase, $\phi_s = 1$; conversely, when nearest-neighbour vibrations are out-of-phase, $\phi_s = -1$.

The phase quotient of a 4096-atom configuration of HEO is shown by the series marked '1NN' (shorthand for 'first nearest-neighbour') in Fig. 4.9. As in crystalline solids, the vibrations near zero frequency are all acoustic; as frequency increases, the vibrations change character to optical-like modes. Near the 150 cm^{-1} weak mode in the optical conductivity, the vibrations are strongly acoustic. Hence the engagement curves in Fig. 4.4 reveal that Zn dominates the motion at 150 cm^{-1}, while the phase quotient reveals that Zn and oxygen vibrate in-phase. It is also interesting to note that the phase quotient peaks to zero near 500 cm^{-1}, just as the oxygen (cationic) engagement attains a maximum (minimum) in Fig. 4.4. Vibrations at this frequency are 'halfway' between acoustic and optical modes, since only the oxygen sublattice vibrates.

Fig. 4.9 also presents modified phase quotients with the summation taken over nearest-neighbours in the cation and oxygen sublattices separately. No vibrational coherence is maintained throughout the oxygen sublattice at any frequency.

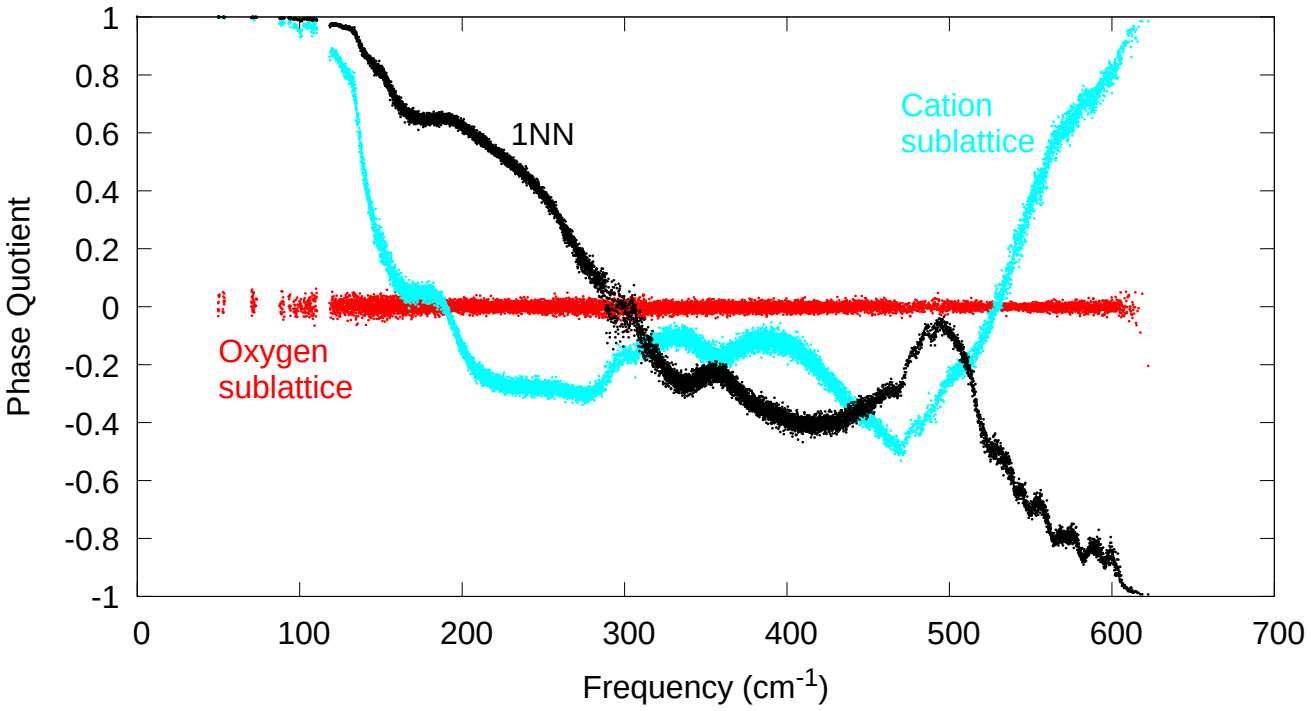

Figure 4.9: Phase quotient of a 4096-atom configuration of HEO.

4.2.3 Polarizations

In Table 2.1 it was noted that the vibrational eigenvectors of a propagon are spatially coherent while the eigenvectors of a diffuson or locon are randomly-oriented. This was observed by Allen et al. [37] in α-Si and should be verified for HEO. Following Yao et al. [61], the eigenvectors are projected onto the unit sphere according to

$$\varepsilon_\alpha(b;s) \to \frac{\varepsilon_\alpha(b;s)}{\sum_\alpha \varepsilon_\alpha(b;s)\,\varepsilon_\alpha(b;s)} \tag{4.4}$$

The polarizations of select modes in a 4096-atom configuration of HEO are shown in Fig. 4.10. Each of the 4096 dots represents the arrowhead of a vector indicating the direction a given atom is oscillating in the mode. The 0 cm^{-1} mode (upper left) is one of the three Goldstone modes in HEO; *i.e.* a mode in which the supercell is rigidly translated at zero energy cost. Observe that there is a single dot corresponding to the singular direction in which all atoms are oscillating. The 50 cm^{-1} mode (upper right) is the tenth-lowest frequency mode in HEO. The dots sweep out a larger solid angle compared to the Goldstone mode, but they are not randomly-distributed over the surface of the unit sphere. Thus the 50 cm^{-1} modes is believed to be a propagon. The remaining modes in Fig. 4.10 occur at higher frequencies and appear to exhibit a random distribution of dots. This suggests that these modes are either diffusons or locons.

The polarizations of atoms in the $z = 1/2$ plane (fractional coordinates) can be seen explicitly in Fig. 4.11. The z-components of the oscillations are not shown for ease of visualization. As expected, all atoms vibrate in the same direction in the Goldstone mode. No spatial coherence is apparent in the diffuson or locon modes. Vortex-like structures appear in the polarization of the propagon mode. Intuitively, these are slowly spatially-varying deformations of the Goldstone mode, and thus occur at lower energies than the diffuson or locon modes.

4.3 Localized Vibrational Modes

In this section several diagnostics for vibrational mode localization are extracted the eigenfrequencies and eigenvectors.

4.3.1 Participation Ratio

The participation ratio P defined by

$$P(s) = \frac{1}{N} \times \frac{\left[\sum_b \sum_\alpha |\varepsilon_\alpha(b;s)|^2\right]^2}{\sum_b \left[\sum_\alpha |\varepsilon_\alpha(b;s)|^2\right]^2} \tag{4.5}$$

where N is the number of atoms in the supercell, is an order parameter for Anderson localization in disordered systems. To see this, suppose that in a particular vibrational mode only a single atom b' is oscillating. Then $\sum_\alpha |\varepsilon_\alpha(b;s)|^2 = \delta_{bb'}$ and $P = N^{-1}$. Conversely, suppose that in another mode every atom vibrates with roughly the same intensity, so that the vibration is extended over the supercell; *i.e.* $\sum_\alpha |\varepsilon_\alpha(b;s)|^2 \sim \text{const.} \equiv \varepsilon_0^2$. In this case

$$P(s) \sim \frac{1}{N} \times \frac{\left[\sum_b \varepsilon_0^2\right]^2}{\sum_b \varepsilon_0^4} = \frac{1}{N} \times \frac{N^2\varepsilon_0^4}{N\varepsilon_0^4} = 1$$

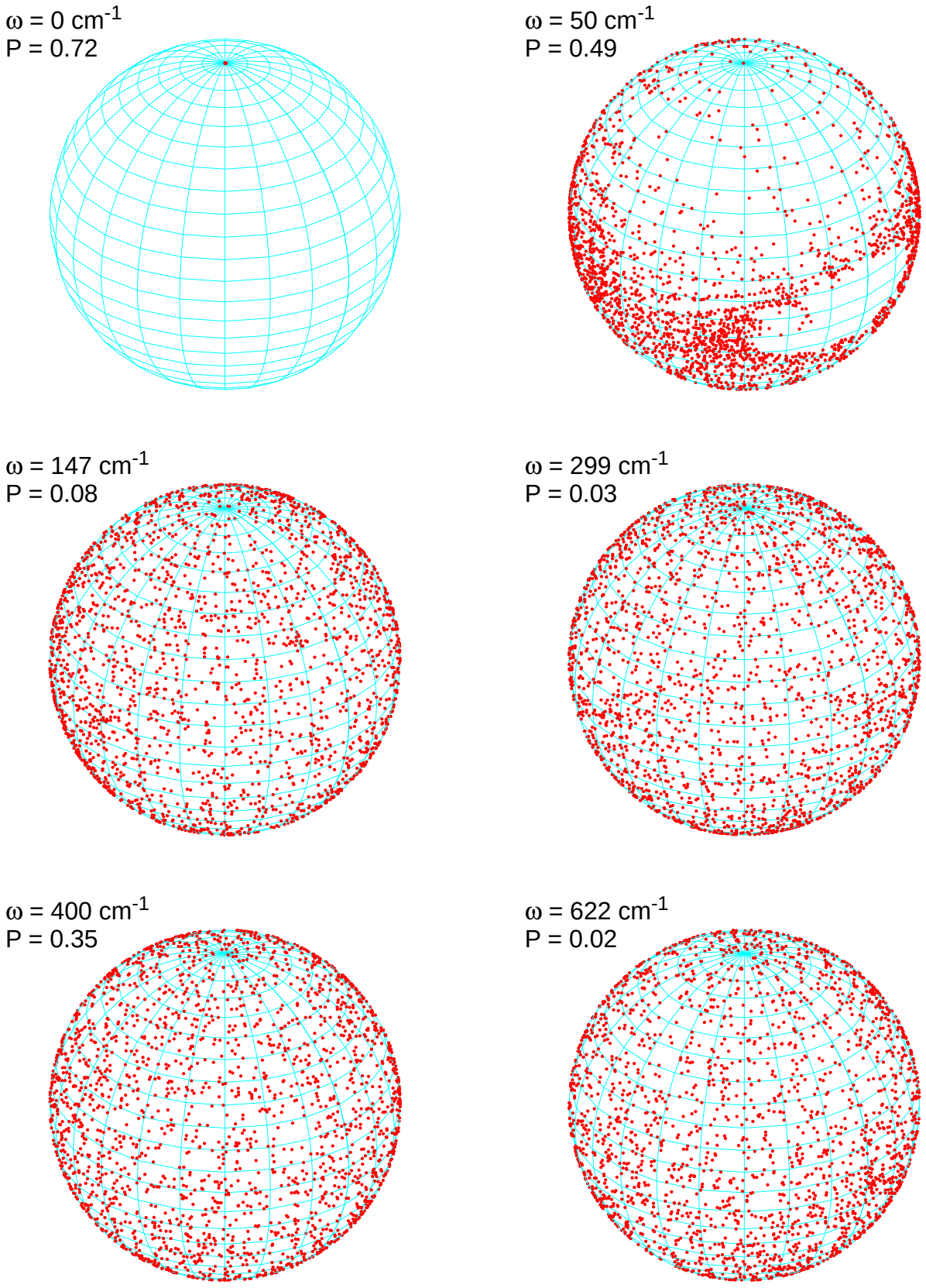

Figure 4.10: Polarizations of select eigenmodes in a 4096-atom configuration of HEO. The frequencies and participation ratios (see Sect. 4.3.1) of the modes are listed in the upper-left corners.

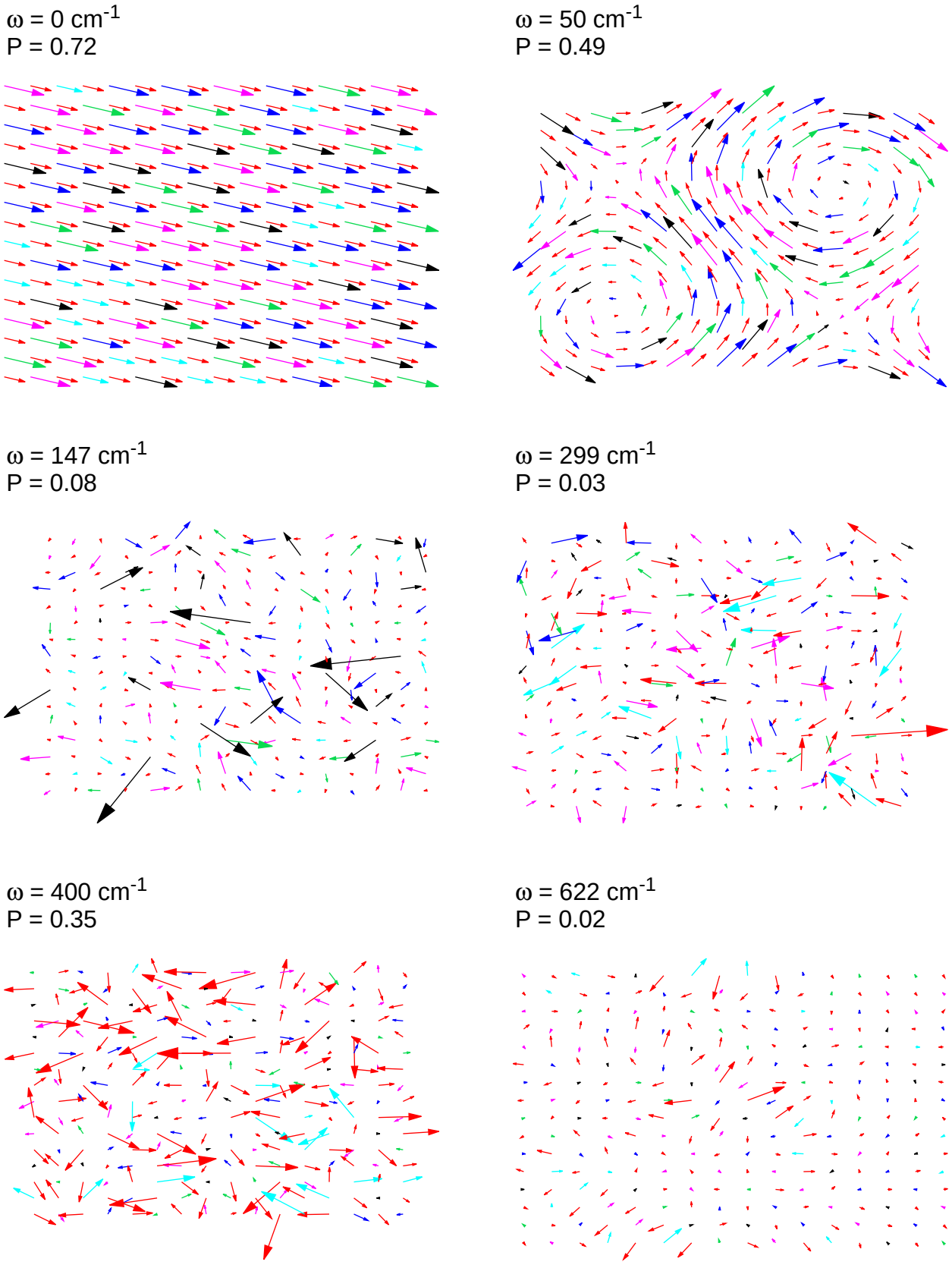

Figure 4.11: Polarizations in the $z^1/_2$ plane (fractional coordinates) of select eigenmodes in a 4096-atom configuration of HEO. The frequencies and participation ratios (see Sect. 4.3.1) are listed in the upper-left corners. Refer to Fig. 1.1 for the colour scheme.

Thus the numerical size of P can be used to distinguish between extended and localized modes. In practise, participation ratios of the order N^{-1} likely do not occur and previous studies have chosen *e.g.* $P < 0.1$ or $P < 0.2$ as the cutoff for localized modes [62]. A cutoff of $P < 0.05$ is used throughout the remainder of this thesis[1].

Fig. 4.12 compares the participation ratios of HEO, HESO, and α-Si. See Sect. 3.7 for the definition of HESO. Each system exhibits a high-frequency 'mobility edge' separating the localized from the extended modes. At frequencies beyond the mobility edge, the participation ratio falls rapidly towards zero. The highest-frequency mobility edge occurs in HEO, where the average atomic mass is lightest.

Consider the cluster of modes near 300 cm^{-1} in HEO below the locon cutoff of $P < 0.05$. Given that these modes occur at the same frequency as the engagement curve crossings in Fig. 4.4, it is reasonable to conclude that they originate from a transition from cation- to-oxygen dominated motion. Further support for this idea follows by noticing that the engagement of sulfur ions in HESO (see Fig. 4.5) reaches a maximum at 300 cm^{-1}. Hence the motion of sulfur ions interpolates between the low- and high-frequency regimes of cation- and oxygen-dominated motion, and there is no well-defined transition from one regime to the other. Consequently, there is no 300 cm^{-1} minimum in the participation ratio of HESO.

At this stage, it must be remarked that a transition from cation- to oxygen-dominated motion is not sufficient to guarantee the existence of localized modes. Rather, the results of the following sections all indicate that the modes near 300 cm^{-1} in HEO are diffusons despite satisfying $P < 0.05$. This makes clear the arbitrariness in the locon cutoff and suggests that no one test for localization is definitive evidence for localized modes.

The preceding discussion also makes clear that, if it is desired to engineer a high-entropy material containing a significant fraction of localized modes, it is not enough to combine masses at random. The legend entries in Fig. 4.12 count the fraction of modes which fall below the threshold of $P < 0.05$. That this number is identical in HEO and HESO implies that HESO 'transfers' the 300 cm^{-1} cluster of modes in HEO to higher frequencies, beyond its mobility edge. Both HEO and HESO support an order-of-magnitude fewer locons than α-Si, which suggests that structural disorder favours the creation of localized modes more strongly than mass- or force constant-disorder.

The dip in the participation ratio of α-Si at 250 cm^{-1} has a very different origin and was proposed by Allen et al. [37] to arise, in analogy with crystalline silicon, from a transition from TA-like modes to LA-like modes. See also Fig. 2.3 and the discussion in Sect. 2.2.2.

4.3.2 Bubble Plots

In Fig. 4.13 each atom b in a 4096-atom configuration of HEO is represented by a sphere with diameter proportional to $\sum_\alpha |\varepsilon_\alpha(b;s)|^2$; *i.e.* the norm of the bth eigenvector component in mode s. Thus a larger sphere indicates an atom which is vibrating more intensely, and vice-versa. For ease of visualization, periodic boundary conditions have been invoked to shift the atom with the largest eigenvector norm to the centre of the supercell. In addition, all atoms are located at the ideal rocksalt positions[2]. It is clear that the 200 cm^{-1} mode is delocalized. This agrees with the prediction of the participation ratio, since $P = 0.250$ is well above the locon cutoff of 0.05. The

[1] The location of cutoff is arbitrary. The choice $P < 0.05$ was partly made to exclude the modes near the 150 cm^{-1} minimum in the participation ratio (Fig. 4.12), which would be locons according to $P < 0.1$ but are actually diffusons according to the results of subsequent sections.

[2] This does not significantly affect the visualization of the modes – from Fig. 4.2, the ions drift only ~ 0.05 Å from the ideal rocksalt lattice, or $\sim 2\%$ of the cation-oxygen spacings.

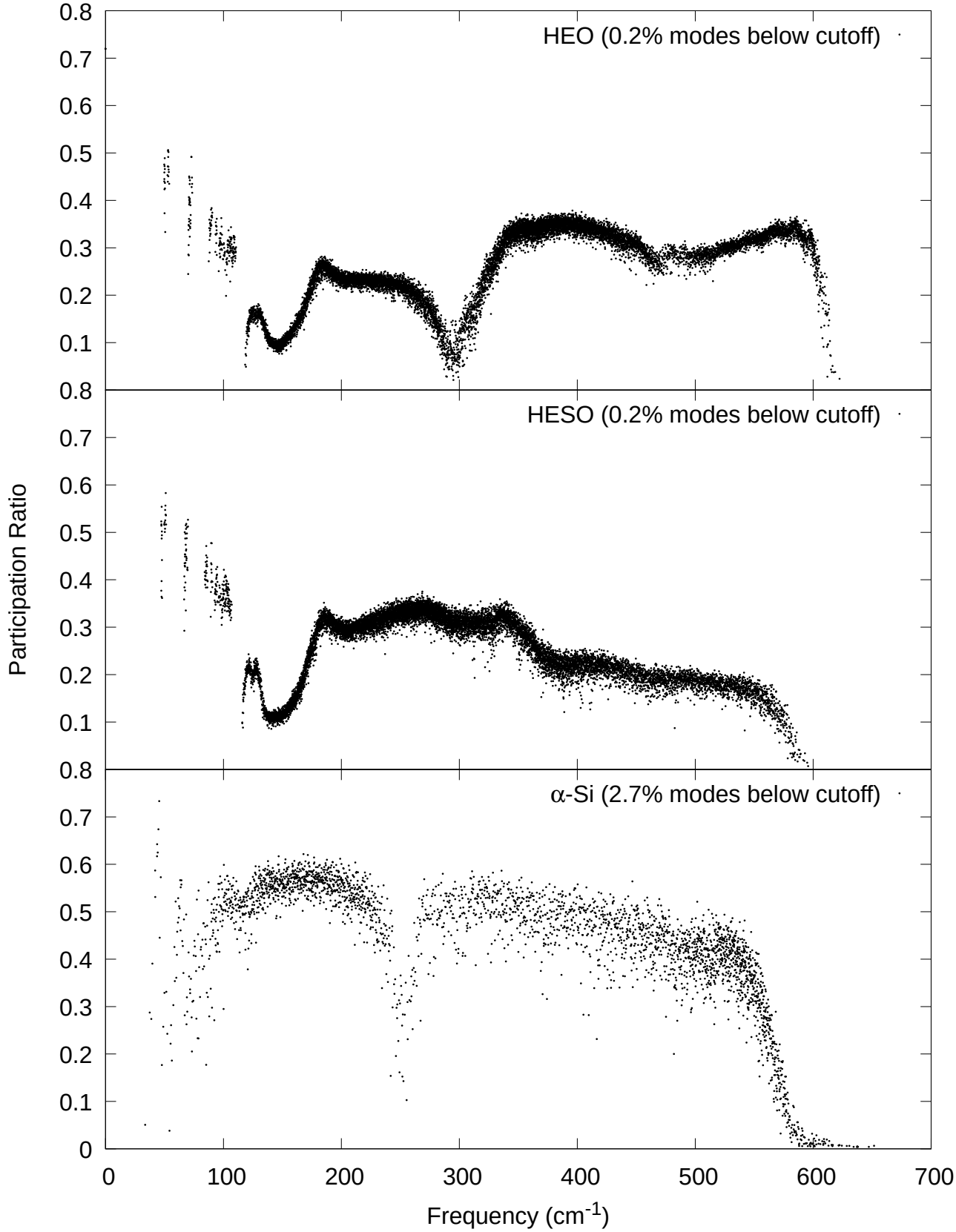

Figure 4.12: Participation ratios of 4096-atom configurations of HEO and HESO, and a 1000-atom configuration of α-Si. The legend entries count the fraction of modes in each system falling below the locon threshold of $P < 0.05$.

same is true of the 150 cm^{-1} mode; however, it should be noted that this would be considered a locon on the basis of $P < 0.1$, as is common in the literature [62].

4.3.3 Localization Lengths

Allen et al. [37] observed that the eigenvector components of locons α-Si decay exponentially as

$$|\varepsilon(b;s)| \propto \exp\left(-\frac{|b - b_{max}|}{\xi_s}\right) \tag{4.6}$$

where b is any atom in the supercell, b_{max} is the atom with the largest eigenvector component, and ξ_s is the localization length of mode s, which should be much smaller than the lattice constant of the supercell $a \sim 33$ Å.

Visual inspection of Fig. 4.13 suggests that modes near 300 cm^{-1} and 620 cm^{-1} may be localized. This was investigated by checking if Eq. 4.6 gives a reasonable fit to the $\{|\varepsilon_\alpha(b;s)|\}$. The fit was performed by:

1. Identifying the atom b_{max} with the largest eigenvector component in the mode s.

2. Calculating the distances from all other atoms $\{b\}$ to b_{max} modulo periodic boundary conditions. The formula used to calculate these distances is identical to Eq. 4.1 used to calculate the atomic drifts in Sect. 4.1.3.

3. Sorting the distances into 60 uniformly-spaced bins spanning 0–30 Å. The height of each bin is taken to be the average of the eigenvector norms it contains.

Fig. 4.14 shows the eigenvector decay profiles for a 622 cm^{-1} mode in a 4096-atom configuration of HEO. The curve marked 'linear' was obtained by taking the logarithm of the binned data and performing a linear fit. On the other hand, the curve marked 'exp' was obtained by fitting the data directly to Eq. 4.6. If the data were truly exponential, the same fit parameters should be obtained irrespective of the fitting scheme used; *i.e.* irrespective of whether the points are weighted linearly or exponentially [63]. Thus a figure-of-merit for the error in the localization length is the difference between the two $\{\xi\}$ in Fig. 4.14. This gives $\xi \sim 2.2(4)$ cm^{-1} which is indeed much smaller than the supercell lattice constant.

The decay profiles of 299 cm^{-1} mode are shown in Fig. 4.15. Observe that the localization length varies by an order of magnitude between the two fitting schemes. Under exponential weighting, the fit is dominated by the first two or three data points. A possible interpretation of this is that Eq. 4.6 is an inadequate model; the eigenvector components do not decay as a simple exponential, and the 299 cm^{-1} mode is therefore not localized.

It is worth mentioning that the data in Fig. 4.15 is better described by a sum of two exponentials, plus a DC offset to account for the downturn of the data near the supercell boundary. This is shown in Fig. 4.16. That two exponentials are required is interpreted as there being two localization processes: one which acts over a very short distance, and decays rapidly thereafter; and a second, weaker process which persists over much longer distances [63]. This can be seen in Fig. 4.13, where there is a cluster of intense oxygen vibrations at the centre of the cell, and weaker clusters scattered elsewhere.

Finally, the decay profiles of 147 cm^{-1} and 400 cm^{-1} modes are shown in Fig. 4.17. It is apparent from visual inspection and by comparison with Fig. 4.15 that these are extended modes.

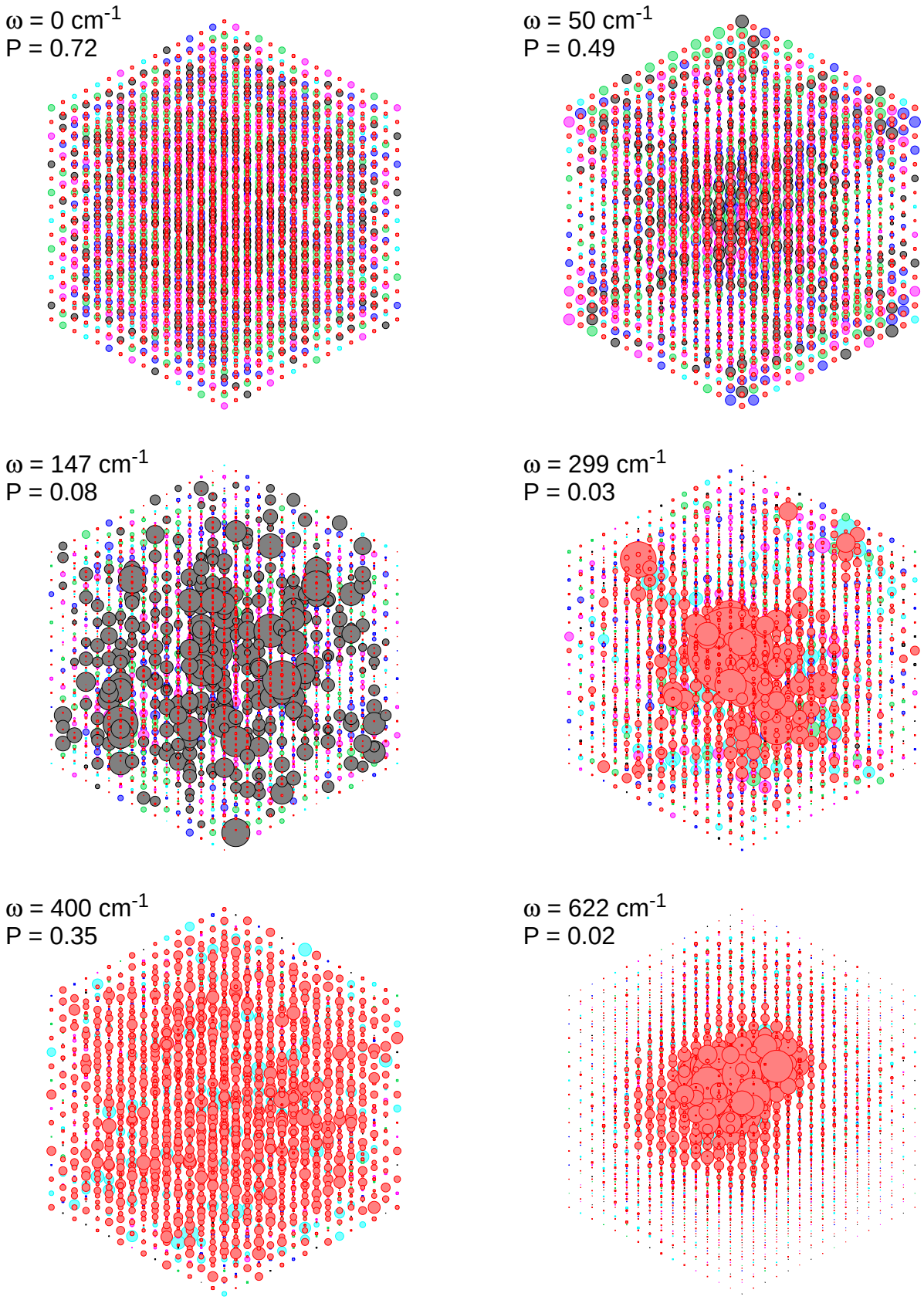

Figure 4.13: Bubble plots of select eigenmodes in a 4096-atom configuration of HEO. Refer to Fig. 1.1 for the colour scheme.

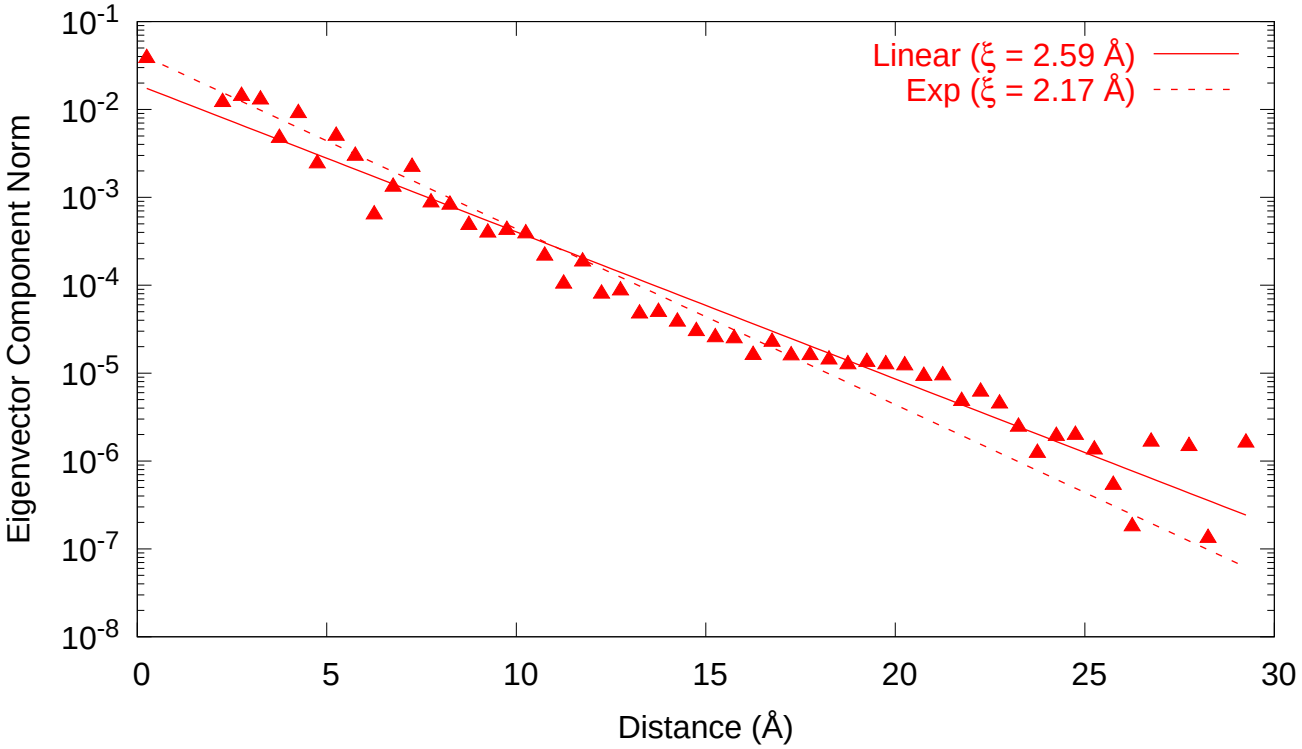

Figure 4.14: Eigenvector decay profiles of a 622 cm^{-1} mode in HEO.

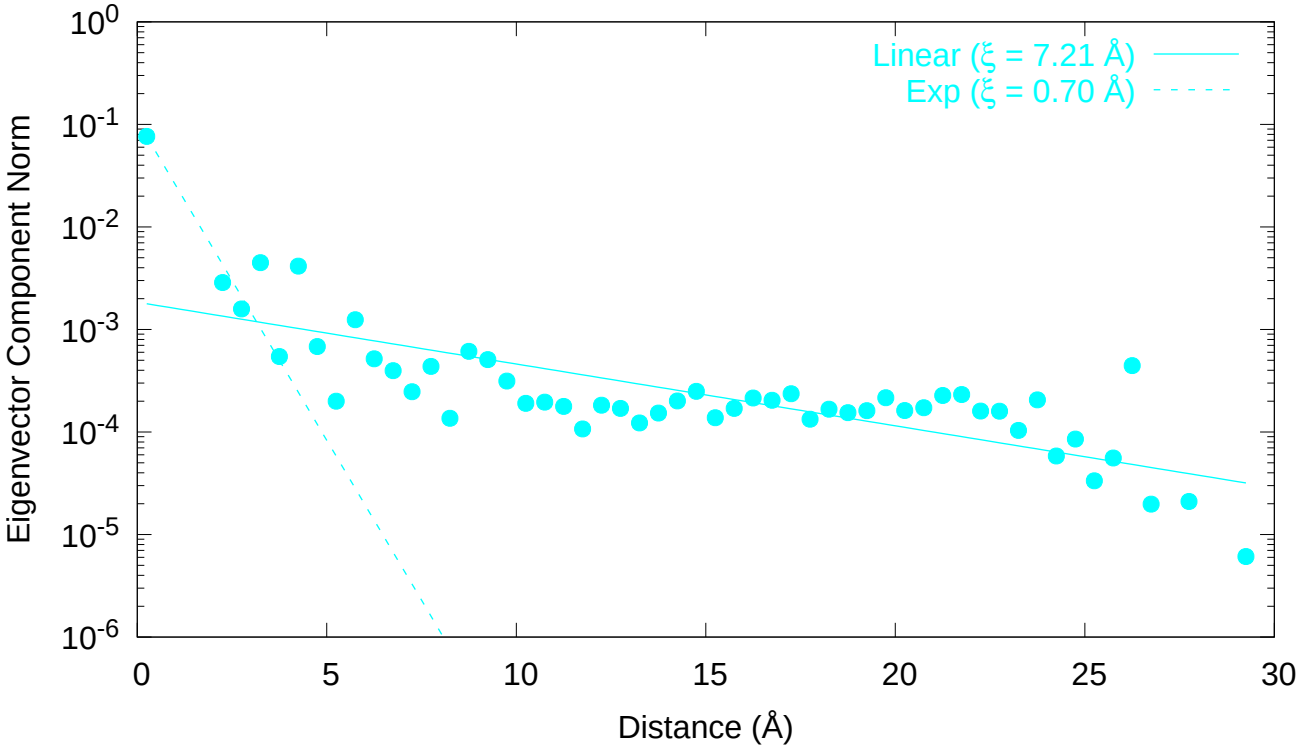

Figure 4.15: Eigenvector decay profiles of a 299 cm^{-1} mode in HEO.

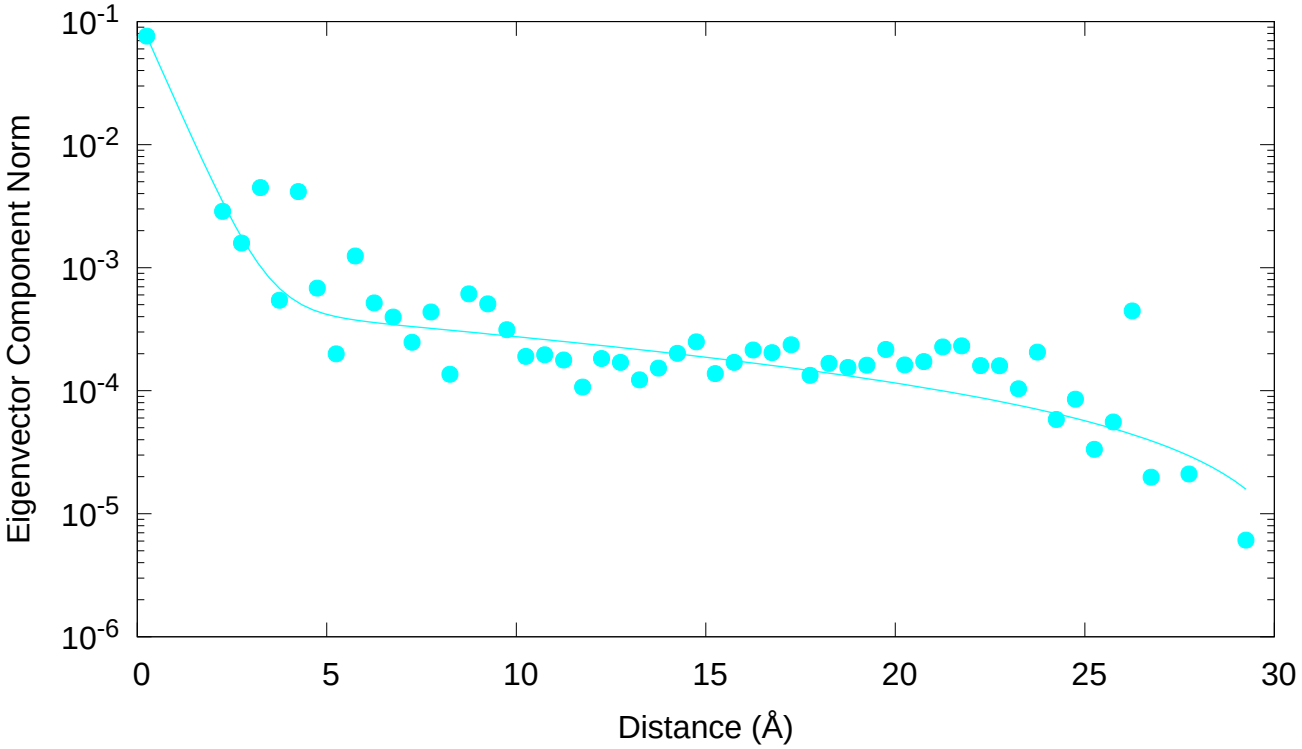

Figure 4.16: Multiexponential fit to the decay profile in Fig. 4.15.

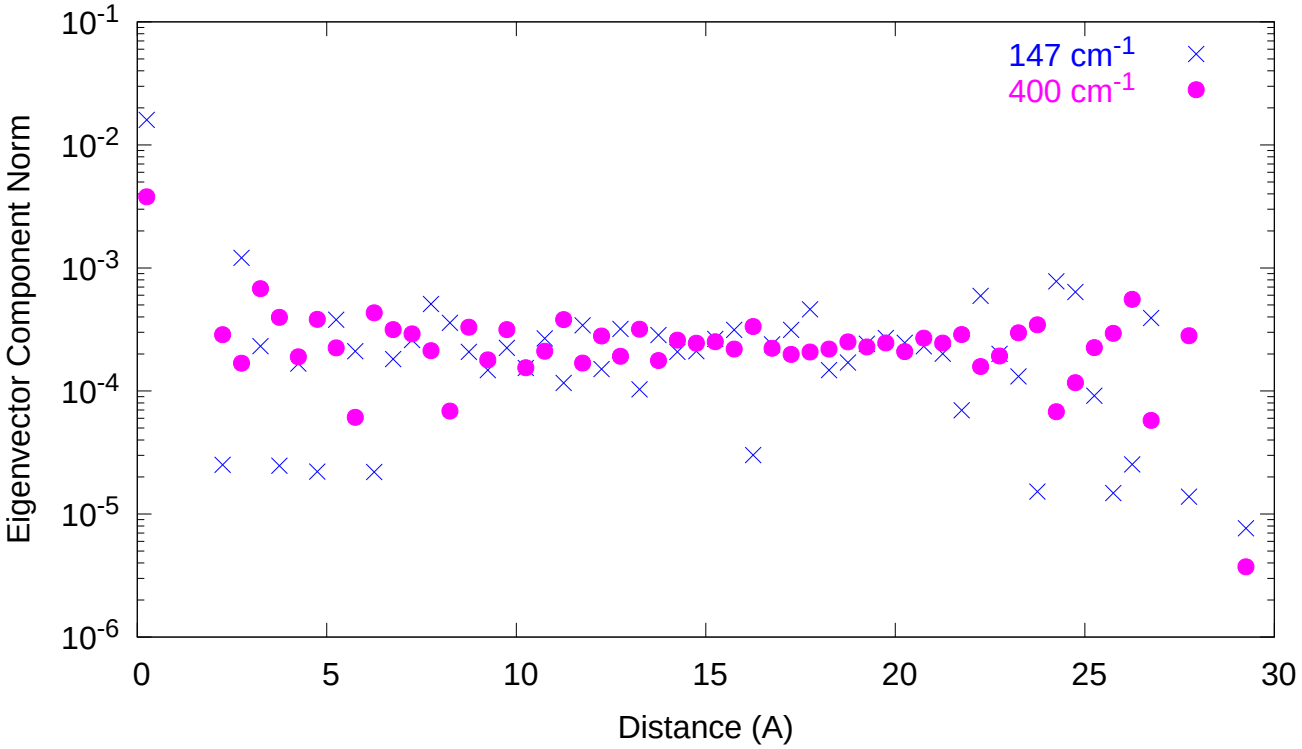

Figure 4.17: Eigenvector decay profiles of 147 cm^{-1} and 400 cm^{-1} modes in HEO.

4.3.4 Local Environment

It is interesting to ask why the 622 cm^{-1} locon forms on the particular oxygen ion that it does in Fig. 4.13. Denote by $(O)_{max}$ the oxygen ion with the largest eigenvector component in the highest-frequency eigenmode (in the particular configuration shown in Fig. 4.13, this is a frequency of 622 cm^{-1}). The distribution of first, third, and fifth nearest-neighbour (denoted '1NN', '3NN', and '5NN', respectively) cations surrounding $(O)_{max}$ is shown in Fig. 4.18. The distribution has been averaged over 50 disorder realizations of 4096-atom HEO. Observe that there is a strong preference for Mg cations as first nearest-neighbours. By the fifth nearest-neighbour shell, the distribution is nearly uniform; *i.e.* there is short-range ordering which persists over a distance $\sqrt{5}a/2 \sim 4.7$ Å. Physically, the locon is situated in a 'cage' of lighter Mg ions. There then must be an excess of Zn and heavier cations at distances from $(O)_{max}$ greater than the fifth nearest-neighbour shell, which insulate the vibration from the remainder of the supercell.

The median first nearest-neighbour cation-oxygen bond lengths surrounding $(O)_{max}$ were also investigated, but were identical within error to the bulk results reported in Table 4.2.

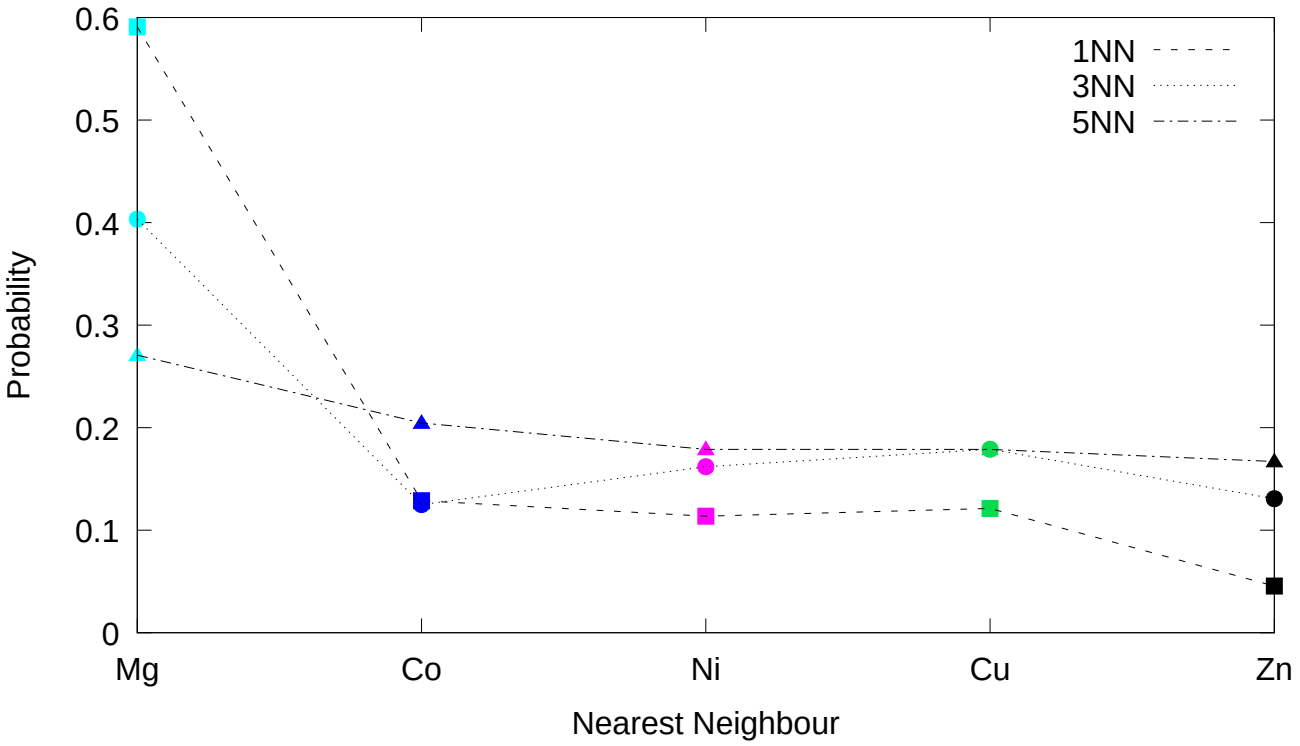

Figure 4.18: Distribution of cations surrounding the oxygen ion with the largest eigenvector component in a $\omega = 622$ cm^{-1} mode. The dotted lines correspond to various nearest-neighbour shells and are guides to the eye.

4.3.5 Level Statistics

Define by $\{\epsilon\}$ the differences between nearest-neighbour eigenvalues of a random matrix (the 'level spacings'). For vibrations in HEO or disordered media in general, these are the differences between adjacent squared eigenfrequencies; *i.e.* the eigenvalues of the dynamical matrix. According to random matrix theory (RMT) [64], the $\{\epsilon\}$ of a delocalized system are distributed according to the

Wigner-Dyson distribution

$$P(\epsilon) = \frac{\pi\,\epsilon}{2}\,\exp\left(-\frac{\pi\epsilon^2}{4}\right) \tag{4.7}$$

while for a localized system, they are distributed according to the Poisson distribution

$$P(\epsilon) = \exp(-\epsilon) \tag{4.8}$$

Thus a window of frequencies which produces level spacings conforming to the Poisson distribution would provide additional evidence for the existence of localized vibrational modes in HEO. Indeed, J. Fabian has previously shown that diffusons and locons in α-Si conform to the Wigner-Dyson and Poisson distributions, respectively [65].

The connection between localization and the eigenvalues of a random matrix is directly related to the phenomenon of 'level repulsion': for a delocalized system, the chance of finding two eigenvalues which are arbitrarily close together is vanishingly small. This follows by taking the $\epsilon \to 0$ limit of Eq. 4.7. Physically, since the eigenmodes are extended and mutually orthogonal, they "cannot have the same frequency given that they overlap in space" [66]. Conversely, locons are confined to a region of finite spatial extent and their frequencies are uncorrelated [66].

The predictions of RMT are valid for systems having a constant density-of-states [29]. It is immediately apparent from Fig. 4.19 that HEO does not fall into this category. Thus, before the level statistics can be calculated, the eigenfrequencies of HEO must first be 'unfolded' onto a constant density-of-states. This procedure is non-unique, and in this thesis, it consisted of the following four steps:

1. To increase the number of data points, the dynamical matrices of an additional eight 8000-atom supercells were diagonalized. The squared eigenfrequencies of 28 disorder realizations (20 configurations of 4096-atom HEO, plus the eight just discussed) were collected into a single file and sorted in ascending order. A plot of $\{\omega^2\}$ versus 'mode number' (*i.e.* the position of each frequency in the sorted list) generates the 'staircase function', or cumulative density function $C(\omega^2)$ shown in Fig. 4.20. Note that Fig. 4.20 has been normalized by the total number of modes.

2. Fit $C(\omega^2)$ to some phenomenological function which reproduces the staircase function. Polynomials are common in the literature. Motivated by the shape of Fig. 4.20 as a sum of 'smoothed steps', the following function was chosen:

$$C(\omega^2) = \sum_{i=1}^{3} a_i S_i(\omega^2) \qquad S_i(\omega^2) = 1 - \frac{1+\exp[-\omega^2/\Omega_i^2]}{1+\exp[(\omega^2-\omega_i^2)/\Omega_i^2]} \tag{4.9}$$

   subject to the constraints

$$a_i \geq 0\ \forall\ i \qquad \sum_{i=1}^{3} a_i = 1 \tag{4.10}$$

   Here the index i runs over the number of 'steps' in the fit; visual inspection of Fig. 4.20 suggested three steps was sufficient. The fit parameters $\{a_i, \Omega_i, \omega_i\}$ represent, repspectively, the height, width, and zero-crossing of each step. This particular form of $C(\omega^2)$ satisfies:

   (a) $C(0) = 0$

   (b) $C(\omega^2 \to \infty) = 1$

(c) $C(\omega^2)$ is monotonically increasing

which guarantee $C(\omega^2)$ is a *bona fide* cumulative density function for all values of the fit parameters. This is not in general true of a polynomial fit or a spline interpolation.

Due to the constraint Eq. 4.10, attempting to directly fit Eq. 4.9 to the eigenfrequencies was not successful. Instead, the following procedure was developed to gradually incorporate Eq. 4.10 into the fit. Excellent agreement with the $\{\omega_s^2\}$ was thus obtained.

(a) By process of trial-and-error, find a reasonable set of $\{a_i, \Omega_i, \omega_i\}$ and fit $C(\omega^2)$ to the $\{\omega_s^2\}$, allowing all 9 parameters to vary. Once the fit is complete, the sum $\sum_i a_i$ should not deviate too far from its requisite value of unity (it was observed $\sum_i a_i = 1.03$).

(b) The constraint equation in Eq. 4.10 is now used to eliminate one of the $\{a_i\}$. The parameter a_3 was chosen in the actual fit and will be singled out for explanatory purposes. The goal is to reduce $\sum_i a_i$ down from its current value of 1.03 to one. Fix $a_3 = 1.02 - a_1 - a_2$ and perform a second fit using as initial guesses for the other parameters the optimised values determined in (a).

(c) Fix $a_3 = 1.01 - a_1 - a_2$, where a_1, a_2, and the remaining parameters are set to the optimised values determined in (b). Perform another fit. This process is iterated a final time using $a_3 = 1 - a_1 - a_2$. If at any point a fit does not converge, a_3 can be brought down to unity in smaller increments.

3. The unfolded mode numbers $\{n_s = C(\omega_s^2)\}$ and level spacings $\{\epsilon_s = n_s - n_{s-1}\}$ were calculated from $C(\omega^2)$ for each of the frequency ranges shown in the upper panel of Fig. 4.21. The level spacings were normalized according to $\{\epsilon_s \to \epsilon_s / \langle \epsilon_s \rangle\}$, where $\langle \epsilon_s \rangle$ was taken to be the mean spacing in each range, then sorted into bins of width 0.25 (in units of $\langle \epsilon_s \rangle$).

4. The foregoing three steps generated 28 histograms, one for each disorder realization of HEO. A disorder average of these histograms was performed for each frequency range. The resulting averaged histograms are presented in the bottom panel of Fig. 4.21.

Before discussing any results, it is very important to emphasize that the Wigner-Dyson and Poisson distributions (as well as the level spacing ratio distributions to be discussed shortly) are derived assuming an entire window of frequencies. Here, except for the diffusons, eigenmodes have been selected on the bases of both frequency and participation ratio. This was done out of necessity: no agreement between the (alleged) locon modes and the Poisson distribution was observed by selecting according to frequency only. The locon level spacings should be treated with caution.

From Fig. 4.21, the level spacings of the modes with eigenfrequencies between 350–400 cm^{-1} are in excellent agreement with the Wigner-Dyson distribution. Given that these modes are far above the locon threshold of $P > 0.05$, and should therefore be delocalized, this is to be expected. More surprisingly, the modes between 100 cm^{-1} and 200 cm^{-1} also follow the Wigner-Dyson distribution despite satisfying $P < 0.1$. As discussed in Sect. 4.3.3, this suggests a cutoff of $P < 0.1$ is too relaxed for HEO and partially motivated the choice $P < 0.05$.

The cluster of modes at 300 cm^{-1} are in reasonable agreement with the Poisson distribution and should therefore be localized. The agreement between the high-frequency modes past the mobility edge and the Poisson distribution is, however, not satisfactory. It is conceivable that there are too few data points in this region to obtain good statistics: each 4096-atom configuration contains only

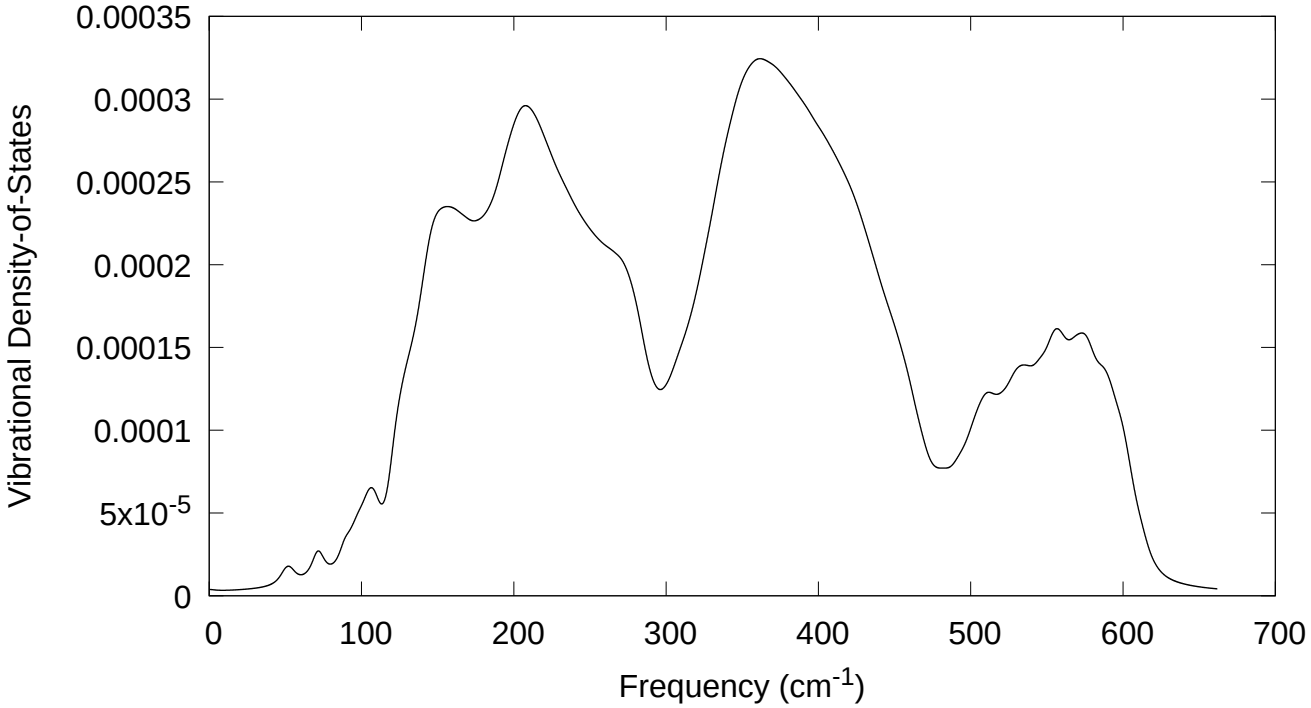

Figure 4.19: Vibrational density-of-states (VDOS) of a 4096-atom configuration of HEO normalized to unit intensity.

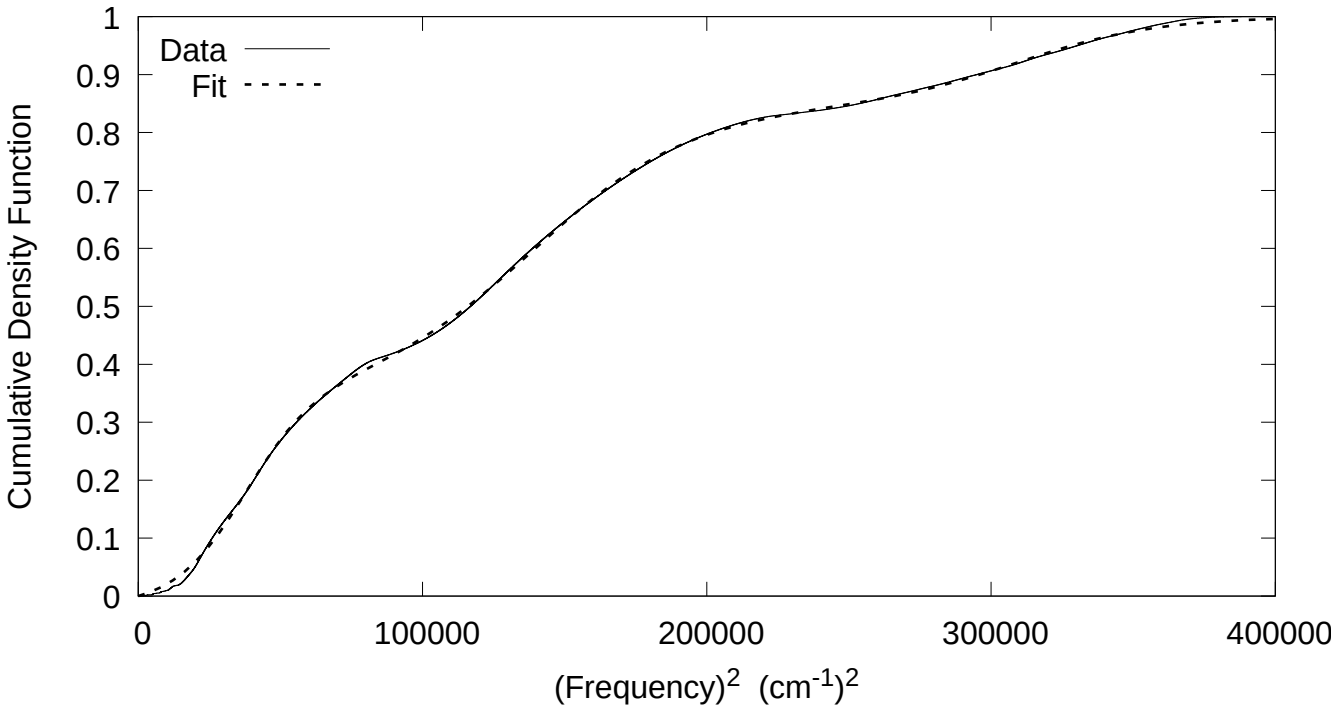

Figure 4.20: Cumulative density function (CDF) of the squared eigenfrequencies of HEO. The fit to Eq. 4.9 is shown by the dashed line.

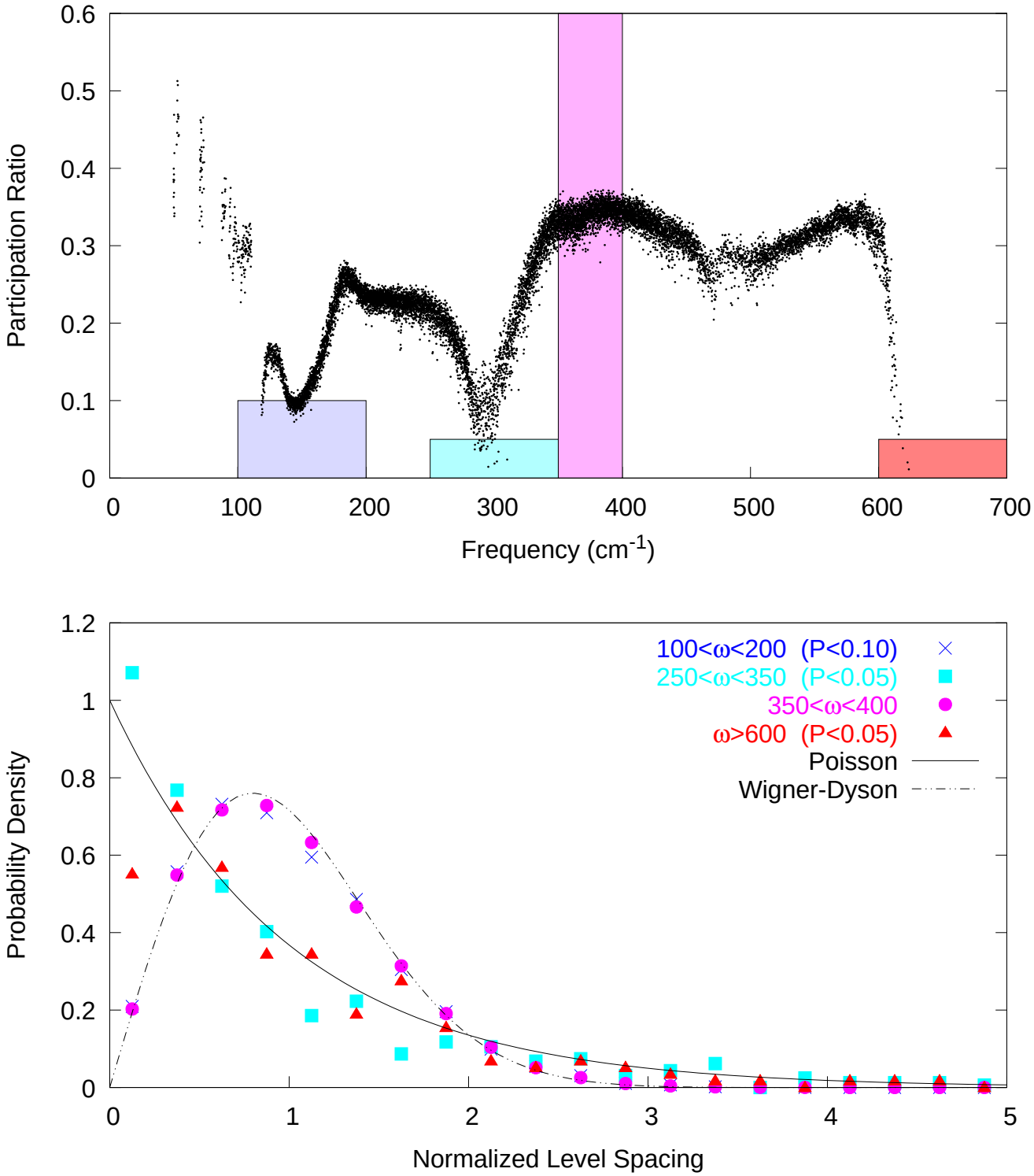

Figure 4.21: (Top panel): Participation ratio of a 4096-atom configuration of HEO. The frequency ranges in which the level statistics were studied are highlighted by shaded rectangles. (Bottom panel): Level spacing distributions in HEO. The colors of the points correspond to the rectangles in the upper panel.

$\sim 15/12,288$ of these high-frequency modes, compared to $\mathcal{O}(10^3)$ diffusons between 350–400 cm^{-1}.

Let $r_s = \epsilon_s/\epsilon_{s-1}$ be the ratio of consecutive level spacings. Recent papers have proposed that localized and extended systems can be distinguished from the distribution $P(r)$ of the $\{r\}$ [67]. Unlike the pure level spacings, the quantity $P(r)$ has the advantage of not requiring an unfolding scheme.

Analogues of the Wigner-Dyson and Poisson distrbutions exist for $P(r)$. The level spacing ratios for a localized system should be distributed according to

$$P(r) = \frac{1}{(1+r)^2} \tag{4.11}$$

while for an extended system in the Gaussian Orthogonal Ensemble

$$P(r) = \frac{27}{8}\frac{(r+r^2)}{(1+r+r^2)^{5/2}} \tag{4.12}$$

The level spacing ratio distributions are shown in Fig. 4.22. The colors of the points correspond to the frequency windows in the top panel of Fig. 4.21. Observe that modes between 350–400 cm^{-1} conform to Eq. 4.12 and are therefore diffusons. This agrees with the predictions of the pure level statistics and the participation ratio. In contradistinction to the pure level spacings, however, Fig. 4.22 suggests that modes near 300 cm^{-1} are diffusons. It further suggests that modes past the mobility edge are localized, the caveat discussed above notwithstanding.

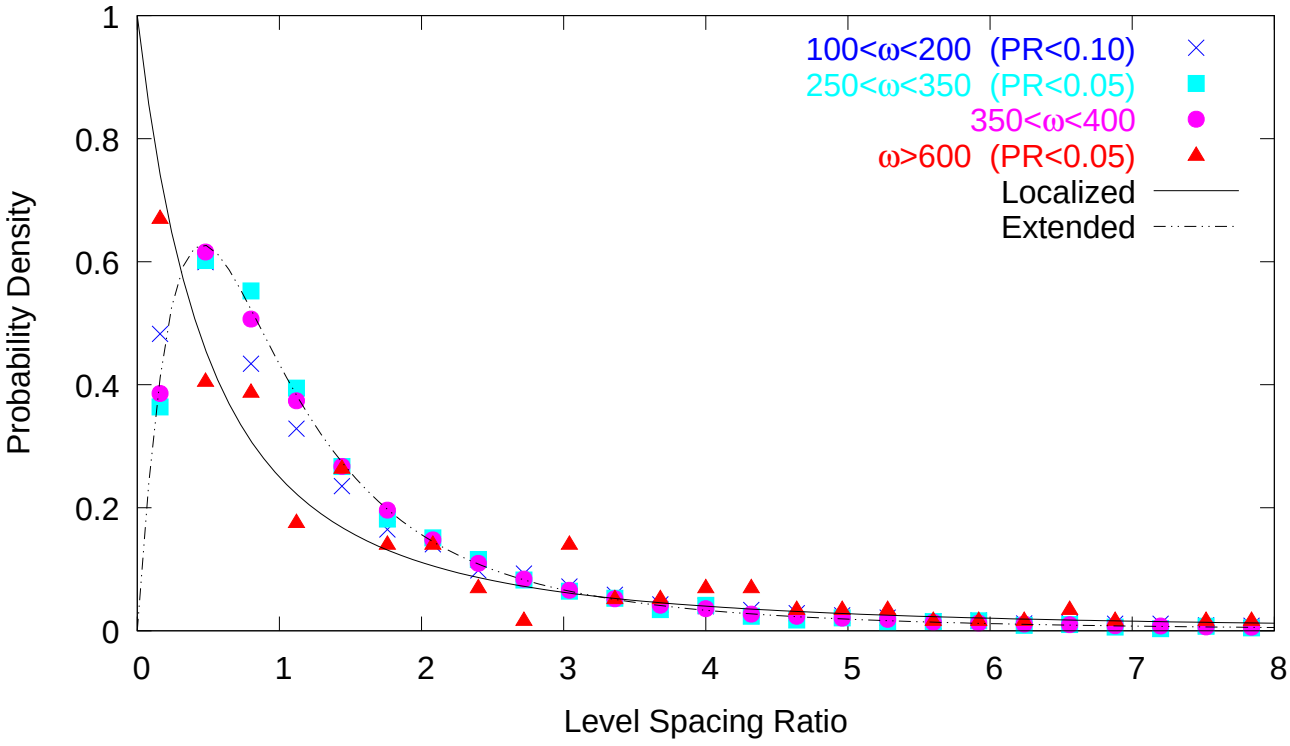

Figure 4.22: Level spacing ratio distributions in HEO. The colors correspond to the frequency windows in the top panel of Fig. 4.21. The 'localized' and 'extended' curves refer to Eqs. 4.11 and 4.12, respectively.

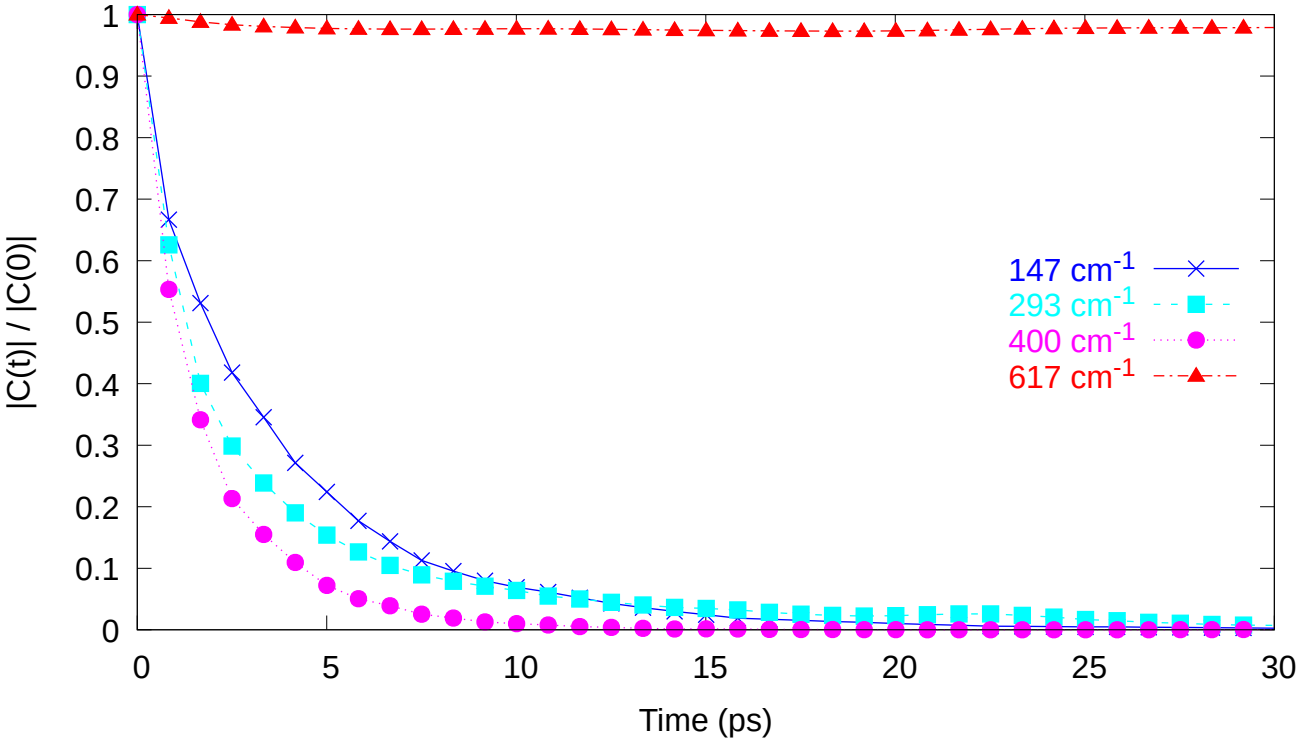

Figure 4.23: Correlation amplitude of select eigenmodes in HEO.

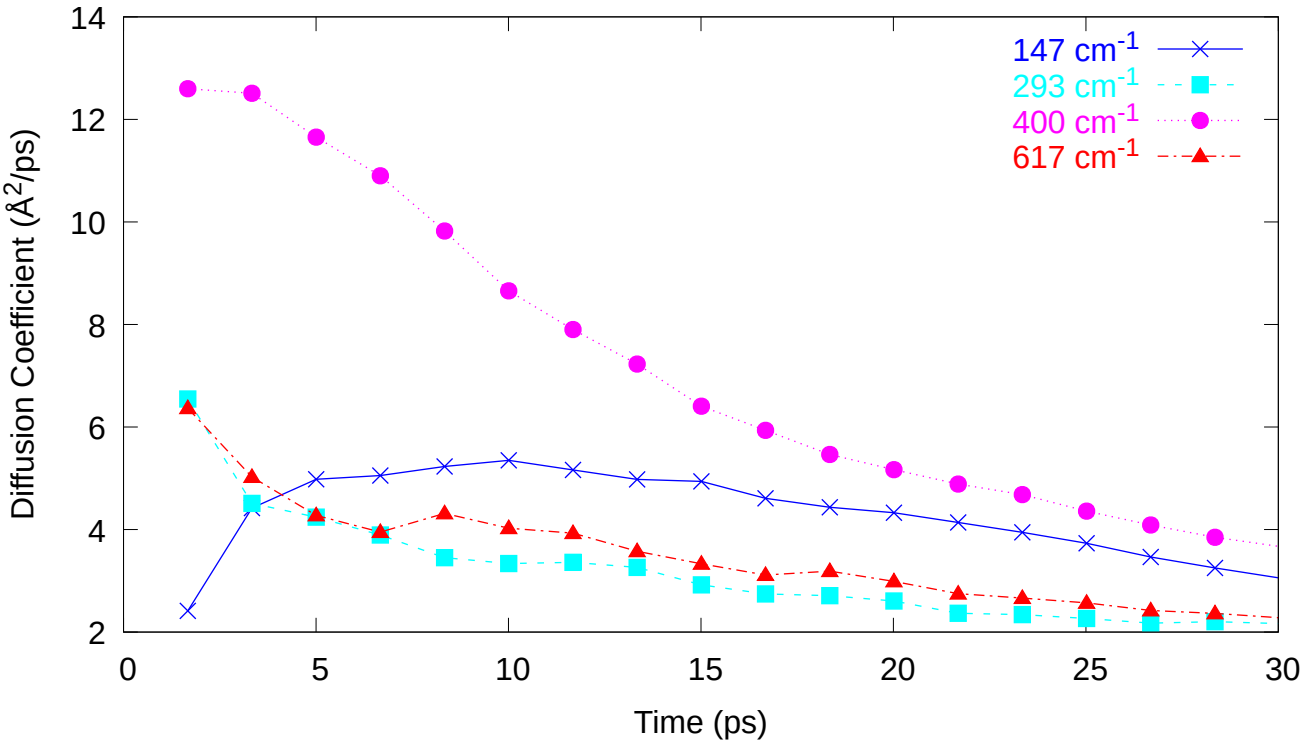

Figure 4.24: Diffusion coefficient of select eigemodes in HEO.

4.3.6 Wavepacket Dynamics

The wavepacket dynamics were studied by embedding a 1728-atom supercell of HEO in the centre of an 8000-atom environment. See Sect. 2.3 for the theoretical background on wavepacket dynamics. The correlation amplitude Eq. 2.52 of several eigenmodes[3] is shown in Fig. 4.23. Observe that the correlation amplitude of the 617 cm^{-1} mode remains close to unity for all time; *i.e.* the state of the system at later times always closely resembles the initial state. This suggests, in agreement with the tests previously discussed, that there are locons in HEO at high-frequency. The remaining modes in Fig. 4.23 decohere quickly and are therefore delocalized.

The diffusion coefficients Eq. 2.27 are shown in Fig. 4.24. The functional dependences of the diffusion coefficients on the time do not appear to agree with the predictions of Table 2.2. It is ultimately difficult to disentangle localization from finite-size effects. Possible improvement with the theory of Sect. 2.3 might be attained by embedding the 1728-atom cluster in a larger environment.

[3]It will be noted that the highest-frequency mode studied in all the tests so far has been 622 cm^{-1}. In Figs. 4.23 and 4.24, however, it is only 617 cm^{-1}. This is because the highest-frequency mode occurs at larger frequencies in the 4096-atom cells than the 1728-atom cell used here.

Chapter 5

Conclusions

It has been shown that the optical conductivity, bond lengths, and crystal structure of HEO are well-reproduced by a) a shell model description of the ions, and; b) parametrizing the short-range cation-oxygen interactions with the Buckingham potential. The weak mode in the optical conductivity reported by Afsharvosoughi and Crandles [15] is ascribed to a low-frequency, acoustic-like vibration of Zn ions against the stationary oxygen sublatttice. The combination of the participation ratio, mode polarization, level statistics, and correlation amplitude provide strong evidence for diffusons at frequencies between 350–400 cm^{-1}. Similarly, the participation ratio, eigenvector decay curves, and correlation amplitude suggest HEO supports high-frequency locons beyond the mobility edge in its vibrational density-of-states. Modes near 300 cm^{-1}, where the engagements transition from cation- to oxygen-dominated motion, are localized according to the participation ratio, but extended according to all other pieces of available evidence. It is likely that these modes are diffusons.

Insofar as this thesis employs the assumptions of Lewis and Catlow [43], and models HEO as a 'superposition' of its parent binary oxides, it is similar to previous lattice-dynamical studies by *e.g.* Anand et al. [18] and Chen et al. [19]. The new contributions to the literature are a) the introduction of interatomic potentials optimised for vibrational and dielectric properties, and; b) confirmation from numerous tests that localized vibrational modes do indeed exist in HEO.

The memory requirements of exact diagonalization limit the size of supercells `GULP` can handle to the order of 10^4 atoms. Future work might therefore include an application the kernel polynomial method [68] to calculate the spectrum of much larger supercells. It is conceivable that the greater pool of eigenvalues thus obtained will improve the agreement between the level statistics and the Poisson distribution. In addition, the existence of localized vibrational modes must still be verified by experiment. Theoretically, this could be done as follows: consider FTIR transmission/reflectance from an HEO thin film. The infrared spot size is made as small as possible. If a 400 cm^{-1} source is used to excite diffusons, the reflected intensity should not change significantly as the spot is swept across the sample. Conversely, if a 620 cm^{-1} source is used, a significant variation in intensity is expected wherever the source impinges upon a localized mode.

Appendix A

Experimental Data

In the tables below are presented the measured crystal structures, dielectric constants, and phonon frequencies used to fit the interatomic potentials for MgO, CoO, CuO, NiO, and ZnO. All measurements were performed at room temperature, unless otherwise indicated. For explicit reciprocal-space coordinates of the high-symmetry Brillouin zone points in Tables A.5 through A.9, refer to the `kvec` utility on the Bilbao Crystallographic Server [69, 70, 71, 72].

Abbreviation	Definition
COD	Crystallographic Database ID
SG	Space group (international notation)
INS	Inelastic neutron scattering
Ellips.	Ellipsometry
Cap.	Capacitance

Table A.1: List of abbreviations used in this appendix.

Oxide	Ref.	SG	COD	Cell Parameters					
				a (Å)	b (Å)	c (Å)	α (°)	β (°)	γ (°)
MgO	[73]	225	9006784	4.2128(2)	4.2128(2)	4.2128(2)	90	90	90
CoO	[74]	225	–	4.2614(3)	4.2614(3)	4.2614(3)	90	90	90
NiO	[75]	225	4329323	4.1786(2)	4.1786(2)	4.1786(2)	90	90	90
CuO	[76]	15	7212242	4.6837(5)	3.4226(5)	5.1288(6)	90	99.54(1)	90
ZnO	[77]	186	2300112	3.24931(2)	3.24931(2)	5.20571(4)	90	90	120

Table A.2: Conventional cell parameters and space groups. With the exception of β for CuO, all angles are exact by symmetry.

Oxide	A			O		
	x	y	z	x	y	z
MgO	0	0	0	½	½	½
CoO	0	0	0	½	½	½
NiO	0	0	0	½	½	½
CuO	¼	¼	0	0	0.418(1)	¼
ZnO	⅓	⅔	0	⅓	⅔	0.382(1)

Table A.3: Atomic coordinates in the primitive unit cell. Entries marked '0' or which are pure fractions are exact by symmetry. Entries which are decimal values were taken from the COD files listed in Table A.3.

Oxide	Ref.	Method	Component						
				xx	xy	xz	yy	yz	zz
MgO	[78]	IR	ϵ_∞	2.9(2)	0	0	2.9(2)	0	2.9(2)
	[79]	Cap.	ϵ_0	9.96(5)	0	0	9.96(5)	0	9.96(5)
CoO	[80]	IR	ϵ_∞	5.3(1)	0	0	5.3(1)	0	5.3(1)
	[81]	Cap.	ϵ_0	12.9(1)	0	0	12.9(1)	0	12.9(1)
NiO	[82]	Ellips.	ϵ_∞	4.97(1)	0	0	4.97(1)	0	4.97(1)
	[81]	Cap.	ϵ_0	11.9(1)	0	0	11.9(1)	0	11.9(1)
CuO	[83]	IR	ϵ_∞	7.3	0	-0.8	5.9	0	6.8
ZnO	[84]	Ellips.	ϵ_∞	3.70(1)	0	0	3.70(1)	0	3.78(5)
			ϵ_0	7.77(3)	0	0	7.77(3)	0	8.91(9)

Table A.4: Static and high-frequency dielectric constants. Entries marked "0" are identically equal to zero by symmetry. No values of ϵ_0 for CuO were found in the available literature.

	MgO								
	Γ	Ref.	Method	X	Ref.	Method	L	Ref.	Method
ω_{TA_1}	0	–	–	299(8)	[85]	INS	288(8)	[85]	INS
ω_{TA_2}	0	–	–	299(8)	[85]	INS	288(8)	[85]	INS
ω_{LA}	0	–	–	422(8)	[85]	INS	–	–	
ω_{TO_1}	396.6(5)	[78]	IR	443(8)	[85]	INS	369(8)	[85]	INS
ω_{TO_2}	396.6(5)	[78]	IR	443(8)	[85]	INS	369(8)	[85]	INS
ω_{LO}	724(6)	[78]	IR	554(8)	[85]	INS	–	–	–

Table A.5: Phonon frequencies of MgO. Frequencies at X, L points adapted from Table 3 in Schutt et al. [85], who digitized the INS work of Sangster et al. [22]. The error in all X, L frequencies is estimated to be 8 cm^{-1}, which is the largest experimental error reported by Sangster et al.

	CoO								
	Γ	Ref.	Method	X	Ref.	Method	L	Ref.	Method
ω_{TA_1}	0	–	–	151(8)	[86]	INS	172(8)	[86]	INS
ω_{TA_2}	0	–	–	151(8)	[86]	INS	172(8)	[86]	INS
ω_{LA}	0	–	–	240(8)	[86]	INS	–	–	–
ω_{TO_1}	335.7(3)	[87]	IR	–	–	–	–	–	–
ω_{TO_2}	335.7(3)	[87]	IR	–	–	–	–	–	–
ω_{LO}	562.1(3)	[87]	IR	–	–	–	–	–	–

Table A.6: Phonon frequencies of CoO. Errors from Kant et al. [87] assumed equal to the one-half of the instrument resolution of 0.5 cm^{-1} (Bruker IFS 66v/s and IFC 113v IR spectrometers). Sakurai et al. [86] do not estimate errors in their INS frequencies, but do claim 0.15 THz "is well below the experimental resolution". Therefore, the same error estimate in the X, L frequencies as was used for MgO is adopted for CoO, the Sangster et al. [22] and Sakurai papers being contemporaneous.

	NiO								
	Γ	Ref.	Method	X	Ref.	Method	L	Ref.	Method
ω_{TA_1}	0	–	–	181(3)	[88]	INS	203(2)	[88]	INS
ω_{TA_2}	0	–	–	181(3)	[88]	INS	203(2)	[88]	INS
ω_{LA}	0	–	–	275(3)	[88]	INS	332(3)	[88]	INS
ω_{TO_1}	392.9(4)	[82]	Ellips.	430(5)	[88]	INS	337(7)	[88]	INS
ω_{TO_2}	392.9(4)	[82]	Ellips.	430(5)	[88]	INS	337(7)	[88]	INS
ω_{LO}	593.9(5)	[82]	Ellips.	477(7)	[88]	INS	544(7)	[88]	INS

Table A.7: Phonon frequencies of NiO.

Mode No.	CuO					
	Γ	Ref.	Method	A	Ref.	Method
1	0	–	–	62(3)	[89]	INS
2	0	–	–	62(3)	[89]	INS
3	0	–	–	108(5)	[89]	INS
4	148.0(6)	[90]	IR	108(5)	[89]	INS
5	163.4(7)	[90]	IR	230(12)	[89]	INS
6	297.7(2)	[90]	Raman	230(12)	[89]	INS
7	320(3)	[90]	IR	367(18)	[89]	INS
8	345.9(6)	[90]	Raman	367(18)	[89]	INS
9	401(11)	[90]	IR	440(22)	[89]	INS
10	481(5)	[90]	IR	440(22)	[89]	INS
11	557(5)	[90]	IR	633(32)	[89]	INS
12	630(6)	[90]	Raman	633(32)	[89]	INS

Table A.8: Phonon frequencies of CuO.

Mode No.	ZnO								
	Γ	Ref.	Method	A	Ref.	Method	H	Ref.	Method
1	0	–	–	80	[91]	INS	102	[91]	INS
2	0	–	–	80	[91]	INS	102	[91]	INS
3	0	–	–	80	[91]	INS	170	[91]	INS
4	102(1)	[84]	Raman	80	[91]	INS	170	[91]	INS
5	102(1)	[84]	Raman	182	[91]	INS	257	[91]	INS
6	259	[91]	INS	182	[91]	INS	257	[91]	INS
7	379(2)	[84]	Raman	427	[91]	INS	448	[91]	INS
8	410(2)	[84]	Raman	427	[91]	INS	448	[91]	INS
9	437(1)	[84]	Raman	427	[91]	INS	508	[91]	INS
10	437(1)	[84]	Raman	427	[91]	INS	508	[91]	INS
11	552	[91]	INS	562	[91]	INS	542	[91]	INS
12	573	[91]	INS	562	[91]	INS	542	[91]	INS

Table A.9: Phonon frequencies of ZnO. Errors from Serrano et al. [91] assumed equal to the one-half of the instrument resolution of 32 cm^{-1} (IN1 triple axis spectrometer, Institut Laue Langevin, Grenoble, France). INS frequencies were acquired at 10 K; however, "the effect of temperature on the phonon frequencies is completely masked by the energy resolution" [91]. Only the Γ, A frequencies were used during fitting.

Appendix B

Interatomic Potential Comparison

In this Chapter, the observables calculated from the interatomic potentials developed in Sect. 3.1 are compared to existing potentials used by Chen et al. [19]. All cell lengths a, b, c and internal coordinates u are measured in Angstrom. All cell angles α, β, γ are measured in degrees. All phonon frequencies are measured in wavenumbers.

	MgO		
	Expt.	Chen et al. [19]	This work
a	4.2128(2)	4.1329	4.2127
ϵ_∞	2.9(2)	2.3	3.0
ϵ_0	9.96(5)	26.53	9.91
ω_{Γ_4}	396.6(5)	237.2	396.1
ω_{Γ_5}	396.6(5)	237.2	396.1
ω_{Γ_6}	724(6)	797.7	718.5
ω_{X_1}	299(8)	253.8	303.4
ω_{X_2}	299(8)	253.8	303.4
ω_{X_3}	422(8)	398.8	448.3
ω_{X_4}	443(3)	398.8	448.3
ω_{X_5}	443(8)	473.9	464.0
ω_{X_6}	554(8)	566.5	555.6
ω_{L_1}	288(8)	213.9	285.1
ω_{L_2}	288(8)	213.9	285.1
ω_{L_3}	369(8)	256.9	347.4
ω_{L_4}	369(8)	256.9	347.4
ω_{L_5}	–	598.0	564.7
ω_{L_6}	–	664.6	601.3

Table B.1: Comparison of MgO observables to experiment and Chen et al. [19]. Both sets of potentials incorrectly predict the LA and TO branches cross at the X point.

	CoO		
	Expt.	Chen et al. [19]	This work
a	4.2614(3)	4.2446	4.2638
ϵ_∞	5.3(1)	2.2	4.8
ϵ_0	12.9(1)	17.8	13.2
ω_{Γ_4}	335.7(3)	242.9	336.1
ω_{Γ_5}	335.7(3)	242.9	336.1
ω_{Γ_6}	562.1(3)	688.6	557.9
ω_{X_1}	151(8)	185.9	194.0
ω_{X_2}	151(8)	185.9	194.0
ω_{X_3}	240(8)	266.0	276.9
ω_{X_4}	–	370.7	399.3
ω_{X_5}	–	370.7	399.3
ω_{X_6}	–	561.8	494.5
ω_{L_1}	172(8)	145.2	180.0
ω_{L_2}	172(8)	145.2	180.0
ω_{L_3}	–	273.9	301.8
ω_{L_4}	–	273.9	340.2
ω_{L_5}	–	414.6	340.2
ω_{L_6}	–	590.6	595.4

Table B.2: Comparison of CoO observables to experiment and Chen et al. [19].

	NiO		
	Expt.	Chen et al. [19]	This work
a	4.1786(2)	4.1786	4.1862
ϵ_∞	4.97(1)	2.28	5.02
ϵ_0	11.9(1)	20.6	11.6
ω_{Γ_4}	392.9(4)	231.9	388.8
ω_{Γ_5}	392.9(4)	231.9	388.8
ω_{Γ_6}	593.9(5)	695.7	591.4
ω_{X_1}	181(3)	184.3	201.2
ω_{X_2}	181(3)	184.3	201.2
ω_{X_3}	275(3)	264.3	296.6
ω_{X_4}	430(5)	371.9	435.8
ω_{X_5}	430(5)	371.9	435.8
ω_{X_6}	477(7)	567.7	506.8
ω_{L_1}	203(2)	143.6	204.2
ω_{L_2}	203(2)	143.6	204.2
ω_{L_3}	332(3)	269.5	326.7
ω_{L_4}	337(7)	269.5	382.7
ω_{L_5}	337(7)	423.4	382.7
ω_{L_6}	544(7)	595.9	612.5

Table B.3: Comparison of NiO observables to experiment and Chen et al. [19].

CuO			
	Expt.	Chen et al. [19]	This work
a	4.6837(5)	6.3851	4.8659
b	3.4226(5)	2.8539	3.1936
c	5.1288(6)	6.3851	5.0180
u	0.418(1)	0.250	0.373
β	99.54(1)	126.90	100.79
ϵ^{∞}_{xx}	7.3(1)	1.9	6.4
ϵ^{∞}_{xz}	-0.8(1)	-2.5	-0.6
ϵ^{∞}_{yy}	5.9(1)	28.7	5.0
ϵ^{∞}_{zz}	6.8(1)	30.7	6.1
ω_{Γ_4}	148.0(6)	77.5	117.9
ω_{Γ_5}	163.4(7)	96.2	143.3
ω_{Γ_6}	297.7(2)	130.2	290.8
ω_{Γ_7}	320(3)	137.3	312.5
ω_{Γ_8}	345.9(6)	181.1	365.6
ω_{Γ_9}	401(11)	224.7	393.4
$\omega_{\Gamma_{10}}$	481(5)	365.7	458.3
$\omega_{\Gamma_{11}}$	557(5)	580.0	592.2
$\omega_{\Gamma_{12}}$	630(6)	662.9	646.9
ω_{A_1}	62(3)	40.5	95.0
ω_{A_2}	62(3)	40.5	95.0
ω_{A_3}	108(5)	87.5	101.9
ω_{A_4}	108(5)	87.5	101.9
ω_{A_5}	230(12)	150.3	232.2
ω_{A_6}	230(12)	150.3	232.2
ω_{A_7}	367(18)	184.4	314.0
ω_{A_8}	367(18)	184.4	314.0
ω_{A_9}	440(22)	249.0	420.5
$\omega_{A_{10}}$	440(22)	249.0	420.5
$\omega_{A_{11}}$	633(32)	627.3	632.8
$\omega_{A_{12}}$	633(32)	627.3	632.8

Table B.4: Comparison of CuO observables to experiment and Chen et al. [19].

	ZnO		
	Expt.	Chen et al. [19]	This work
a	3.24931(2)	3.26761	3.28381
c	5.20571(4)	5.07402	5.13173
u	0.382(1)	0.392	0.390
ϵ_{xx}^{∞}	3.70(1)	1.90	3.65
ϵ_{zz}^{∞}	3.78(5)	1.92	3.83
ϵ_{xx}^{0}	7.77(3)	6.43	7.82
ϵ_{zz}^{0}	8.91(9)	8.74	10.71
ω_{Γ_4}	102(1)	140.0	122.6
ω_{Γ_5}	102(1)	140.0	122.6
ω_{Γ_6}	259(16)	303.3	203.1
ω_{Γ_7}	379(2)	305.7	261.4
ω_{Γ_8}	410(2)	367.2	305.2
ω_{Γ_9}	437(1)	383.5	342.9
$\omega_{\Gamma_{10}}$	437(1)	383.5	342.9
$\omega_{\Gamma_{11}}$	552(16)	570.7	446.8
$\omega_{\Gamma_{12}}$	573(16)	674.8	530.7
ω_{A_1}	80(16)	102.5	94.3
ω_{A_2}	80(16)	102.5	94.3
ω_{A_3}	80(16)	102.5	94.3
ω_{A_4}	80(16)	102.5	94.3
ω_{A_5}	182(16)	196.2	159.5
ω_{A_6}	182(16)	196.2	159.5
ω_{A_7}	427(16)	374.8	324.2
ω_{A_8}	427(16)	374.8	324.2
ω_{A_9}	427(16)	374.8	324.2
$\omega_{A_{10}}$	427(16)	374.8	324.2
$\omega_{A_{11}}$	562(16)	618.6	481.9
$\omega_{A_{12}}$	562(16)	618.6	481.9

Table B.5: Comparison of ZnO observables to experiment and Chen et al. [19].

Bibliography

[1] Christina M. Rost et al. "Entropy-stabilized oxides". In: *Nature Communications* 6.1 (Sept. 2015), p. 8485. ISSN: 2041-1723. DOI: 10.1038/ncomms9485. URL: https://doi.org/10.1038/ncomms9485.

[2] Alexander D. Dupuy et al. "Hidden transformations in entropy-stabilized oxides". In: *Journal of the European Ceramic Society* 41.13 (2021), pp. 6660–6669. ISSN: 0955-2219. DOI: https://doi.org/10.1016/j.jeurceramsoc.2021.06.014. URL: https://www.sciencedirect.com/science/article/pii/S095522192100426X.

[3] Brianna Musicó et al. "Tunable magnetic ordering through cation selection in entropic spinel oxides". In: *Phys. Rev. Mater.* 3 (10 Oct. 2019), p. 104416. DOI: 10.1103/PhysRevMaterials.3.104416. URL: https://link.aps.org/doi/10.1103/PhysRevMaterials.3.104416.

[4] Wei Xiong et al. "Low-loss high entropy relaxor-like ferroelectrics with A-site disorder". In: *Journal of the European Ceramic Society* 41.4 (2021), pp. 2979–2985. ISSN: 0955-2219. DOI: https://doi.org/10.1016/j.jeurceramsoc.2020.11.030. URL: https://www.sciencedirect.com/science/article/pii/S0955221920309298.

[5] Solveig S. Aamlid et al. "Phase stability of entropy stabilized oxides with the α-PbO2 structure". In: *Communications Materials* 4.1 (June 2023), p. 45. ISSN: 2662-4443. DOI: 10.1038/s43246-023-00372-5. URL: https://doi.org/10.1038/s43246-023-00372-5.

[6] Brianna L. Musicó et al. "The emergent field of high entropy oxides: Design, prospects, challenges, and opportunities for tailoring material properties". In: *APL Materials* 8.4 (2020), p. 040912. DOI: 10.1063/5.0003149. eprint: https://doi.org/10.1063/5.0003149. URL: https://doi.org/10.1063/5.0003149.

[7] Solveig S. Aamlid et al. "Understanding the Role of Entropy in High Entropy Oxides". In: *Journal of the American Chemical Society* 145.11 (2023). PMID: 36881986, pp. 5991–6006. DOI: 10.1021/jacs.2c11608. eprint: https://doi.org/10.1021/jacs.2c11608. URL: https://doi.org/10.1021/jacs.2c11608.

[8] Martina Fracchia et al. "Is configurational entropy the main stabilizing term in rock-salt Mg0.2Co0.2Ni0.2Cu0.2Zn0.2O high entropy oxide?" In: *Nature Communications* 13.1 (May 2022), p. 2977. ISSN: 2041-1723. DOI: 10.1038/s41467-022-30674-0. URL: https://doi.org/10.1038/s41467-022-30674-0.

[9] George N. Kotsonis et al. "High-entropy oxides: Harnessing crystalline disorder for emergent functionality". In: *Journal of the American Ceramic Society* 106.10 (2023), pp. 5587–5611. DOI: https://doi.org/10.1111/jace.19252. eprint: https://ceramics.onlinelibrary.wiley.com/doi/pdf/10.1111/jace.19252. URL: https://ceramics.onlinelibrary.wiley.com/doi/abs/10.1111/jace.19252.

[10] M. Lim et al. "Influence of mass and charge disorder on the phonon thermal conductivity of entropy stabilized oxides determined by molecular dynamics simulations". In: *Journal of Applied Physics* 125.5 (Feb. 2019), p. 055105. ISSN: 0021-8979. DOI: 10.1063/1.5080419. eprint: https://pubs.aip.org/aip/jap/article-pdf/doi/10.1063/1.5080419/13680677/055105_1_online.pdf. URL: https://doi.org/10.1063/1.5080419.

[11] Jeffrey L. Braun et al. "Charge-Induced Disorder Controls the Thermal Conductivity of Entropy-Stabilized Oxides". In: *Advanced Materials* 30.51 (2018), p. 1805004. DOI: https://doi.org/10.1002/adma.201805004. eprint: https://onlinelibrary.wiley.com/doi/pdf/10.1002/adma.201805004. URL: https://onlinelibrary.wiley.com/doi/abs/10.1002/adma.201805004.

[12] Hui Yang and Nianqiang Wu. "Ionic conductivity and ion transport mechanisms of solid-state lithium-ion battery electrolytes: A review". In: *Energy Science & Engineering* 10.5 (2022), pp. 1643–1671.

[13] D. Berardan et al. "Controlled Jahn-Teller distortion in (MgCoNiCuZn)O-based high entropy oxides". In: *Journal of Alloys and Compounds* 704 (2017), pp. 693–700. ISSN: 0925-8388. DOI: https://doi.org/10.1016/j.jallcom.2017.02.070. URL: https://www.sciencedirect.com/science/article/pii/S0925838817304863.

[14] Qingsong Wang et al. "Multi-anionic and -cationic compounds: new high entropy materials for advanced Li-ion batteries". In: *Energy Environ. Sci.* 12 (8 2019), pp. 2433–2442. DOI: 10.1039/C9EE00368A. URL: http://dx.doi.org/10.1039/C9EE00368A.

[15] Tahereh Afsharvosoughi and D. A. Crandles. "An infrared study of antiferromagnetic medium and high entropy rocksalt structure oxides". In: *Journal of Applied Physics* 130.18 (2021), p. 184103. DOI: 10.1063/5.0070994. eprint: https://doi.org/10.1063/5.0070994. URL: https://doi.org/10.1063/5.0070994.

[16] Tahereh Afsharvosoughi. "Structural, Magnetic, and Vibrational Studies of Entropy Stabilized Oxides". Supervised by David Crandles. PhD thesis. Brock University, 2021. URL: http://hdl.handle.net/10464/15128.

[17] M. N. Luckyanova et al. "Phonon localization in heat conduction". In: *Science Advances* 4.12 (2018), eaat9460. DOI: 10.1126/sciadv.aat9460. eprint: https://www.science.org/doi/pdf/10.1126/sciadv.aat9460. URL: https://www.science.org/doi/abs/10.1126/sciadv.aat9460.

[18] G. Anand et al. "Phase stability and distortion in high-entropy oxides". In: *Acta Materialia* 146 (2018), pp. 119–125. ISSN: 1359-6454. DOI: https://doi.org/10.1016/j.actamat.2017.12.037. URL: https://www.sciencedirect.com/science/article/pii/S1359645417310492.

[19] Jian Chen et al. "Stability and Compressibility of Cation-Doped High-Entropy Oxide MgCoNiCuZnO5". In: *The Journal of Physical Chemistry C* 123.29 (2019), pp. 17735–17744. DOI: 10.1021/acs.jpcc.9b04992. eprint: https://doi.org/10.1021/acs.jpcc.9b04992. URL: https://doi.org/10.1021/acs.jpcc.9b04992.

[20] G. P. Srivastava. *The Physics of Phonons*. 1st ed. Routledge, 1990. DOI: 10.1201/9780203736241.

[21] Giorgia Fugallo, Benoit Rousseau, and Michele Lazzeri. "Infrared reflectance, transmittance, and emittance spectra of MgO from first principles". In: *Phys. Rev. B* 98 (18 Nov. 2018), p. 184307. DOI: 10.1103/PhysRevB.98.184307. URL: https://link.aps.org/doi/10.1103/PhysRevB.98.184307.

[22] M J L Sangster, G Peckham, and D H Saunderson. "Lattice dynamics of magnesium oxide". In: *Journal of Physics C: Solid State Physics* 3.5 (May 1970), p. 1026. DOI: 10.1088/0022-3719/3/5/017. URL: https://dx.doi.org/10.1088/0022-3719/3/5/017.

[23] D.C. Wallace. *Thermodynamics of Crystals*. Dover Books on Physics. Dover Publications, 1998. ISBN: 9780486402123.

[24] F.W. Byron and R.W. Fuller. *Mathematics of Classical and Quantum Physics*. Dover Books on Physics. Dover Publications, 2012. ISBN: 9780486135069.

[25] Julian D. Gale. *General Utility Lattice Program*. English. Version 6.0. Curtin Institute for Computation, School of Molecular and Life Sciences, Curtin University. 181 pp.

[26] Peter Brüesch. *Phonons: Theory and Experiments I. Lattice Dynamics and Models of Interatomic Forces*. 1st ed. Springer Series in Solid-State Sciences. Springer Berlin, Heidelberg, 1982. ISBN: 3-540-11306-1.

[27] B. G. Dick and A. W. Overhauser. "Theory of the Dielectric Constants of Alkali Halide Crystals". In: *Phys. Rev.* 112 (1 Oct. 1958), pp. 90–103. DOI: 10.1103/PhysRev.112.90. URL: https://link.aps.org/doi/10.1103/PhysRev.112.90.

[28] Philip Phillips. *Advanced Solid State Physics*. 2nd ed. Cambridge University Press, 2012. DOI: 10.1017/CBO9781139031066.

[29] Ling Zhang et al. "Level statistics and Anderson delocalization in two-dimensional granular materials". In: *Phys. Rev. B* 103 (10 Mar. 2021), p. 104201. DOI: 10.1103/PhysRevB.103.104201. URL: https://link.aps.org/doi/10.1103/PhysRevB.103.104201.

[30] David W. Snoke. *Solid State Physics: Essential Concepts*. 2nd ed. Cambridge University Press, 2020. DOI: 10.1017/9781108123815.

[31] E. Abrahams et al. "Scaling Theory of Localization: Absence of Quantum Diffusion in Two Dimensions". In: *Phys. Rev. Lett.* 42 (10 Mar. 1979), pp. 673–676. DOI: 10.1103/PhysRevLett.42.673. URL: https://link.aps.org/doi/10.1103/PhysRevLett.42.673.

[32] D. S. Kim et al. "Phonon anharmonicity in silicon from 100 to 1500 K". In: *Phys. Rev. B* 91 (1 Jan. 2015), p. 014307. DOI: 10.1103/PhysRevB.91.014307. URL: https://link.aps.org/doi/10.1103/PhysRevB.91.014307.

[33] W. A. Kamitakahara et al. "Vibrational spectrum of amorphous silicon: Experiment and computer simulation". In: *Phys. Rev. B* 36 (12 Oct. 1987), pp. 6539–6542. DOI: 10.1103/PhysRevB.36.6539. URL: https://link.aps.org/doi/10.1103/PhysRevB.36.6539.

[34] Y. M. Beltukov et al. "Boson peak and Ioffe-Regel criterion in amorphous siliconlike materials: The effect of bond directionality". In: *Phys. Rev. E* 93 (2 Feb. 2016), p. 023006. DOI: 10.1103/PhysRevE.93.023006. URL: https://link.aps.org/doi/10.1103/PhysRevE.93.023006.

[35] R J Bell and D C Hibbins-Butler. "Acoustic and optical modes in vitreous silica, germania and beryllium fluoride". In: *Journal of Physics C: Solid State Physics* 8.6 (Mar. 1975), p. 787. DOI: 10.1088/0022-3719/8/6/009. URL: https://dx.doi.org/10.1088/0022-3719/8/6/009.

[36] Philip B. Allen and Joseph L. Feldman. "Thermal conductivity of disordered harmonic solids". In: *Phys. Rev. B* 48 (17 Nov. 1993), pp. 12581–12588. DOI: 10.1103/PhysRevB.48.12581. URL: https://link.aps.org/doi/10.1103/PhysRevB.48.12581.

[37] Philip B. Allen et al. "Diffusons, locons and propagons: Character of atomie yibrations in amorphous Si". In: *Philosophical Magazine B* 79.11-12 (1999), pp. 1715–1731. DOI: 10.1080/13642819908223054.

[38] Buxuan Li et al. "The importance of localized modes spectral contribution to thermal conductivity in amorphous polymers". In: *Communications Physics* 5.1 (Dec. 2022), p. 323. ISSN: 2399-3650. DOI: 10.1038/s42005-022-01103-x. URL: https://doi.org/10.1038/s42005-022-01103-x.

[39] Julian D. Gale and Andrew L. Rohl. "The General Utility Lattice Program (GULP)". In: *Molecular Simulation* 29.5 (2003), pp. 291–341. DOI: 10.1080/0892702031000104887. eprint: https://doi.org/10.1080/0892702031000104887. URL: https://doi.org/10.1080/0892702031000104887.

[40] Harald Böttger. *Principles of the Theory of Lattice Dynamics*. Physik-Verlag, 1983. ISBN: 3-87664-064-4.

[41] Sabyasachi Nag, Arti Garg, and T. V. Ramakrishnan. "Nature of single-particle states in disordered graphene". In: *Phys. Rev. B* 93 (23 June 2016), p. 235426. DOI: 10.1103/PhysRevB.93.235426. URL: https://link.aps.org/doi/10.1103/PhysRevB.93.235426.

[42] Philip B. Allen and Jonathan Kelner. "Evolution of a vibrational wave packet on a disordered chain". In: *American Journal of Physics* 66.6 (June 1998), pp. 497–506. ISSN: 0002-9505. DOI: 10.1119/1.18890. eprint: https://pubs.aip.org/aapt/ajp/article-pdf/66/6/497/11510766/497_1_online.pdf. URL: https://doi.org/10.1119/1.18890.

[43] G V Lewis and C R A Catlow. "Potential models for ionic oxides". In: *Journal of Physics C: Solid State Physics* 18.6 (Feb. 1985), p. 1149. DOI: 10.1088/0022-3719/18/6/010. URL: https://dx.doi.org/10.1088/0022-3719/18/6/010.

[44] Xingfan Zhang et al. "Toward a Consistent Prediction of Defect Chemistry in CeO2". In: *Chemistry of Materials* 35.1 (2023), pp. 207–227. DOI: 10.1021/acs.chemmater.2c03019. eprint: https://doi.org/10.1021/acs.chemmater.2c03019. URL: https://doi.org/10.1021/acs.chemmater.2c03019.

[45] David Crandles. Private Communication. May 25, 2023.

[46] M. S. Islam and L. J. Winch. "Defect chemistry and oxygen diffusion in the $HgBa_2Ca_2Cu_3O_{8+\delta}$ superconductor: A computer simulation study". In: *Phys. Rev. B* 52 (14 Oct. 1995), pp. 10510–10515. DOI: 10.1103/PhysRevB.52.10510. URL: https://link.aps.org/doi/10.1103/PhysRevB.52.10510.

[47] Luis Elcoro and Jesús Etxebarria. "Common misconceptions about the dynamical theory of crystal lattices: Cauchy relations, lattice potentials and infinite crystals". In: *European Journal of Physics* 32.1 (Nov. 2010), p. 25. DOI: 10.1088/0143-0807/32/1/003. URL: https://dx.doi.org/10.1088/0143-0807/32/1/003.

[48] Hiroshi Fukui et al. "Precise determination of elastic constants by high-resolution inelastic X-ray scattering". In: *Journal of Synchrotron Radiation* 15.6 (Nov. 2008), pp. 618–623. DOI: 10.1107/S0909049508023248. URL: https://doi.org/10.1107/S0909049508023248.

[49] Naoya Uchida and Shoichi Saito. "Elastic Constants and Acoustic Absorption Coefficients in MnO, CoO, and NiO Single Crystals at Room Temperature". In: *The Journal of the Acoustical Society of America* 51.5B (1972), pp. 1602–1605. DOI: 10.1121/1.1913005. eprint: https://doi.org/10.1121/1.1913005. URL: https://doi.org/10.1121/1.1913005.

[50] Wang Jifang, E S Fisher, and M H Manghnzmi. "Elastic Constants of Nickel Oxide". In: *Chinese Physics Letters* 8.3 (Mar. 1991), p. 153. DOI: 10.1088/0256-307X/8/3/012. URL: https://dx.doi.org/10.1088/0256-307X/8/3/012.

[51] Julian Gale and Connor Wilson. *Phonon frequencies as observables*. Materials Science Community Discourse. 2022. URL: https://matsci.org/t/phonon-frequencies-as-observables/44751.

[52] V N Popov. "Shell model parameters for layered copper oxides". In: *Journal of Physics: Condensed Matter* 7.8 (Feb. 1995), p. 1625. DOI: 10.1088/0953-8984/7/8/011. URL: https://dx.doi.org/10.1088/0953-8984/7/8/011.

[53] Mohammed Reda Chellali et al. "On the homogeneity of high entropy oxides: An investigation at the atomic scale". In: *Scripta Materialia* 166 (2019), pp. 58–63. ISSN: 1359-6462. DOI: https://doi.org/10.1016/j.scriptamat.2019.02.039. URL: https://www.sciencedirect.com/science/article/pii/S1359646219301253.

[54] Ling Lin et al. "Mechanochemical synthesis: route to novel rock-salt-structured high-entropy oxides and oxyfluorides". In: *Journal of Materials Science* 55.36 (Dec. 2020), pp. 16879–16889. ISSN: 1573-4803. DOI: 10.1007/s10853-020-05183-4. URL: https://doi.org/10.1007/s10853-020-05183-4.

[55] G. T. Barkema and Normand Mousseau. "Event-Based Relaxation of Continuous Disordered Systems". In: *Phys. Rev. Lett.* 77 (21 Nov. 1996), pp. 4358–4361. DOI: 10.1103/PhysRevLett.77.4358. URL: https://link.aps.org/doi/10.1103/PhysRevLett.77.4358.

[56] Joseph Sushil et al. "High entropy phase evolution and fine structure of five component oxide (Mg, Co, Ni, Cu, Zn)O by citrate gel method". In: *Materials Chemistry and Physics* 259 (2021), p. 124014. ISSN: 0254-0584. DOI: https://doi.org/10.1016/j.matchemphys.2020.124014. URL: https://www.sciencedirect.com/science/article/pii/S0254058420313742.

[57] Christina M. Rost et al. "Local structure of the MgxNixCoxCuxZnxO(x=0.2) entropy-stabilized oxide: An EXAFS study". In: *Journal of the American Ceramic Society* 100.6 (2017), pp. 2732–2738. DOI: https://doi.org/10.1111/jace.14756. eprint: https://ceramics.onlinelibrary.wiley.com/doi/pdf/10.1111/jace.14756. URL: https://ceramics.onlinelibrary.wiley.com/doi/abs/10.1111/jace.14756.

[58] Krishna Chaitanya Pitike et al. "On the elastic anisotropy of the entropy-stabilized oxide (Mg, Co, Ni, Cu, Zn)O compound". In: *Journal of Applied Physics* 128.1 (2020), p. 015101. DOI: 10.1063/5.0011352. eprint: https://doi.org/10.1063/5.0011352. URL: https://doi.org/10.1063/5.0011352.

[59] A. Carvalho et al. "First-principles investigation of a bistable boron-oxygen interstitial pair in Si". In: *Phys. Rev. B* 73 (24 June 2006), p. 245210. DOI: 10.1103/PhysRevB.73.245210. URL: https://link.aps.org/doi/10.1103/PhysRevB.73.245210.

[60] J. T-Thienprasert et al. "First principles study of O defects in CdSe". In: *Physica B: Condensed Matter* 407.15 (2012). 26th International Conference on Defects in Semiconductors, pp. 2841–2845. ISSN: 0921-4526. DOI: https://doi.org/10.1016/j.physb.2011.08.042. URL: https://www.sciencedirect.com/science/article/pii/S0921452611007952.

[61] Yao Yao et al. "Thermal conduction mechanism of ferroelastic Zr-Y-Yb-Ta-Nb-O high-entropy oxides with glass-like thermal conductivity". In: *Journal of the American Ceramic Society* 105.6 (2022), pp. 4360–4374. DOI: https://doi.org/10.1111/jace.18374. eprint: https://ceramics.onlinelibrary.wiley.com/doi/pdf/10.1111/jace.18374. URL: https://ceramics.onlinelibrary.wiley.com/doi/abs/10.1111/jace.18374.

[62] Hamid Reza Seyf and Asegun Henry. "A method for distinguishing between propagons, diffusions, and locons". In: *Journal of Applied Physics* 120.2 (2016), p. 025101. DOI: 10.1063/1.4955420. eprint: https://doi.org/10.1063/1.4955420. URL: https://doi.org/10.1063/1.4955420.

[63] Edward Sternin. Private Communication. Aug. 16, 2023.

[64] Giacomo Livan, Marcel Novaes, and Pierpaolo Vivo. *Introduction to Random Matrices*. Springer International Publishing, 2018. DOI: 10.1007/978-3-319-70885-0. URL: https://doi.org/10.1007%5C%2F978-3-319-70885-0.

[65] Jaroslav Fabian. "Vibrations in C_{60} and Amorphous Silicon". PhD thesis. State University at New York, 1997.

[66] Jose M. Escalante and Sergey E. Skipetrov. "Level spacing statistics for light in two-dimensional disordered photonic crystals". In: *Scientific Reports* 8.1 (Aug. 2018), p. 11569. ISSN: 2045-2322. DOI: 10.1038/s41598-018-29996-1. URL: https://doi.org/10.1038/s41598-018-29996-1.

[67] Y. Y. Atas et al. "Distribution of the Ratio of Consecutive Level Spacings in Random Matrix Ensembles". In: *Phys. Rev. Lett.* 110 (8 Feb. 2013), p. 084101. DOI: 10.1103/PhysRevLett.110.084101. URL: https://link.aps.org/doi/10.1103/PhysRevLett.110.084101.

[68] Alexander Weiße et al. "The kernel polynomial method". In: *Rev. Mod. Phys.* 78 (1 Mar. 2006), pp. 275–306. DOI: 10.1103/RevModPhys.78.275. URL: https://link.aps.org/doi/10.1103/RevModPhys.78.275.

[69] M. I. Aroyo et al. "Crystallography Online: Bilbao Crystallographic Server". In: *Bulgarian Chemical Communications* 43 (Jan. 2011), pp. 183–197.

[70] Mois Ilia Aroyo et al. "Bilbao Crystallographic Server: I. Databases and crystallographic computing programs". In: *Zeitschrift für Kristallographie - Crystalline Materials* 221.1 (2006), pp. 15–27. DOI: doi:10.1524/zkri.2006.221.1.15. URL: https://doi.org/10.1524/zkri.2006.221.1.15.

[71] Mois I. Aroyo et al. "Bilbao Crystallographic Server. II. Representations of crystallographic point groups and space groups". In: *Acta Crystallographica Section A* 62.2 (Mar. 2006), pp. 115–128. DOI: 10.1107/S0108767305040286. URL: https://doi.org/10.1107/S0108767305040286.

[72] Mois I. Aroyo et al. "Brillouin-zone database on the *Bilbao Crystallographic Server*". In: *Acta Crystallographica Section A* 70.2 (Mar. 2014), pp. 126–137. DOI: 10.1107/S205327331303091X. URL: https://doi.org/10.1107/S205327331303091X.

[73] J. Zhang. "Effect of pressure on the thermal expansion of MgO up to 8.2 GPa". In: *Physics and Chemistry of Minerals* 27.3 (Feb. 2000), pp. 145–148. ISSN: 1432-2021. DOI: 10.1007/s002690050001. URL: https://doi.org/10.1007/s002690050001.

[74] W. Jauch et al. "Crystallographic symmetry and magnetic structure of CoO". In: *Phys. Rev. B* 64 (5 July 2001), p. 052102. DOI: 10.1103/PhysRevB.64.052102. URL: https://link.aps.org/doi/10.1103/PhysRevB.64.052102.

[75] Andrew C. Malingowski et al. "Substitutional Mechanism of Ni into the Wide-Band-Gap Semiconductor InTaO4 and Its Implications for Water Splitting Activity in the Wolframite Structure Type". In: *Inorganic Chemistry* 51.11 (2012), pp. 6096–6103. DOI: 10.1021/ic202715c. eprint: https://doi.org/10.1021/ic202715c. URL: https://doi.org/10.1021/ic202715c.

[76] Diogo P. Volanti et al. "Efficient microwave-assisted hydrothermal synthesis of CuO sea urchin-like architectures via a mesoscale self-assembly". In: *CrystEngComm* 12 (6 2010), pp. 1696–1699. DOI: 10.1039/B922978G. URL: http://dx.doi.org/10.1039/B922978G.

[77] Heidrun Sowa and Hans Ahsbahs. "High-pressure X-ray investigation of zincite ZnO single crystals using diamond anvils with an improved shape". In: *Journal of Applied Crystallography* 39.2 (Apr. 2006), pp. 169–175. DOI: 10.1107/S0021889805042457. URL: https://doi.org/10.1107/S0021889805042457.

[78] D.J. Lockwood, Guolin Yu, and N.L. Rowell. "Oblique incidence infrared reflectance spectroscopy of phonons in cubic MgO, MnO, and NiO". In: *Infrared Physics & Technology* 109 (2020), p. 103405. ISSN: 1350-4495. DOI: https://doi.org/10.1016/j.infrared.2020.103405. URL: https://www.sciencedirect.com/science/article/pii/S1350449520304539.

[79] R. A. Bartels and P. A. Smith. "Pressure and Temperature Dependence of the Static Dielectric Constants of KCl, NaCl, LiF, and MgO". In: *Phys. Rev. B* 7 (8 Apr. 1973), pp. 3885–3892. DOI: 10.1103/PhysRevB.7.3885. URL: https://link.aps.org/doi/10.1103/PhysRevB.7.3885.

[80] P. J. Gielisse et al. "Infrared Properties of NiO and CoO and Their Mixed Crystals". In: *Journal of Applied Physics* 36.8 (July 1965), pp. 2446–2450. ISSN: 0021-8979. DOI: 10.1063/1.1714508. URL: https://doi.org/10.1063/1.1714508.

[81] K. V. Rao and A. Smakula. "Dielectric Properties of Cobalt Oxide, Nickel Oxide, and Their Mixed Crystals". In: *Journal of Applied Physics* 36.6 (July 2004), pp. 2031–2038. ISSN: 0021-8979. DOI: 10.1063/1.1714397. URL: https://doi.org/10.1063/1.1714397.

[82] Travis I. Willett-Gies et al. "Two-phonon absorption in LiF and NiO from infrared ellipsometry". In: *Journal of Vacuum Science & Technology A* 33.6 (July 2015). 061202. ISSN: 0734-2101. DOI: 10.1116/1.4927159. eprint: https://pubs.aip.org/avs/jva/article-pdf/doi/10.1116/1.4927159/16142038/061202_1_online.pdf. URL: https://doi.org/10.1116/1.4927159.

[83] A. B. Kuz'menko et al. "Infrared spectroscopic study of CuO: Signatures of strong spin-phonon interaction and structural distortion". In: *Phys. Rev. B* 63 (9 Feb. 2001), p. 094303. DOI: 10.1103/PhysRevB.63.094303. URL: https://link.aps.org/doi/10.1103/PhysRevB.63.094303.

[84] N. Ashkenov et al. "Infrared dielectric functions and phonon modes of high-quality ZnO films". In: *Journal of Applied Physics* 93.1 (2003), pp. 126–133. DOI: 10.1063/1.1526935. eprint: https://doi.org/10.1063/1.1526935. URL: https://doi.org/10.1063/1.1526935.

[85] O. Schütt et al. "Ab initio lattice dynamics and charge fluctuations in alkaline-earth oxides". In: *Phys. Rev. B* 50 (6 Aug. 1994), pp. 3746–3753. DOI: 10.1103/PhysRevB.50.3746. URL: https://link.aps.org/doi/10.1103/PhysRevB.50.3746.

[86] J. Sakurai et al. "Crystal Dynamics and Magnetic Excitations in Cobaltous Oxide". In: *Phys. Rev.* 167 (2 Mar. 1968), pp. 510–518. DOI: 10.1103/PhysRev.167.510. URL: https://link.aps.org/doi/10.1103/PhysRev.167.510.

[87] Ch. Kant et al. "Optical spectroscopy in CoO: Phononic, electric, and magnetic excitation spectrum within the charge-transfer gap". In: *Phys. Rev. B* 78 (24 Dec. 2008), p. 245103. DOI: 10.1103/PhysRevB.78.245103. URL: https://link.aps.org/doi/10.1103/PhysRevB.78.245103.

[88] W Reichardt, V Wagner, and W Kress. "Lattice dynamics of NiO". In: *Journal of Physics C: Solid State Physics* 8.23 (Dec. 1975), p. 3955. DOI: 10.1088/0022-3719/8/23/009. URL: https://dx.doi.org/10.1088/0022-3719/8/23/009.

[89] W. Reichardt et al. "Lattice dynamics of cupric oxide". In: *Zeitschrift für Physik B Condensed Matter* 81.1 (Feb. 1990), pp. 19–24. ISSN: 1431-584X. DOI: 10.1007/BF01454208. URL: https://doi.org/10.1007/BF01454208.

[90] S. P. P. Jones et al. "Influence of nonmagnetic Zn substitution on the lattice and magnetoelectric dynamical properties of the multiferroic material CuO". In: *Phys. Rev. B* 90 (6 Aug. 2014), p. 064405. DOI: 10.1103/PhysRevB.90.064405. URL: https://link.aps.org/doi/10.1103/PhysRevB.90.064405.

[91] J. Serrano et al. "Phonon dispersion relations of zinc oxide: Inelastic neutron scattering and ab initio calculations". In: *Phys. Rev. B* 81 (17 May 2010), p. 174304. DOI: 10.1103/PhysRevB.81.174304. URL: https://link.aps.org/doi/10.1103/PhysRevB.81.174304.